Computational modeling of trabecular bone indentation and development of a new test method to perform unconstrained load-induced subsidence of an intervertebral body fusion device

by

Rémy Benais

A thesis

presented to the University of Waterloo

in fulfillment of the

thesis requirement for the degree of

Master of Applied Science

in

Mechanical and Mechatronics Engineering

Waterloo, Ontario, Canada, 2024

Author’s Declaration

I hereby declare that I am the sole author of this thesis. This is a true copy of the thesis, including any required final revisions, as accepted by my examiners.

I understand that my thesis may be made electronically available to the public.

Abstract

Intervertebral body fusion devices ("interbody cages") used in spinal surgeries are susceptible to axial and/or rotational subsidence into the underlying trabecular bone of the spinal vertebrae. Despite the variety of pre-clinical testing methods and previously developed detailed computational models, the ability to pre-operatively predict implant subsidence remains limited. Current state-of-the-art computational models have issues due to the size and complexity of existing subject-specific, image-based models. In contrast, experimental testing standards, such as ASTM F2267, overly simplify the loading and bone materials. The goals of this thesis were: 1) to develop a simplified finite element (FE) model for trabecular bone indentation towards pre-clinical implant subsidence prediction, and 2) to develop and evaluate a novel test method to perform unconstrained load-induced implant subsidence.

The first study involved explicit FE simulations created in LS-Dyna (Version 12.1, LST, Livermore, California, USA) using smoothed particle hydrodynamics (SPH) elements to model confined indentation of human trabecular bone, using different indenter-tip geometries. A generalized continuum-level approach with an isotropic crushable foam (CF) material model was developed to represent trabecular bone. Five such FE models were generated calibrated to cadaveric specimens spanning a range of bone mineral densities (BMD). Additionally, an alternative model configuration was developed that included consideration of bone marrow, with bone and marrow material parameters assigned to SPH elements randomly, owing to the quasi-stochastic nature of trabecular bone tissue microstructure. Analysis of the FE models using correlation and analysis software found a good match to the behaviour previously

observed experimentally, accurately capturing the shape of the force-displacement curves as well as bone densification patterns seen in clinical imaging. Inclusion of marrow elements offered improved response prediction of the flat-tip indenter tests.

In a second study, a new force-control (FC) experimental testing method was developed for conducting unconstrained load-induced implant subsidence. This new method was compared to the ASTM F2267 method, which uses a lubricated ball-and-socket joint (BSJ), using the VIVO joint motion simulator (AMTI, Massachusetts, USA) to apply unconstrained loading up to 4kN. Subsidence testing was performed on two different polyurethane (PU) foams densities (rigid 20 and 30 PCF) sandwiched together providing a boundary interface to induce implant rotation into the less dense foam. Unconstrained axial compression up to 4kN yielded, on average, 2.51 mm (SD = 0.38) versus 4.68 mm (SD = 0.57) of axial subsidence for BSJ setup compared to the FC setup, respectively. The BSJ setup had an average implant rotation of 2.77° (SD = 0.50), in contrast to the FC setup, with an average of 17.97° (SD = 0.89). The results were further compared to computational results using a SPH FE model mimicking the experiment.

Ultimately, the presented work demonstrates the ability of a generalizable continuum-level SPH approach to capture bone variability using clinical bone imaging metrics without needing detailed image-based geometries, a significant step towards simplified pre-clinical modeling of implant subsidence prediction. Further, the development of new experimental testing methods for unconstrained load-induced subsidence demonstrates the potential improvement for implant subsidence testing relative to devices conforming to ASTM F2267.

Acknowledgements

The work in this thesis was made possible through the help of many individuals. First, I would like to thank my supervisor Dr. Stewart McLachlin for his guidance, expertise, patience, and kindness. He introduced me to the lab and to research as an undergrad and has supported me ever since. I had two wonderful mentors in Dr. Aleksander Rycman and Martine McGregor. Alex survived the endless waves of modeling- and continuum-mechanics-related questions, and Martine lifted me up during many challenges I faced during my research. Thank you to all my fellow students in the Orthopaedic Mechatronics Lab with special thanks to Richard Barina, Matheus Correia, and Gwennyth Carroll. The entire experimental side to this research would have taken an eternity if not for the tireless nights Richard spent in the machine shop and for the fun testing days he spent with me in the concrete dungeon. Matheus for answering the plethora of modeling-related questions I had, and Gwennyth for her help with getting CT images for my test samples that really enhanced my research! I would like to thank Dr. Duane Cronin for his modeling expertise, and Dr. Renan Fernandes for his surgical knowledge and for inviting me to observe an interbody fusion surgery with my own eyes! I would like to acknowledge the Natural Sciences and Engineering Research Council and Ontario Graduate Scholarship Program for the funding that gave me the opportunity to do this research. Finally, I would like to thank my family and friends for their unwavering encouragement, and to Jess for her constant support and for all that she does for me everyday.

Table of Contents

List of Figures

List of Tables

List of Abbreviations

FE	Finite element
CT	Computerized Tomography
VM	von Mises
DP	Drucker-Prager
MC	Mohr-Coulomb
CF	Crushable Foam
p-q	Pressure – von Mises stress
E	Elastic Modulus
K	Yield Stress Ratio
PU	Polyurethane
PCF	Pounds per cubic foot
BMD	Bone Mineral Density
X-FEM	Extended Finite Element Method
SPH	Smoothed Particle Hydrodynamics
SB	Solid Bone Models
BM	Bone-Marrow Models
MPK	MAT_PLASTIC_KINEMATIC material model
BSJ	Ball-Socket Joint
FC	Force-Control
ASTM	American Society for Testing and Materials
RMSE	Root Mean Square Error
R^2	Coefficient of Determination, R-squared value
SD	Standard Deviation

Chapter 1

Introduction

1.1 Thesis Motivation: Implant subsidence following spinal fusion surgeries

There has a been a significant upwards trend of lumbar spinal fusion surgeries, with a 229% increase in the number of procedures performed between 1993 and 2012 in Canada [1]. These surgical procedures are intended to address debilitating spinal disorders arising from degeneration, trauma, and deformity. Fusion surgeries that involve anterior spinal column reconstruction commonly use intervertebral body implants ("interbody cages") (Figure 1.1). Interbody cage implants are used towards three surgical goals: (1) promoting healthy fusion of the adjacent vertebrae by containing bone graft materials, (2) restoring sagittal alignment and disc height, and (3) indirectly decompressing neural elements to relieve pain and restore function and activities of daily living for the patient [2].

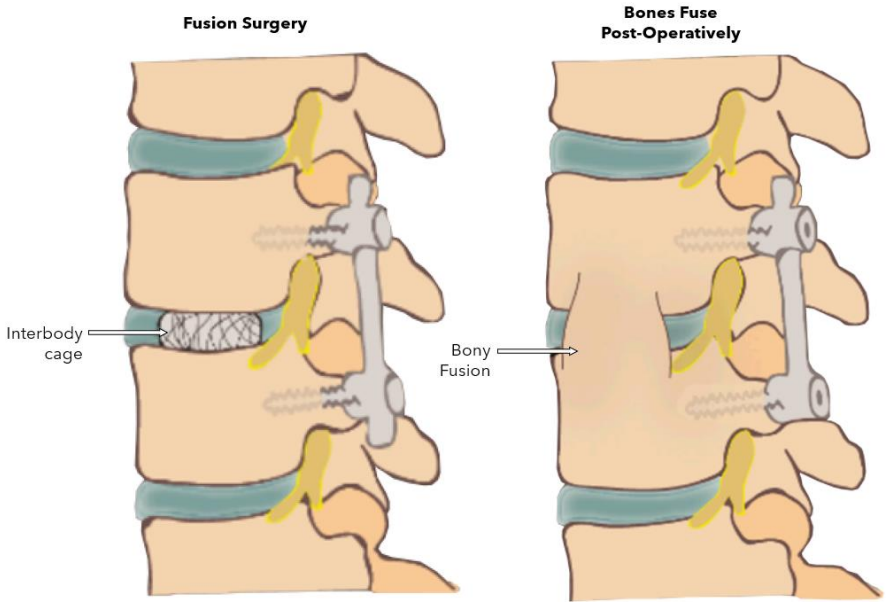

Figure 1.1 Schematic depicting bone-implant system before and after and after successful spinal bony fusion [Adapted from Schickert et al. (2020)] [3]

Interbody cage implants are commonly made of biocompatible materials, like titanium alloys, that are much stiffer than the adjacent vertebral bone and do not typically conform to the surface geometry of the vertebral endplate. Resultantly, their introduction into the intervertebral space induces significant stress concentrations in the adjacent bone. This can engender implant subsidence, the penetration of the implant into the bone (Figure 1.2). It is a major complication affecting 14-50% of patients undergoing interbody fusion surgery [4]–[7] and can result in complications, including recurrence of the spinal deformity for which the implant was employed, unwanted changes in spinal alignment, and in some cases neurological compression, causing pain, numbness, and the need for revision surgery [7]–[9]. Most importantly, implant subsidence can result in the failure to achieve the desired clinical goals of interbody fusion surgery, producing a poor outcome for the patient, both financially and for their short- and long-term health [10].

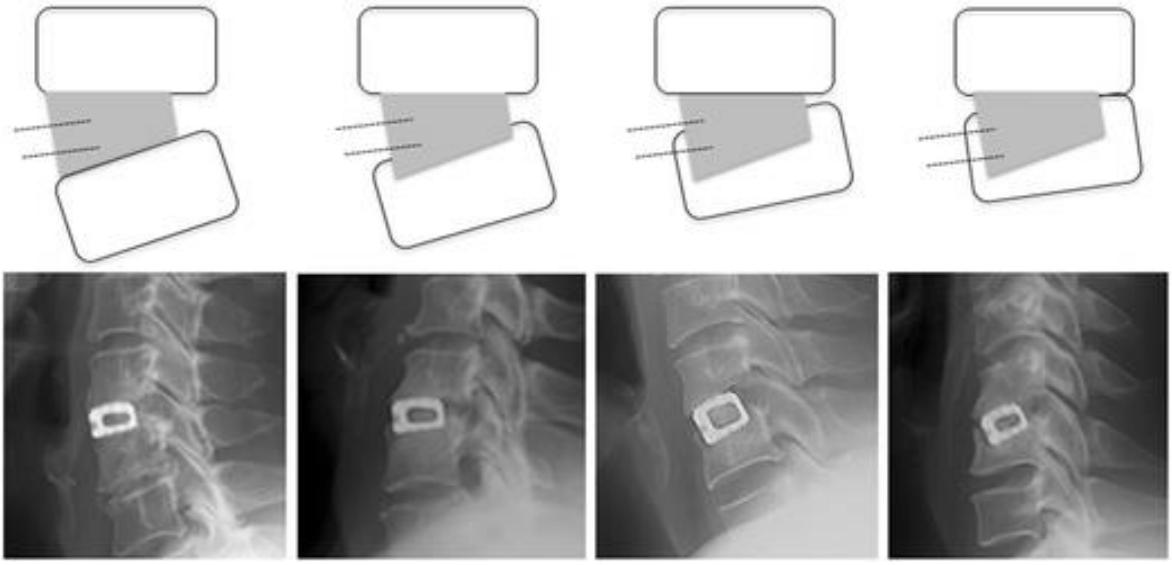

Figure 1.2 Schematic diagrams and radiographic images representing different severities of implant subsidence with progressive axial translation and rotation of the implant [Adapted from Yamagata et al. (2016)] [11]

Predictive models in orthopaedic surgery can serve as valuable tools [12], offering insights into potential outcomes and complications, thereby aiding surgeons in pre-operative planning and decision-making for spinal fusion procedures. Yet, there are currently no clinical decision-making tools for predictive risk assessment of three-dimensional (3D) implant subsidence, with only retrospective studies available to identify risk factors associated with implant subsidence [4], [13]. In general, the ability to pre-operatively predict implant subsidence is currently limited [10].

Trabecular bone indentation during implant subsidence has been extensively studied experimentally and computationally using the finite element (FE) method. Clinical observations have demonstrated that implant subsidence can involve implant rotation and progressive changes in spinal alignment [8]. This suggests that the interfaces between vertebral bone tissues and the implant, combined with the multi-axial loading modes (e.g. axial compression, bending, shear, etc.) that the spine experiences during daily activities in the early-post-operative rehabilitation period [14], influence the resulting implant subsidence. Yet, previous *in vitro* experimental investigations of implant subsidence have been limited to applying constrained uniaxial compressive loading, without consideration for such unconstrained multiaxial effects [15]–[20]. From a computational modeling perspective, previous studies have included simplified material properties, lacking consideration for continuum damage mechanics suitable for macro-level simulations, and simplified bone-implant interface conditions that have prevented modeling of trabecular bone densification which is common with implant subsidence. As a result, studies have only inferred subsidence risk based on local stress and strain concentrations, lacking any inclusion of appropriate failure

behaviour to accurately predict trabecular bone deformation and failure with implant subsidence [21]–[25].

1.2 Thesis Objectives and Approach

This thesis employed a combination of computational and experimental approaches to investigate methods for improving pre-clinical prediction of implant subsidence. The two main objectives of this thesis were as follows:

Objective 1: Develop a meshless crushable foam FE model with continuum-based geometry to represent indentation of trabecular bone.

Explicit FE simulations using meshless smoothed particle hydrodynamics (SPH) elements of confined indentation testing of human trabecular bone were performed, using flat- and sharp-tip indenters. The test setup and loading protocol followed Kulper et al. (2018) methods [26], using a generalized continuum-level approach with a crushable foam material model with isotropic hardening applied to the bone and by modeling the bone geometry as a continuum. The implementation of 'marrow' elements representing the constituents of the intra-trabecular spaces was also investigated. Material parameters were calibrated to bone specimens representing a range of bone mineral densities (BMD) based on work done by Soltanihafshejani et al. (2021) [27] and the model's force-displacement curves were compared to experimental data reported by Kulper et al. (2018) [26].

Objective 2: Evaluate a new experimental 'force-control' method for conducting unconstrained load-induced subsidence.

Two experimental setups were developed using the VIVO joint motion simulator (AMTI, Massachusetts, USA). The first method used texting fixtures inspired by the ASTM

F2267 method, including a lubricated ball-and-socket joint for unconstrained axial compression loading up to 4 kN. A second method was developed in this study using the six-axis force control capabilities of the VIVO, with the same magnitude of axial force applied but with the remaining force and moment axes holding no load in force control for unconstrained displacement. A novel bone setup was established that used two different polyurethane (PU) foam densities (rigid 20 and 30 PCF, Sawbones, USA) sandwiched together, providing a boundary to induce rotation with load-induced implant subsidence. Verification of the experimental results was performed with explicit FE simulations using a modified PU foam version of the FE model developed for Objective 1. The developed crushable foam model was calibrated to experimental material characterization tests of PU foams by Issa et al. (2023) [28] and Schulze et al. (2018) [29].

1.3 Thesis Organization

The thesis document is organized into five chapters. Chapter 1 outlines the objectives and motivation for the research. Chapter 2 delves into key background concepts and existing literature on trabecular bone damage mechanics and numerical modeling of trabecular bone. The primary contributions of the thesis are divided into two chapters: Chapter 3 focuses on the computational study (Objective 1), while Chapter 4 addresses the experimental work and verification using the developed computational model (Objective 2). Lastly, Chapter 5 offers overall conclusions and recommendations for future work.

Chapter 2

Background

2.1 Trabecular Bone

2.1.1 Anatomy and Physiology

Bone is a hard tissue that provides the mechanical structure of the human body. Bone consists of two different tissue types (cortical and trabecular) that provide it unique structural abilities. Cortical bone is a high strength, dense and solid type of osseous tissue that forms the thin outer shell (0.25-0.40 mm [30]–[32]) of the vertebral body and represents approximately 21-39% of the bone mass in the body [33]. It provides mechanical support and serves as a reservoir for minerals such as calcium and phosphates [34]. In contrast, trabecular bone, which is the focus of this thesis, is a spongy type of osseous tissue characterized by its porous honeycomb-like structure that forms the inner core of the vertebral body, confined by the cortical shell [35], contributing to 61-79% of the bone mass in the vertebral body (Figure 2.1) [33]. Under microscopic examination, trabecular bone appears as a network of interconnected thin bony struts or trabeculae that are 0.160 mm thick [36], which form a lattice-like structure, resembling a three-dimensional scaffold. The trabecular network is aligned preferentially along the lines of average loading [37] (Figure 2.1), enhancing bone strength and resilience to force by effectively transferring forces throughout the tissue, thereby minimizing localized stress concentrations, and reducing the risk of fracture.

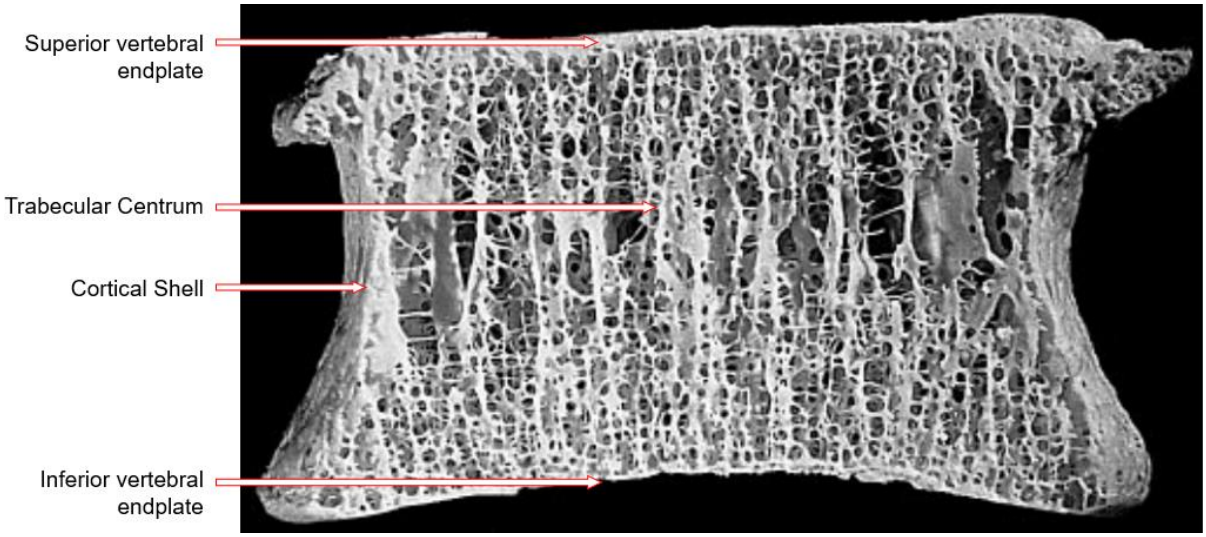

Figure 2.1 A photograph of a lumbar vertebral body cut at the mid-sagittal plane, showing the cortical shell, the vertebral endplates, and the porous trabecular core [Adapted from Mosekilde et al. (2000)] [38]

At the microstructural level, an individual trabecula is comprised of parallel lamellae groups bounded by cement lines, predominately oriented parallel to the surfaces of the trabeculae. Within these lamellae, mineralized collagen fibrils are arranged, with ellipsoidal lacunae housing osteocytes distributed throughout. The size and distribution of these lacunae are critical aspects of bone microstructure, as stress concentrations, most frequently at the longitudinal direction of the lacuna, can lead to microdamage within trabeculae [39].

The space between the trabeculae in trabecular bone consist of various constituents, including bone marrow, blood vessels, and cells that contribute to the bone's function. Bone marrow plays essential roles in lipid storage, blood cell production, providing a microenvironment for bone cells, and supporting bone remodeling [38], [40]. The marrow also provides structural support to the overall architecture of the bone tissue: the inter-trabecular fluid and intraosseous pressure has been reported to significantly influence bone strength under mechanical loading [41]. Furthermore, studies have shown that marrow fat content was

increased in osteoporotic bone, suggesting that marrow content fills the spaces vacated during bone loss [42].

2.1.2 Material Properties of Trabecular Bone

The microstructural architecture plays a dominant role in the mechanical properties of trabecular bone. Trabecular bone mineral density and the orientation of the trabecular network directly affect the tissue's biomechanical properties. The loading direction is particularly important in assessing bone's response due to the inherent anisotropic nature of the porous trabecular network [43]. Previous work has shown that loading direction has a direct influence on the location of material yielding in trabecular bone [44], and that trabeculae misaligned with respect to the load direction are significantly weaker [45].

Inter-site variation

Trabecular bone is a naturally porous cellular structure that exhibits significant variability in material properties, both between different anatomical sites (inter-site) and within the same site (intra-site). The mechanical response of trabecular bone is influenced by bone mineral density, anatomic site, geometry, and demographic factors including age, sex, and species [15], [19], [46]. Bones in different anatomical regions generally have different microstructural properties which would then lead to having differing mechanical properties depending on the anatomical site [47]–[49].

Intra-site variation

Trabecular bone also exhibits variation in mechanical properties in different parts of a same bone, for example in the superior, inferior, anterior, and posterior regions of the bone [50]. These differences stem from geometrical differences and preferential bone remodeling according to the loads exerted on the bones, leading to variation in stiffness across

a single bone [51]. As a result, there is no universal elastic modulus for bone [46] and such properties have been derived from apparent density or bone volume fraction using linear or power-law type equations [17], [52].

Anisotropy

Trabecular bone is typically considered to exhibit orthotropic behaviour, with three planes of symmetry. However, an alternative simplified description characterizes it as a transversely isotropic structure possessing rotational symmetry about its axis of symmetry [39]. The elastic mechanical properties for trabecular bone, particularly the elastic modulus, are reportedly similar between compressive and tensile loading [17], [46]. This tension-compression symmetry is not true for plastic deformation however [53]. Additionally, due to the anisotropic architecture of the trabecular network, trabecular bone is weaker in shear than it is in compression: the shear strength of trabecular bone is approximately 0.58 times its strength in compression [54].

2.1.3 Failure Mechanisms of Trabecular Bone

The microarchitecture of trabecular bone that governs its mechanical properties is significantly influenced by the BMD. At the microscopic level, lower density trabecular bone like in the vertebra is made up of more rod-like structures and fewer plate-like structures, where the reverse is true for higher density trabecular bone [55]–[57]. This difference in microstructure influences the failure mode as lower density trabecular bone is more susceptible to bending under compression loading. Generally, in compressive loading scenarios, shear bands and strain localization are observed in trabecular bone compression fracture [58]–[60]. However, shear alone does not fully represent the experimental patterns of compressive fracture in trabecular bone: tensile stresses associated with localized buckling are observed as

well in this loading mode [61]. At the continuum level, the failure of trabecular bone in compression is generally characterized by the crushing and compaction of bone where the cells collapse, contact, and further compression is done on the bulk material [15], [55], [62].

The compressive stress-strain curve of trabecular bone can usually be characterized by three stages of the deformation behaviour (Figure 2.2). Elastic bending of the trabeculae initiates a linear elastic region until material yield where the trabecular cell walls collapse. This stage is followed by a stress plateau that occurs due to progressive collapsing of the cell walls coupled with fracture and buckling of the trabeculae, absorbing energy with increased loading. Finally, the densification of the trabecular bone occurs, greatly increasing the local stiffness of the specimen [63].

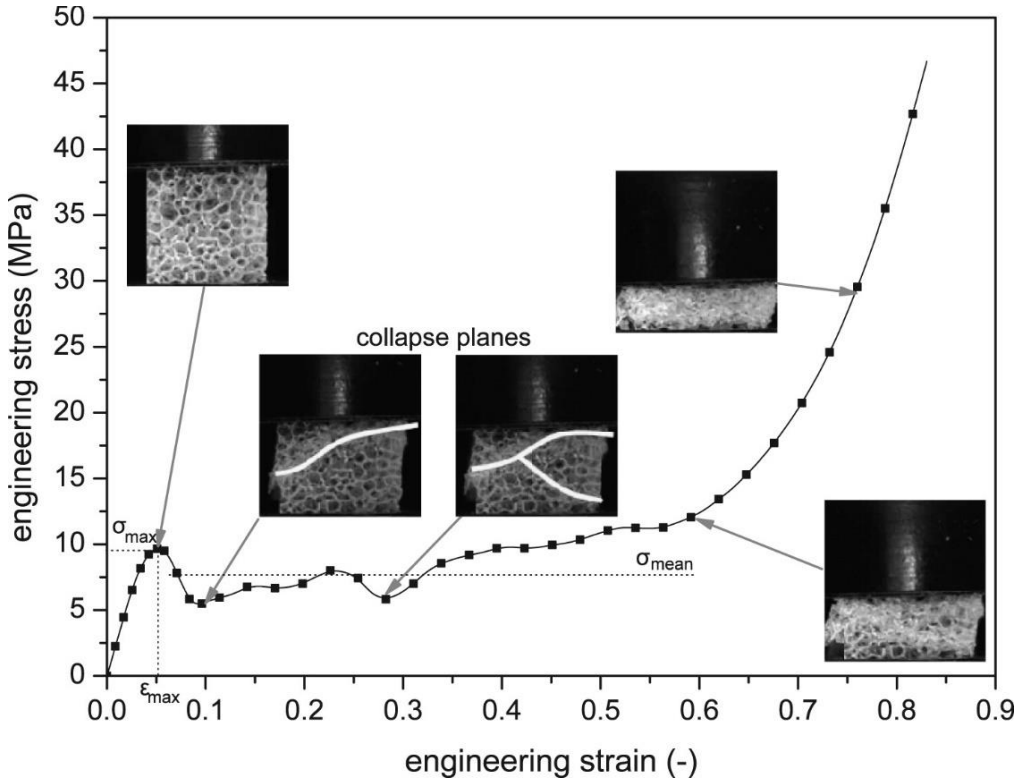

Figure 2.2 Typical compressive stress-strain curve of a trabecular sample plotted with the evolution of the deformed shape [From Halgrin et al. (2012)] [64]

This stress-strain curve is influenced by the density of the trabecular bone specimen. With increased density, the elastic modulus and yield strength in compression are increased, but the strain at which the plateau stage begins is reduced and the plateau region is followed by the stiffening from bone compaction sooner at a lower strain (Figure 2.3) [65], [66].

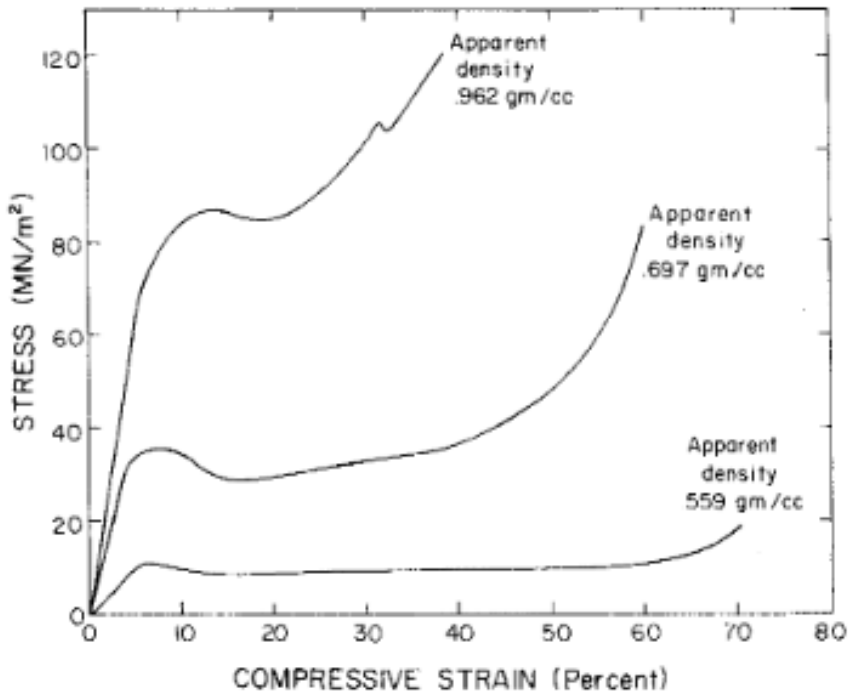

Figure 2.3 Compressive stress-strain curve of three typical specimens of bovine subchondral trabecular bone of different apparent densities [From Hayes & Carter (1976)] [65]

Bone Marrow

Bone marrow in the inter-trabecular spaces of the hard tissue has been shown to influence bone mechanical properties [41]. However, considerable intra- and inter-sample heterogeneity has been observed in the mechanical properties of bone marrow [67], with reported variations in the constitution between yellow and red marrow [68] and with site, age, and species [69], [70]. The mechanical properties of marrow are less well known and understudied due to difficulty of harvesting and because of its viscous properties [67], [71].

Only elastic properties have been previously reported to represent the behaviour of bone marrow, using rheological methods [67], [72] or with ultrasound [73], and the reported values have shown considerable heterogeneity: elastic moduli of 0.25-24.7 kPA [67] and 2 MPa [72], [73] have been reported. In shear, tensile and bending tests, it is believed that bone marrow has no significant effect on bone's mechanical properties [74], [75]. In contrast, compression tests have found that the physiological existence of marrow fat increases the stress on individual trabeculae [76], [77]. Other similar studies found that the elastic modulus, and the maximum and average compressive stresses of bone were decreased considerably when marrow was kept in their experimental bone sample. The trabeculae collapse prematurely with marrow included due to increases in transverse strain applied on the trabecular network from the marrow flow pressure in compressive loading of the bone [64], [78].

2.2 Modeling of Trabecular Bone

2.2.1 Geometry

FE modeling has emerged as a valuable tool for investigating the biomechanical behaviour of trabecular bone and other biological systems. Computational models can provide an efficient and cost-effective means to extract information from experiments [79]. In pre-clinical and clinical applications of computational biomechanics, mechanical analysis considering only generalized models is not sufficient for representing the biomechanics of each individual. Subject-specific models are needed to capture the broad spectrum of subject properties [80]. With modern three-dimensional (3D) medical imaging techniques, capturing subject-specific bone microarchitecture in FE models has become possible. In particular, computerized tomography (CT) has been leveraged to retrieve these subject-specific geometries, converting 3D images of the bone microstructure to 3D models ready for use in FE [79]. Meshing of these high-resolution geometries allows for the simulation of trabecular bone microarchitecture using simplified material constitutive laws [63]. However, for modeling macroscale experiments, they are of limited pre-clinical use [63]. While the methods by which these high-resolution geometries are generated are becoming more efficient, they are still computationally expensive, often with hundreds of thousands to millions of elements. Current microstructural bone FE models also have limitations with contact definitions, material behaviours and levels of deformation [81]. The high computational resources of these detailed models have ultimately limited the pre-clinical utility towards predicting phenomena like implant subsidence. For patient-specific prediction of implant penetrations into bone, a more time-efficient trabecular bone model is required to make these tools or resulting data more feasible and accessible in pre-clinical settings. One such alternative is the use of continuum

geometries, considering trabecular bone tissue as a solid continuum material, agnostic to the microstructural geometry. Continuum FE models can be effective in modeling macroscale simulations that include non-linear material behaviour, and complex boundary conditions and contact definitions [81]. Kelly et al. (2013) investigated a continuum geometry approach for trabecular bone coupled with a continuum-based material model and were able to produce accurate results when measuring the thickness of the bone that has been plasticly deformed beneath a punch [81].

2.2.2 Constitutive Material Modeling

The choice of constitutive model dictates the level of accuracy and range of material behaviour the computational model can represent. Typically, a linear elastic constitutive model is employed [82]–[86], but it is only relevant for experiments that assess behaviour up to 0.4% apparent strain [79]. At higher levels of bone deformation, non-linear constitutive models are needed to capture behaviour of bone tissue [18], [87], [88].

Many FE models incorporate complex constitutive models for trabecular bone and are difficult to implement to a variety of subjects due to their complexity and the difficulty to acquire material parameters from any given specimen following extensive model fitting. As a result, there is a need to develop more simplified models of trabecular bone damage, where the effects from different conditions and factors can more readily be investigated in pre-clinical studies [89].

Previous studies have proposed non-linear constitutive models that can account for trabecular bone morphology without the need of microstructural representations of bone geometry. The post-yield behaviour in these studies' models have predominantly been based on the von Mises (VM) criterion [53], [81], [89], [90], Drucker-Prager (DP) criterion [63],

[81], [91], [92], or Mohr-Coulomb (MC) criterion [63], [81], [93], [94]. Kelly et al. (2012) showed that each of these criteria could be used to produce effective stress-strain results when modeling uniaxial compression of trabecular bone modelled as a continuum. However, they showed that they were inadequate in representing the post-yield response of trabecular bone in confined compression loading scenarios [63]. Trabecular bone is a naturally confined system, being surrounded by stiffer cortical bone. Owing to this property, Kelly et al. (2012) suggested that high pressures within the marrow space would occur during plastic deformation [63]. The VM formulation's yield criterion is independent of pressure, only considering the hydrostatic stresses and thus is incapable of capturing the full stress-strain field in trabecular bone. Kelly et al. (2012) performed the first study applying DP and MC formulations for trabecular bone, where they had previously only been applied to cortical bone. They concluded that despite the consideration for pressure in these materials' yield criteria, they were incapable of accurately representing the confined compression of trabecular bone: a near elastic response was computed with these formulations at high pressures rather than plastic deformation [63]. Previous research has suggested that the modeling of the post-yield behaviour of trabecular and cortical bone necessitates the inclusion of pressure dependence in the yield criterion of the material model, particularly in continuum-based models [63], [81], [92].

Crushable Foam (CF) Material Formulation

A crushable foam (CF) model with isotropic hardening was introduced by Deshpande and Fleck for simulating the buckling of foam cell walls [95]. The CF formulation includes pressure-dependent yielding, which assumes symmetry between material behaviour in tension and compression. It defines the plastic behaviour of the material as an elliptical yield surface in the p-q (VM stress – pressure) plane (Figure 2.4) that evolves with increasing plastic strain

beyond the initial yield point, predicting material yield based on a combination of both hydrostatic pressure and deviatoric stresses.

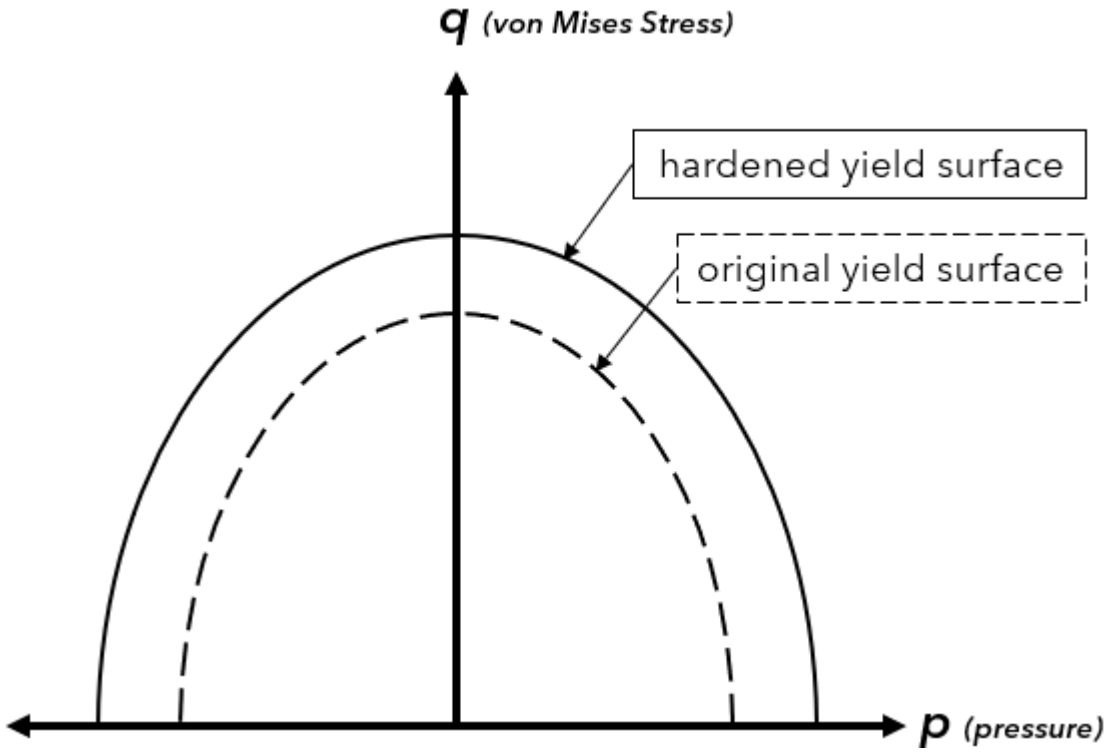

Figure 2.4 CF model yield surface evolution in p-q space (p = pressure, q = VM stress)

CF material models have previously demonstrated a similar structure and behaviour to trabecular bone, making them an effective analogue for trabecular bone for modeling purposes [55]. CF models also have a pressure-dependent yield surface, considering both hydrostatic and deviatoric stress states. A few studies have used this formulation for trabecular bone applications. In a series of papers by Kelly et al. (2012, 2013), they applied a CF model to continuum models of bovine trabecular bone, ovine trabecular bone, and a PU foam. They showed that CF models were better equipped to model the post-yield behaviour of trabecular bone in confined compression, compared to VM, DP, and MC post-yield formulations [63], [81]. They also showed that their model could qualitatively match the densification and crushing phenomena that trabecular bone experiences in bone indentation experiments [81].

Kinzl et al. (2013) developed a simple CF model that could be easily used in most commercially available FE solvers. The model produced good results until the ultimate material yield point for whole bone specimens [96]. Schulze et al. (2018) created a CF model that provided accurate results relative to experimental data for acetabular cup deformation into PU foams [29]. Soltanihafshejani et al. (2021) developed a CF model and developed empirical relationships between the material input values and the BMD in human proximal tibial specimens [27]. Their model was able to reproduce the post-yield behaviour of confined trabecular bone up to 15% strain. Their model was also applied to predict femoral bone strength where it was shown to be just as effective as when using a softened VM criterion. Additionally, it was capable of predicting various fracture locations and orientations observed in experiments [97].

2.2.3 Bone Damage Modeling

Bone damage modeling has been studied using different approaches such as the stiffness reduction approach, cohesive zone modeling, extended finite element modeling (X-FEM), the element deletion approach, by applying adaptive remeshing rules, and most recently the SPH technique.

Stiffness Reduction

Several investigations have studied non-linear trabecular behaviour by decreasing the stiffness of the trabecular material once localized principal strain surpasses a predetermined threshold, thereby simulating the damaged tissue as having lower stiffness and transmitting more of the load to the surrounding undamaged material [98]–[100]. It has successfully been implemented to determine ‘macro-level’ properties of a specimen such as the material’s yield point [99]–[101]. However, the existence of these damaged elements throughout the model can

result in numerical difficulties, particularly in compression loading [102]. As well, in cases with significant strain and deformation, the high levels of distortion that the elements withstand render the accurate prediction of fracture location, pattern, or propagation challenging [103] and thus less suitable for high deformation testing initiatives. Another similar approach to induce macro-level softening of the material used a complex constitutive law based on damage and anisotropic elasto-plastic hardening [104], but in this case too, the persistent presence of damaged elements within the solution was deemed a hindrance to the overall failure analysis.

Cohesive Zone Modeling

One method that has been used to address element separation in high deformation setups is cohesive zone modeling. Cohesive zone modeling involves inserting zero thickness 'cohesive' elements between two finite elements along the anticipated crack propagation path. Once the local fracture criterion is satisfied, the two original elements can separate from one another and the cohesive element between them expands and fills the gap. These cohesive elements have weaker mechanical properties than the original normal elements in the model. Many such models have successfully been created for crack propagation in bone [105], [106]. This method can capture the post-yield behavior of the material, which is not possible with simplified elastic fracture methods [107]. However, a limitation of cohesive zone modeling relative to other techniques is that the fracture path must either be predefined for analysis or cohesive elements must be inserted throughout the entire model, which is a laborious and inefficient process [105]–[107]. Furthermore, for macro analyses, this approach is very time-consuming and computationally expensive.

Extended Finite Element Method (X-FEM)

X-FEM offers the advantage of conveniently simulating the entire fracture process independent of the FE mesh or of the requirement to pre-define the anticipated path of the crack [108]. Damage initiation is predicted according to a defined failure criterion and once the crack initiates, an element splits in two with contact interactions being applied to the newly exposed surfaces. However, it incurs a significant computational cost and at present, it is mostly used in 2D simulations [49], [109], [110]. X-FEM has been implemented in few limited studies [103], [108], [111], but they required FE solvers and other methods that are not currently commercially available.

Element Deletion

The element deletion approach (or element 'erosion') involves deleting elements that reach pre-defined failure strain or stress criteria and the crack path is initiated following these deleted elements. This method produces numerically stable solutions [112] and has previously produced results that agree with experimental studies [112]–[116]. However, De Wit et al. (2012) suggested that this approach may not accurately capture the post-yield response of vertebral fracture in compression, as in compression the damage progresses quickly at first but then slows as trabecular bone densifies. This type of behaviour cannot be captured with element deletion, which removes material from the model [112].

Adaptive Remeshing

To model high strain in bone, without element deletion, some studies have investigated adaptive remeshing rules, [81], [117]–[119] where the FE mesh is re-meshed throughout the simulation to account for the change in shape of the newly deformed geometry. However, this method was proven to be excessively computationally demanding, sometimes requiring user

intervention. Due to this, Kelly et al. (2013) limited their study to a two-dimensional case since a 3D geometry was too costly computationally [81].

Smoothed Particle Hydrodynamics (SPH)

First introduced by Monaghan et al. (1992) [120], the meshless SPH method differs from typical Lagrangian based approaches as it does not include interconnected elements, instead employing a series of particle-looking elements (Figure 2.5) that carry attraction forces to one another over a region of influence.

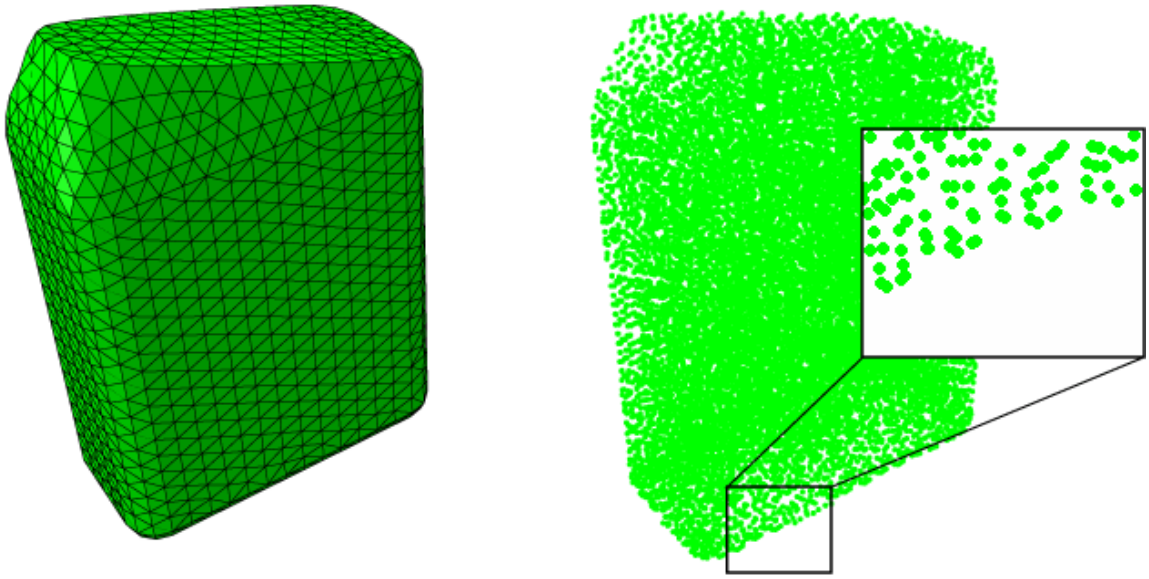

Figure 2.5 Example Lagrangian FE mesh and an equivalent SPH particle distribution [From Simulia Abaqus] [121]

The SPH approach suggests that any quantity at a point can be represented by the summation of this quantity at points whose regions of influence encompass the original point in question, multiplied by a weight function or 'kernel', where higher weight is given to points that are closer to the original point (Figure 2.6). This is a way to evaluate a quantity by sampling a neighbourhood of space and weighting points according to how close they are to the sample point of interest.

The SPH method has typically been used to model fluid flows [122]–[124] and fluid-structure interactions [125]–[127] , but has more recently seen implementation in solid mechanics, such as high velocity impacts [128]–[131] and orthopaedic applications including cement infiltration [132], medical waterjet impact [133], and bone cutting [134]. Most notably, Kulper et al. (2018) demonstrated the effectiveness of the SPH method when modeling indentation of trabecular bone by metallic implants [26] , having produced effective force-displacement results for various bone-implant setups compared to experimental data, as well as accurately representing the qualitative phenomena of bone crushing and densification. Despite the significant potential of the SPH method in orthopaedic biomechanics, there remain only a few studies that have successfully employed its use. While the use of a mesh-based FE approach for modeling large strains has inherent limitations, including the distribution of material throughout the specimen during crushing [26] , the grid-free nature of the meshless SPH method makes it very effective at modeling high strain and localized deformation especially for complex shaped structures [26], [135]. A drawback of the SPH method is its instability for analyses investigating isotropic tension of a solid and limited its use in solid mechanics problems where tensile stresses are commonly found [136]. Furthermore, the SPH method has primarily been developed and refined for fluid dynamics applications, with fewer advancements focused specifically on solid mechanics problems. For this reason, this method has not experienced widespread adoption in orthopaedic applications.

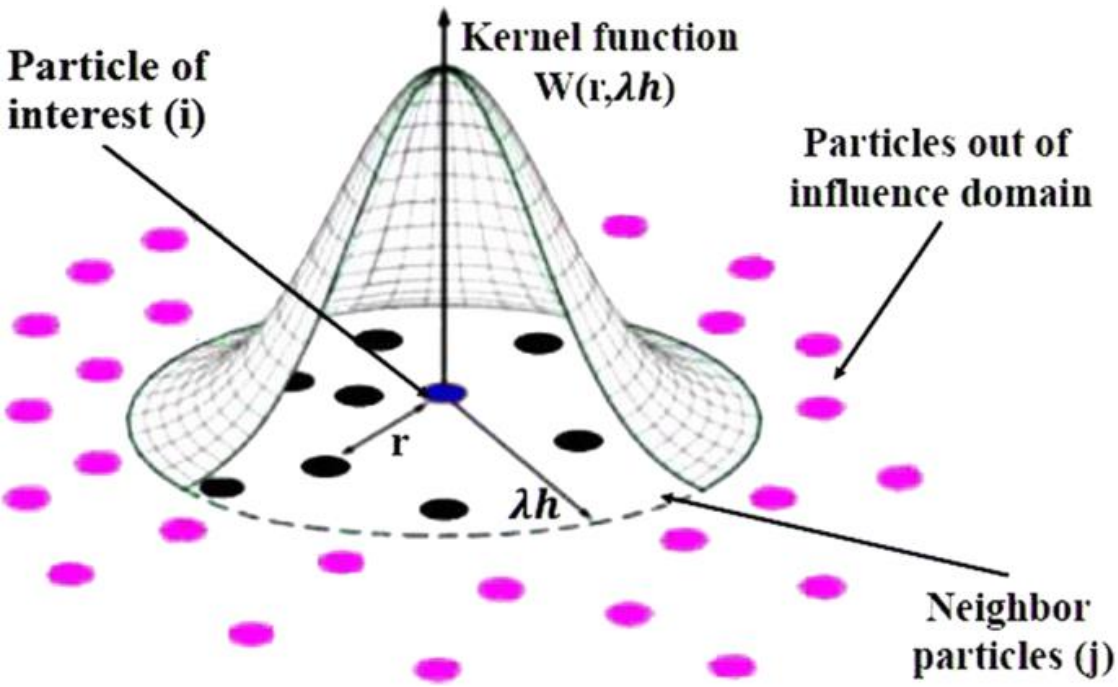

Figure 2.6 Schematic representation of an example kernel function determining the level of influence each 'particle' has on the 'particle of interest' [From Bagheri et al. (2020)] [137]

2.3 Experimental Techniques for Simulating Implant Subsidence

2.3.1 Implant Subsidence Mechanisms

Following spinal fusion surgery, anterior column support is typically required in the intervertebral space while the bone fusion process occurs. Support of the anterior spinal column is provided by interbody cage implants that are inserted between adjacent vertebrae. These implants preserve sagittal spine alignment throughout the healing process until solid osseous union is achieved. However, a prevalent failure mode is the subsidence of the implant into either of the adjacent vertebral bodies, which can lead to progressive spinal deformity and compression of neural elements, thereby reducing the chance of successful spinal fusion [138].

In regular daily activities, vertebrae are loaded with multi-axial stress states [14], [139]. In fact, FE studies analyzing vertebral failure patterns can be inaccurate due to non-uniform loading applied across the vertebral endplates [139]. Clinical observations have demonstrated implant rotation and progressive changes in spinal alignment during implant subsidence [8]. This suggests that multiaxial spinal loading associated with daily life influences implant subsidence following this operation. Lim et al. (2001) conducted an FE study comparing the amount of subsidence experienced by two different implant designs depending on the loading type applied and found that flexion loads led to significantly greater levels of subsidence relative to other loading modes including extension, lateral bending, and axial rotation [140]. This is further supported by research that has shown that multiaxial loads reduce the fatigue life of trabecular bone by a factor of five when compared to only applying uniaxial loading [141]. Further, to prevent implant subsidence, the implant and vertebral bone must have sufficient strength to resist the large *in vivo* load magnitudes, which is dependent on the underlying bone density as well as the implant shape and size [142], [143]. It is well established

that there is substantial variation in the trabecular bone density within the vertebral body [144], [145]. The vertebral endplate's density and thickness have been shown to increase toward the vertebral periphery too [138], [146]. *In vitro* studies on subsidence of implants on human vertebrae found that placing the implant along the peripheral regions of the lumbar vertebra reduces the risk of subsidence compared to placement on the weaker central portion of the body [138], [147]. In consideration of these factors, rotational implant subsidence is likely a result of the complex loads applied to the implant and the non-uniform material properties of bone beneath the implant.

2.3.2 In-Vitro Test Methods for Assessment of Implant Subsidence Risk

Current *in vitro* test methods have predominantly employed uniaxial compression testing to evaluate trabecular bone mechanical properties [15]–[20]. The widespread use of these simplified loading conditions is linked to current testing standards and regulations. The ASTM International (formerly known as the American Society for Testing and Materials) has established only two specific test methods for interbody cage implants: ASTM-F2077 Test Methods for Intervertebral Body Devices [148] and ASTM-F2267 Standard Test Method for Measuring Load Induced Subsidence of an Intervertebral Body Fusion Device Under Static Axial Compression [149]. ASTM-F2077 is designed not to directly predict the *in vivo* performance of the implants, but rather to gather data on their mechanical properties to facilitate a comparative analysis of outcomes across various devices under controlled conditions. ASTM-F2267 is specifically designed to assess interbody cage implants' resistance to subsidence. The biggest advantage of the F2267 test methods is the relative simplicity. This test method evaluates devices under an axial compressive force, which is the most dominant load mode for anterior interbody devices [150]. Further, this method prescribes the use of PU

foams as a surrogate for human vertebrae, which model the mechanical behaviour of the trabecular bone in the vertebral body well, removing the need for testing on human vertebral cadavers, which have large variances in reported mechanical properties. However, this standard only mentions static axial compression, neglecting any other loading modes. Suh et al. (2017) noted that *in vivo* loads onto vertebral bodies reflect complex shear and rotational vectors in addition to axial forces, but in their tests following ASTM-F2267, only axial loads were applied [151]. As a result, current test standards for evaluating implant subsidence neglect clinically relevant behaviours of the bone-implant interaction. Only a few *in vitro* tests have incorporated unconstrained loading of interbody devices where the implant was free to translate and rotate in and about all uncontrolled axes [152]–[155] , but their methods have only been applied to the assessment of the stabilization of the implants and have not been used to test the implant's resistance to axial and rotational subsidence.

Materials (Sawbones)

PU foams are cellular structures composed of solid polymeric struts and voids. Rigid PU foam is a closed-cell polymeric foam and is commonly used as bone surrogates in biomechanical testing of orthopaedic implants and instruments because of the foam structure's similarity to that of trabecular bone and the strong similarity between these two materials' mechanical behaviour. Like trabecular bone, PU foam's microstructure can be described by a network of struts and plates (Figure 2.7) [156] .

Studies investigating the mechanical properties of PU foam found that PU foam provided consistent elastic responses that resembled the response of trabecular bone. The overall stiffness, elastic modulus and the compressive strength of PU foam was also found to be within ranges of trabecular bone mechanical properties [62], [157]. Additionally, the

mechanical properties of the synthetic bone surrogate such as its stiffness can be varied in the experiments, as different densities of PU foam are manufactured to match mimic the range of BMD values for human and animal bone.

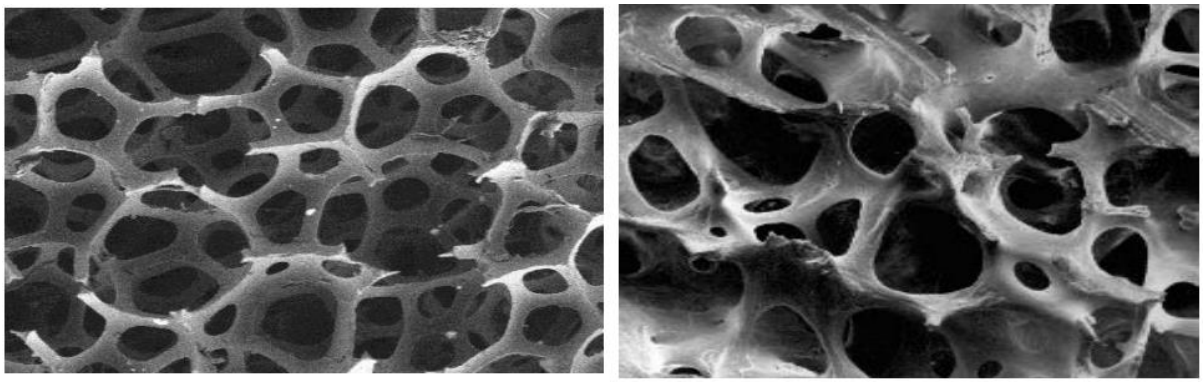

Figure 2.7 Microstructures of PU foam (left) and trabecular bone (right) [From Shim et al. (2012)] [156]

The material behaviour of PU foams in compression consists of three stages of stress-strain response (Figure 2.8), similar to that of trabecular bone (Figure 2.2): the beginning linear elastic region at low stresses and strains controlled by the cell wall bending of the foam, followed by a plateau which is associated collapse of the cells by either elastic buckling or brittle crushing, and finally a densification region with a steep increase in stress as the voids between the struts are reduced with cells collapsing and the cell wall material itself is directly loaded [156], [158].

In summary, rigid PU foam is well established as an acceptable surrogate for trabecular bone, particularly within the linear-elastic region. Its mechanical properties and material behaviour under quasi-static compression closely mirror those of trabecular bone.

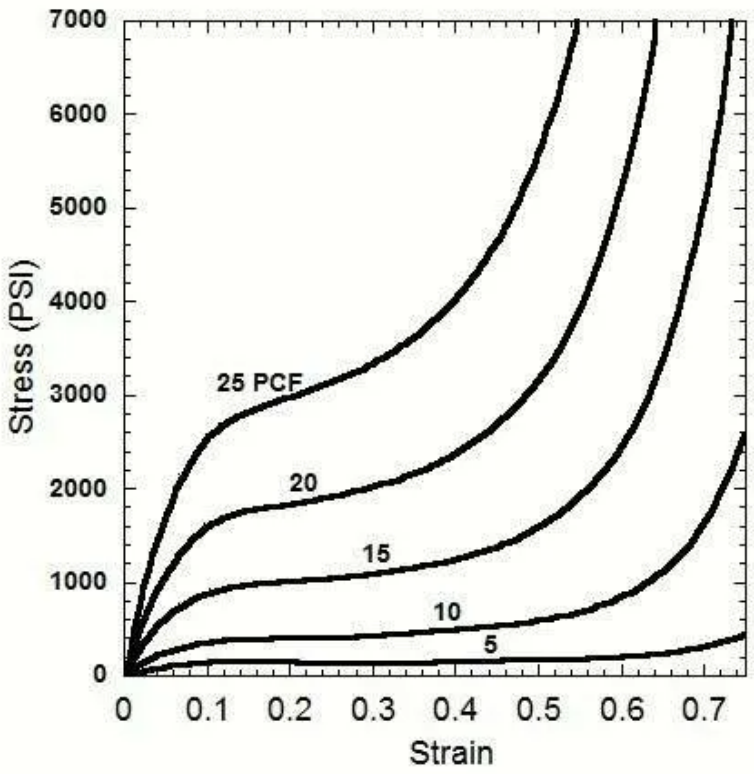

Figure 2.8 Stress-strain curves of different densities of rigid PU foam [From Haggard (2010)] [158]

2.4 Background Summary and Identified Knowledge Gaps

Due to significant inter-subject variability in trabecular bone biomechanics, accurate prediction of implant subsidence risk in the pre-clinical setting necessitates development and use of subject-specific computational models in some fashion. However, current FE modeling methods for representing trabecular bone post-yield behaviour commonly employ CT-based geometries representative of subject's bones, as well as material and damage modeling techniques that present challenges due to their size and complexity for efficient and effective translation to pre-clinical settings. As an alternative, the ability of the SPH method to effectively represent the crushing and densification phenomena of trabecular bone in bone indentation, combined with the CF material formulations' improved prediction of the post-yield behaviour of trabecular bone, may present an option to develop more simplified FE models using standard clinical metrics like BMD to identify implant subsidence risk.

Additionally, while implant rotation during subsidence has been observed clinically, unconstrained load-induced subsidence has not been previously explored in *in vitro* or computational studies. Implant performance evaluation has instead used simplified material and loading protocols using uniaxial compression experiments, as exemplified by the singular ASTM standardized test method for assessing risk of implant subsidence.

Working towards a goal of addressing the pre-clinical problem of accurately predicting trabecular bone damage and implant subsidence and assessing risk factors for different types of patients, the following knowledge gaps were identified for this thesis:

1. Continuum-based geometries and material models have shown benefits for building efficient and effective FE models. However, there remains a gap in leveraging these

methods to accurately representing bone biomechanics across a range of bone mechanical properties.

2. The SPH method has an ability to effectively model localized crushing and high strains. However, it has not yet been widely adopted in trabecular bone modeling and continued research is needed to assess its effectiveness.
3. Limited studies have investigated the effect of marrow presence on trabecular bone biomechanics and its exclusion from current state-of-the-art FE models could potentially obfuscate relevant bone behaviour in confined indention experiments.
4. Existing experimental testing standards for assessing implant subsidence may oversimplify the complex loading conditions experienced *in vivo*. Research should explore the influence of unconstrained loading on subsidence to develop more comprehensive test protocols.
5. Finally, limited research has suggested that multiaxial loading modes resulting in rotational loading onto the implant during subsidence could increase the total amount of implant subsidence. Further investigation into rotational subsidence is required to understand its impact.

Chapter 3

Development of a continuum-based meshless finite-element model to represent trabecular bone indentation[1]

3.1 Introduction

Metallic implants made of biocompatible materials are widely used in orthopaedic surgery to provide structural support in the treatment of various bone and joint disorders. For example, in anterior column reconstruction procedure in spinal surgeries, metallic interbody cage implants are used to restore disc height and sagittal alignment while promoting rigid fixation of the adjacent vertebrae. However, implant subsidence, characterized by penetration of the implant into underlying trabecular bone of the vertebral body, is a result of high stress concentrations due to the altered load path between the vertebrae [81]. It is a major complication of interbody fusion procedures, with rates reportedly as high as 14-50% [4], [6], [7]. However, predicting which patients are at-risk of implant subsidence requires effective tools, such as computational models, to better understand how the trabecular bone may fail under different conditions. Improved modeling techniques for the prediction of implant subsidence would allow for enhanced pre-operative patient-specific assessments, and ultimately for the design and development of better interbody cage implants.

The microarchitecture of trabecular bone that governs its mechanical properties is significantly influenced by the bone's density [65], [66]. At the microscopic level, trabecular bone compressive failure can be described by shear bands and strain localization [58]–[60].

[1] The research presented in this chapter will be submitted for review as a manuscript.

Also, tensile stresses with localized buckling are observed in their experimental fracture pattern [61]. At the continuum level, the failure of trabecular bone in compression is generally characterized by the crushing and compaction of bone where the cell walls collapse, the cell material contacts stiffening the entire system rapidly [15], [55], [62]. The bone marrow in the inter-trabecular spaces has also been known to influence the mechanical properties of the bone system [41].

Considerable intra- and inter-sample heterogeneity has been observed in bone marrow's mechanical properties [67], with reported variations in the constitution between yellow and red marrow [68], [159] and with site, age, and species [69], [70]. While the mechanical properties of marrow are less well known and understudied [67], [71]–[73], a significant effect on the mechanical response of trabecular bone has been observed in micro-level FE analyses where bone geometry and marrow localization was derived from CT-based images [76]. This has also been observed in *in vitro* studies where it was shown that the inclusion of marrow leads to premature collapse of trabecular due to marrow flow pressure applying transverse strain onto the trabeculae [64], [78].

In terms of modeling trabecular bone behaviour under potential damage loading scenarios, like indentation, many simplified elasto-plastic models have been developed based on the VM criterion [53], [81], [89], [90], DP criterion [63], [81], [91], [92], or MC [63], [81], [93], [94] for both continuum-level and micro-level representations of trabecular bone. However, these models have been shown to be inadequate in representing the post-yield response of trabecular bone in confined compression [63], [81]. The accurate prediction of the post-yield behaviour of trabecular bone is of particular importance due to high strain and high deformation bone is subjected to in indentation and implant subsidence studies. Additionally,

the confined configuration of compression tests is a clinically relevant loading mode for trabecular bone due to its confined nature within the cortical shell. Kelly et al. (2013) demonstrated that a pressure dependent yielding material formulation was necessary for the simulation of confined compression of trabecular bone [81]. CF material models have previously demonstrated a similar structure and behaviour to trabecular bone, making them an effective analogue for trabecular bone for modeling purposes [55]. CF models also have a pressure-dependent yield surface, considering both hydrostatic and deviatoric stress states. These CF models have also shown advantages in representing the behaviour of trabecular bone in indentation and crushing loading scenarios relative other material models that have commonly been applied to trabecular bone [63].

Bone damage modeling has been investigated using various methods such as the reduced stiffness approach, cohesive zone modeling, the extended finite-element method (X-FEM), the element deletion approach and by applying adaptive remeshing rules. However, these methods are limited in their ability to accurately model the post-yield behaviour of trabecular bone computationally efficiently in macro-scale simulations such as bone indentation tests. The SPH method has recently seen its implementation in orthopaedic applications such as cement infiltration [132], medical waterjet impact [133], and bone cutting [134]. The grid-free nature of the mesh-less SPH method makes it very effective at modeling high strain and localized deformation [26], [135]. Kulper et al. (2018) demonstrated the effectiveness of the SPH method when modeling indentation of trabecular bone by metallic implants [26]. Despite the significant potential of the SPH method in orthopaedic biomechanics, there remains are a few studies that have successfully employed its use. Since the SPH method has primarily been developed and refined for fluid dynamics applications,

with fewer advancements focused specifically on solid mechanics problems. For this reason, this method has not experienced wide-spread adoption in orthopaedic applications.

Computational models of the trabecular bone microstructure, while being highly accurate from a geometry perspective through the utilization of CT imaging, are very expensive computationally in non-linear analyses. This computational cost and effort limit the pre-clinical utility towards predicting phenomena like implant subsidence. Towards pre-clinical prediction of implant penetration into bone, a more-time efficient continuum-based trabecular bone model would be required to make this tool or resulting data more feasible and accessible in pre-clinical settings [63]. Kelly et al. (2013) investigated a continuum-based geometry approach for trabecular bone coupled with a continuum-based material model and were able to produce accurate results when measuring the thickness of the bone that has been plasticly deformed beneath a punch [81].

Despite many advances in modeling trabecular bone damage, there remains a gap in translating many of these models and their associated outcomes to pre-clinical and clinical settings. Generally, computational models that have been developed are either insufficient and incapable of capturing the phenomena relating to bone damage and crushing, or are far too complex, making them unreasonable to be applied to a range of subject-specific parameters. Most of the previously developed models representing trabecular bone crushing behaviour are mesh-based and considered the trabecular bone response only up to the ultimate stress, incapable of capturing post-yield behaviour of trabecular bone [27], [63], [96]. Further, the use of a mesh-based approach for modeling large strains has inherent negatives including the distribution of material throughout the specimen during crushing [26]. Many other models incorporate complex constitutive models for trabecular bone and are difficult to implement to

a variety of subjects due to their complexity and the difficulty to acquire material parameters from any given specimen following extensive model fitting. As a result, there is a need to develop more simplified models of trabecular bone damage, where the effects from different pre-clinical and subject-specific conditions and factors can more readily be investigated [89].

The primary objective of this study was to develop an SPH-based indentation model of trabecular bone and quantitatively and qualitatively assess its agreement with experimental findings. A second objective of this study was to create an SPH-based model of trabecular using a composite-like approach by modeling trabecular bone with both ‘bone’ and ‘marrow’ elements. It was hypothesized that an SPH-based CF model with continuum-based geometry could be used to represent the behaviour of trabecular bone indentation.

3.2 Methods

Explicit FE simulations of confined indentation testing of human trabecular bone using two indenter geometries (flat-tip and sharp-tip) were performed using LS-Dyna (Version 12.1, LST, Livermore, California, USA). SPH was used to represent trabecular bone thanks to its ability to represent high strain, crushing, and localized densification and damage behaviour experienced during bone indentation.

3.2.1 SPH Representation

Solid Bone (SB) model

A continuum-level macroscale model of trabecular bone was developed based on 10 x 10 x 20 mm rectangular prisms of trabecular bone. Following convergence results, 250,000 SPH elements were used and distributed in a grid arrangement with an even spacing of 0.2 mm in each direction between each element. Each element occupied a volume of 8×10^{-3} mm^3. The smoothing length of each element, which governs the region of influence an element possesses over neighbouring elements, was set as variable and automatically calculated by the solver at each time step. This was done to allow for the smoothing lengths to decrease as elements densify and increase as elements separate from each other, which was deemed critical to avoid artificial over-stiffening of the model as bone crushing and densification occurs. Alternative settings including the hard-coding of the smoothing lengths of the SPH elements during the simulations was investigated in pilot testing but were deemed to have skewed model results with respect to experimental data.

Bone-Marrow (BM) model

An additional FE model utilizing ‘marrow’ elements was developed. Identical qualities relating to the distribution of the SPH elements were applied to this model. A percentage of

the SPH elements corresponding to the bone volume percentages of the specimens used in the experimental tests by Kulper et al. (2018) [26] were kept as ‘bone’ elements and the remaining ones were assigned as ‘marrow’ elements. Owing to the quasi-stochastic nature of the trabeculae structure, a randomization algorithm (MATLAB R2023b, The Math-Works, Inc., Massachusetts, USA) was used to define the marrow elements’ locations where ‘marrow’ material properties were assigned. Pilot testing with multiple generated models using this randomization algorithm was done to ensure consistent results between models with equal proportions of ‘bone’ and marrow’ elements. The preferential alignment of trabeculae in trabecular bone networks was not considered in this novel test method. The experimental specimens used in the flat-tip indenter tests had bone volume percentages ranging from 17.88% to 18.85%; those used for the sharp-tip indenter tests had bone volume percentages ranging from 26.63% to 30.49%. To represent the average bone volume percentage of the experimental specimens used in the flat-tip indenter tests, one FE model was developed using 45,000 SPH elements (18% of all SPH elements) with material properties representative of trabecular bone and using 205,000 SPH elements representing the marrow. For the sharp-tip configuration, a separate model including 70,000 SPH elements (28% of all SPH elements) representing trabecular bone and 180,000 elements representing marrow was created.

3.2.2 Material Formulation

Solid Bone (SB) Model

A CF material formulation with isotropic hardening was applied to the trabecular bone specimen, using the existing model MAT_CRUSHABLE_FOAM (MAT_063) available in LS-Dyna (Version 12.1, LST, Livermore, California, USA). CF plasticity models can represent the buckling of the cell walls of trabecular bone in compressive loading modes [63]. They

incorporate pressure-dependent yielding: the von-Mises stress required to induce failure is reduced as more pressure is applied to the specimen. The CF material model used in this study is based on one developed by Deshpande & Fleck [95] which assumes symmetric behaviour in tension and compression. The yield surface is a Mises circle in the deviatoric stress plane and an ellipse in the p-q stress plane (Figure 2.4). As the material hardens, its yield surface centered at the origin of the p-q plane evolves and grows in a geometrically self-similar manner [160].

The input parameters for this material model are based off uniaxial compression tests of the experimental material. The elastic modulus, yield stress, elastic and plastic Poisson's ratios are used alongside a dimensionless yield stress ratio defining the ratio of initial yield stress in uniaxial compress to the initial yield stress in hydrostatic compression. Furthermore, the plastic region of the uniaxial compressive stress-strain response of the material provides the hardening evolution definition for the material formulation.

In the SB model, the model input parameters were first calibrated to work done by Soltanihafshejani et al. (2021) [27] where they developed empirical relationships between CF input values and BMD values in human proximal tibial specimens. Five material models were developed for this study representing a range of experimental specimen BMD values (Table 3.2) based on uniaxial compression test performed by Soltanihafshejani et al. (2021) [27].

Table 3.1 Empirical power relation of the CF material parameters based on the BMD value, developed by Soltanihafshejani et al. (2021) [27]

Mechanical Properties	Empirical Equation	BMD Value range (g/cc)
Compressive modulus (MPa)	$2131 \cdot \rho_{BMD}^{1.128}$	0.026-0.207
Yield Stress ratio (K)	$1.63 \cdot \rho_{BMD}^{-0.162}$	>0.033
Elastic Poisson's ratio	Constant	0.026-0.207
Plastic Poisson's ratio	$\frac{3 - K_{BMD}^2}{6}$	0.033-0.207

Table 3.2 CF material input parameters used for SB models (SB-CF-26, SB-CF-62, SB-CF-102, SB-CF-187, SB-CF-207), based on BMD values and empirical relationship by Soltanihafshejani et al. (2021) [27] and following the single element fitting procedure

Model ID	SB-CF-26	SB-CF-62	SB-CF-102	SB-CF-187	SB-CF-207
BMD (g/cc)	0.026	0.062	0.102	0.187	0.207
Compressive modulus (MPa)	38.226	57.322	143.493	195.283	180.473
Yield Stress ratio	0.902	1.039	1.126	1.242	1.589
Poisson's ratio - Elastic	0.16				
Poisson's ratio - Plastic	0.364	0.32	0.289	0.243	0.079

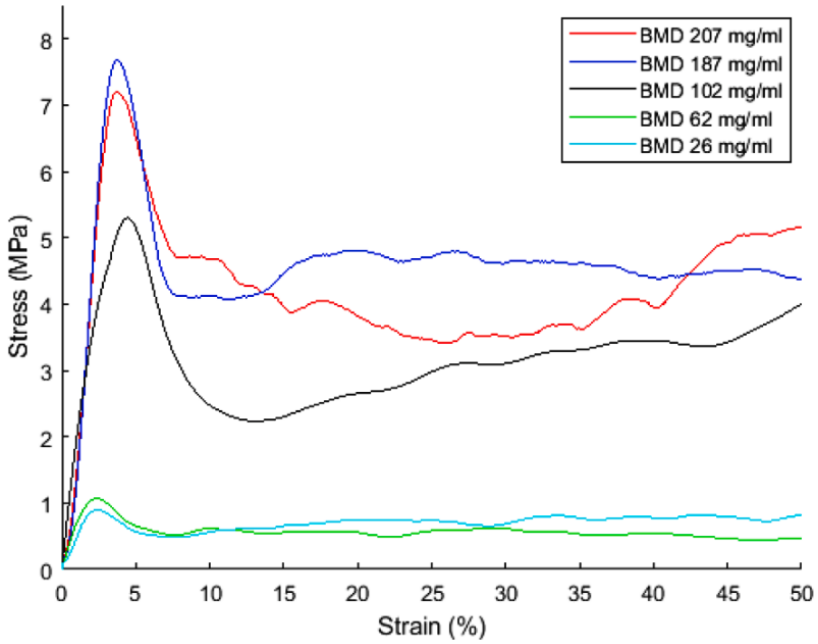

Figure 3.1 Uniaxial compression experimental tests of five trabecular bone specimens with different BMD values [From Soltanihafshejani et al. (2021)] [27]

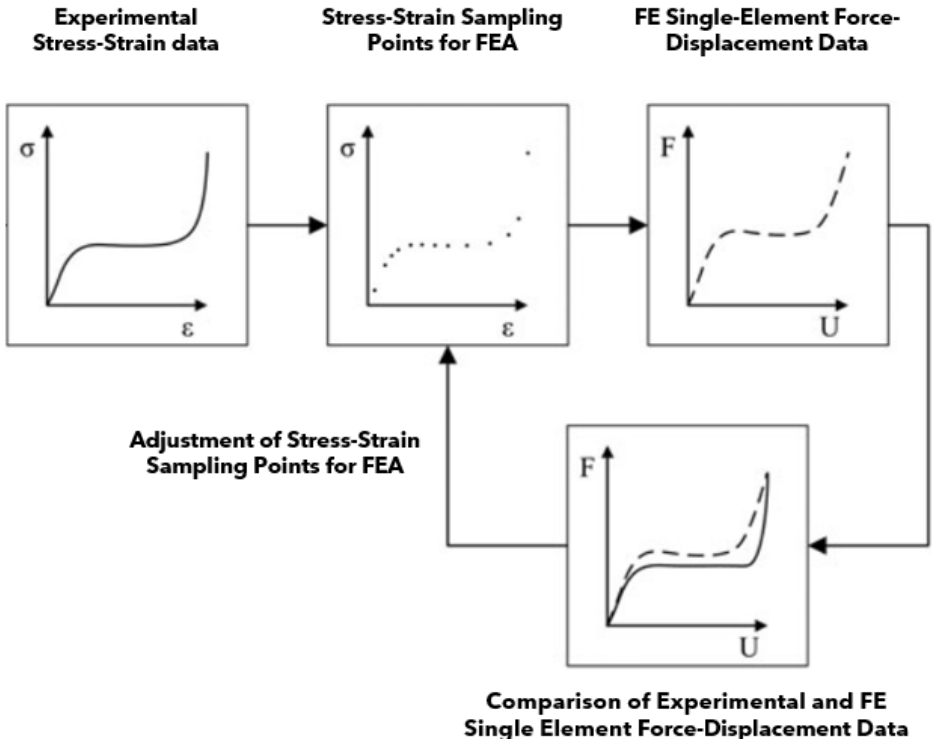

Figure 3.2 Schematic view of the single element fitting procedure for calibrating the stress-strain input data set required for the CF material definition [Adapted from Schulze et al. (2018)] [29]

A single element fitting procedure was performed for each of these material models to achieve a best fit for the reported experimental stress-strain curve. The elastic modulus and the sampled stress-strain points from the plastic region of the uniaxial compression tests of each specimen were adjusted manually to achieve a best fit uniaxial compression response, following methods by Schulze et al. (2018) [29].

For comparison purposes, an additional material model (SB-MPK) with a pressure-independent yield formulation was developed based on work by Khor et al. (2018) [116]. It utilized *MAT_PLASTIC_KINEMATIC (*MAT_003) available in LS-Dyna (Version 12.1, LST, Livermore, California, USA), which is suited for modeling isotropic and kinematic hardening plasticity. This model, originally developed for trabecular bone in cervical vertebrae, was applied to the SB model. Their input parameters are listed below (Table 3.3).

Table 3.3 MPK material parameters applied to bone in the SB model SB-MPK, based on work by Khor et al. (2018) [116]

Model ID	**SB-MPK**
Compressive modulus (MPa)	442
Tangent Modulus (MPa)	30.1
Yield Stress (MPa)	2.83
Failure Strain	0.095
Poisson's ratio	0.3

Bone-Marrow (BM) model

In the BM model, the bone elements were assigned the SB-CF-187 material model. From the estimated elastic modulus and yield stress reported on the experimental indentation specimens [26], the BMD of the specimens was estimated using the empirical relationships

developed by Soltanihafshejani et al. (2021) [27]. From this, the material model representing the sample with a BMD of 187 g/cc was selected as it provided the closest match to the mechanical properties of the experimental indentation specimens [26].

Consistent with the limited previous studies on marrow [67], [72], [76], [161], an elastic material formulation was applied to the marrow elements of the BM model and the bone marrow was simplified as pure fat content [76]. Relevant parameters were set according to work by Lacroix et al. (2002) defining the elastic properties of bone marrow (elastic modulus = 2 MPa, elastic Poisson's ratio = 0.17) [72], following the methodology of previous FE studies studying the inclusion of marrow with trabecular bone [76], [161].

3.2.3 Boundary Conditions

The test setup and loading protocol followed the methods by Kulper et al. [26]. Five rigid walls were positioned in-plane with the bottom and side faces of the bone prism to capture the confined nature of the experiment. Two indenter geometries were modeled: a flat-tip and a sharp-tip indenter. The flat-tip indenter was modeled as a 5 mm diameter cylinder, meshed with Lagrangian elements, and treated as a rigid body. The sharp-tip indenter was modeled as a 5 mm diameter cylinder with a 55˚ conical end, meshed with Lagrangian elements, and treated as a rigid body (Figure 3.3). The indenters were prescribed a stepwise loading protocol: translating axially penetrating the SPH bone model beneath it. The indenter was translated in 2 mm increments, followed by a hold to allow for material relaxation, and repeated until 10 mm of axial displacement was reached. Holds at 2 mm increments were done experimentally for ten minutes by Kulper et al. [26] to obtain photographs at different indentation depths. In this computational model, the duration of the hold was found to be insignificant since no viscoelastic effects were incorporated in the presented models. The indenter was constrained

to axial translation only; it could not translate along other axes or rotate. A static friction coefficient of 0.15 was applied for the bone-indenter contact definition and between the bone and the rigid walls, consistent with Kulper et al. (2018) [26]. Contact with the marrow elements was defined in the same way. A goal of this work was for the eventual translation of these developed models for trabecular bone to simulations representing other sorts of test methods including 3D implant subsidence. For this reason, no further simplifications of the model, including symmetry approximations, were included so that the computational cost of this method for 3D simulations could be observed.

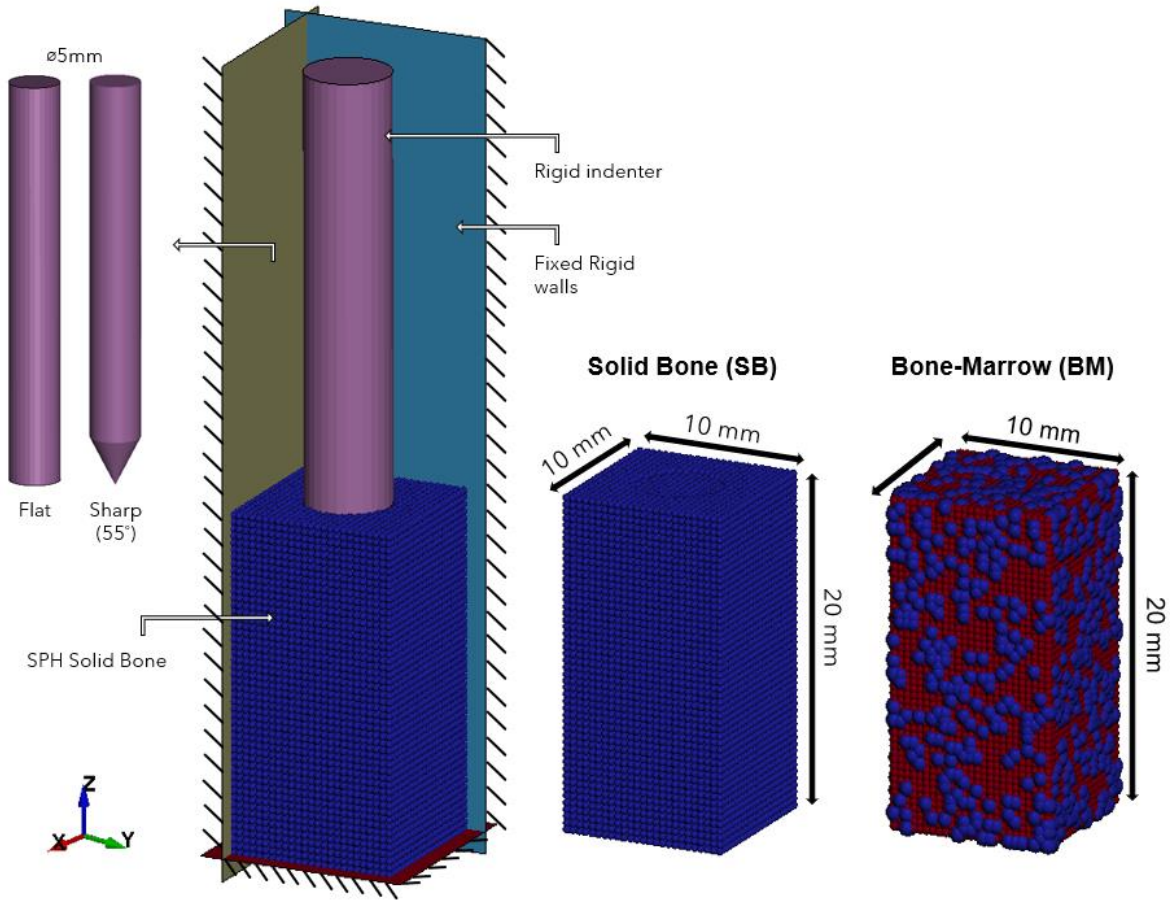

Figure 3.3 Indentation model setup, using an intermediate SPH element distribution density (65536 elements for SPH element visualization) representing both the SB and BM model meshes (blue elements = bone, red elements = marrow)

3.2.4 Analysis

Single element material fitting was assessed using a root mean square error (RMSE) algorithm (MATLAB R2023b, The Math-Works, Inc., Massachusetts, USA). Force-displacement curves were then generated and compared to the experimental data from Kulper et al. (2018) [26]. Agreement of the phase and the shape of the force-displacement response curves between the BM FE model and the experimental test data [26] was further assessed using correlation and analysis software (CORAplus v4.0.5, Partnership for Dummy Technology and Biomechanics, Ingolstadt Germany). Qualitative comparisons were made between the SB-CF and SB-MPK material models in their abilities to match the stress-strain response of trabecular bone indentation. Furthermore, qualitative assessments of bone crushing, and densification were done to determine the models' ability to accurately represent the bone densification and crushing phenomena experienced *in vivo*.

3.3 Results

3.3.1 Solid Bone (SB) Model

Single Element Material Fitting

Single element uniaxial compression tests were conducted with each SB-CF material model and graphical comparisons were made between the experimental input data and the resultant stress-strain responses from the element, to assess an accurate fitting of the material in the FE solver (Figure 3.4 & Figure 3.5).

The coefficient of determination (R^2) was calculated for each simulation-experiment pair (Table 3.4). By manually modifying the input elastic modulus and the sampling points of the plastic region of the uniaxial stress-strain curve through trial-and-error, it was possible to achieve an effective fit of the material model with respect to the experimental data, with all fits having a coefficient of determination greater than or equal to 0.9999.

Table 3.4 Coefficients of Determination for each model fitting with respect to the experimental data

Exp-Sim Pair BMD	Coefficient of Determination (R^2)
26 g/cc	0.99994
62 g/cc	0.99996
102 g/cc	0.99999
187 g/cc	0.99990
207 g/cc	0.99996

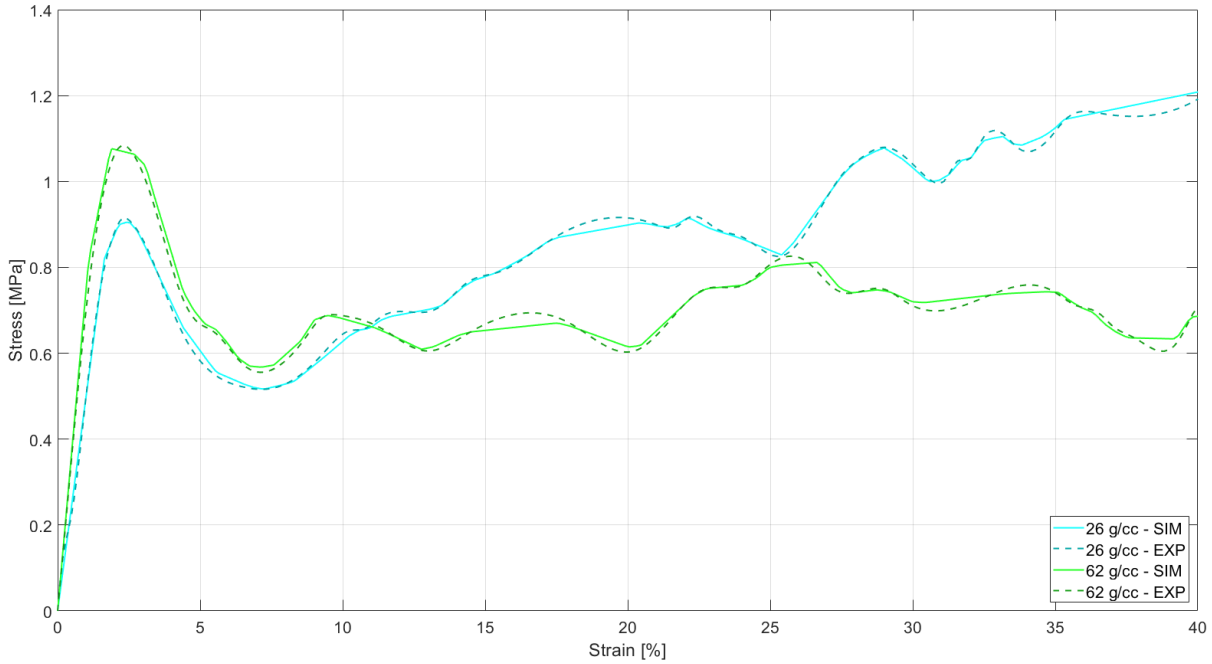

Figure 3.4 Experimental and single element fit uniaxial stress strain curves for the 26 g/cc (light blue) and 62 g/cc specimens (green)

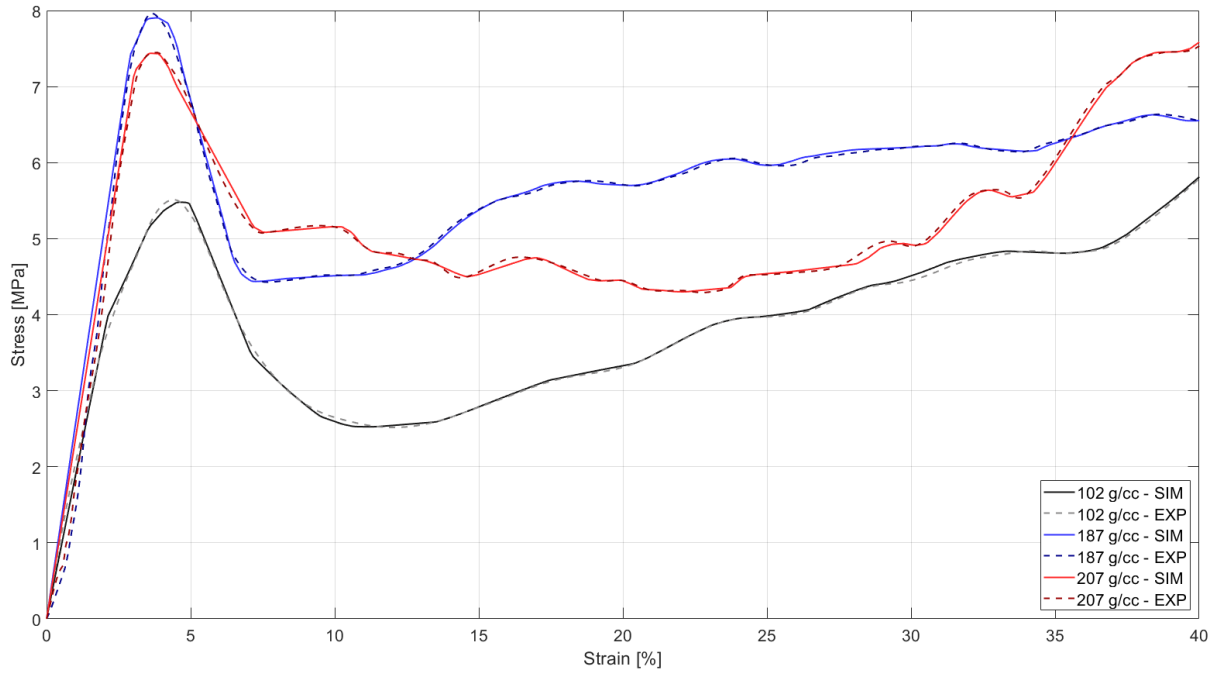

Figure 3.5 Experimental and single element fit uniaxial stress strain curves for the 102 g/cc (black), 187 g/cc (blue) and 207 g/cc specimens (red)

Convergence Analysis

A convergence analysis was performed (Figure 3.6) using the SB-CF-187 model. Due to computational cost, complete convergence was not achieved as it was expected to occur in excess of one million SPH elements based on developed power-law trendlines from the convergence datapoints. An intermediate SPH element distribution density of 250,000 elements was selected for all models in this study, balancing computational cost and numerical accuracy. The main outcomes of work in this study are force-displacement response curves and their comparison to experimental data. The test prescribed a fixed displacement rate and so the maximum force during the test was used as the measure of interest in the convergence analysis.

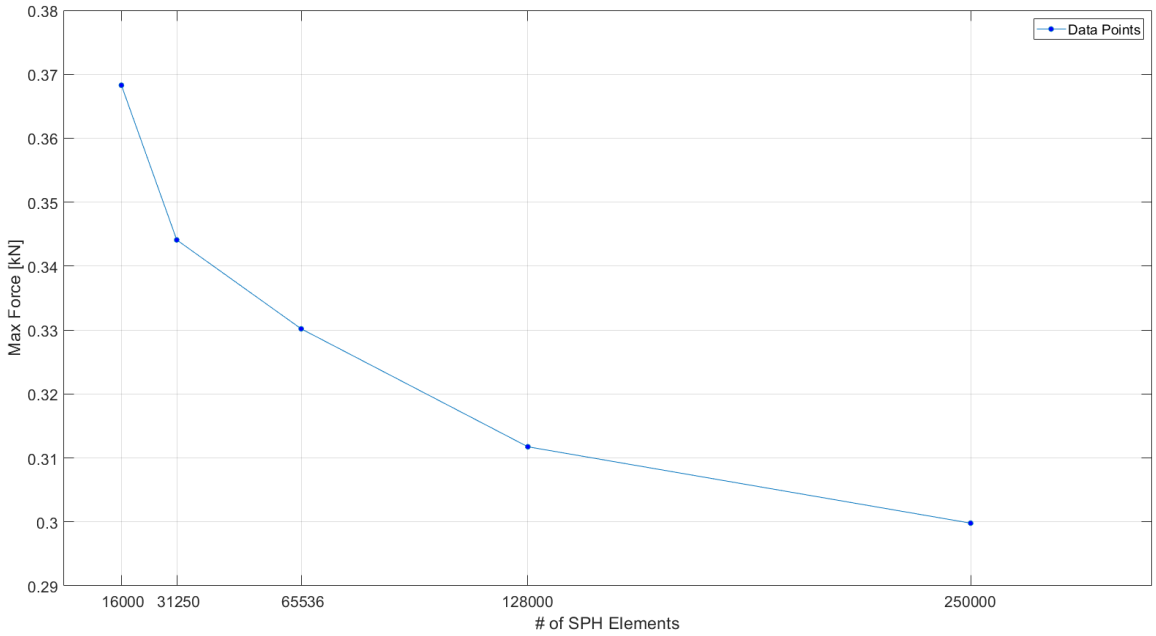

Figure 3.6 Convergence results comparing max indenter force across different SPH element distribution densities

Quantitative Results

Force-displacement plots for the flat-tip and sharp-tip indenter tests, including simulations for each BMD value tested and experimental data used for comparison were produced for model assessment (Figure 3.7 & Figure 3.8). For both test setups, the SPH CF model was capable of capturing the plastic behaviour of trabecular bone under confined indentation. In Figure 3.7, the flat-tip indenter simulations data follow the experimental behaviour with a steep slope in the force response, followed by apparent yield of the full system at approximately 0.4 mm of displacement and with a shallower slope representing a plateau with gradual densification of the trabecular bone beneath the indenter. Similarly, the sharp-tip indenter simulations follow the comparison data: a steady rise in the force response is observed with apparent yield occurring near 5.6 mm of indenter axial displacement followed by a plateau region with bone densification.

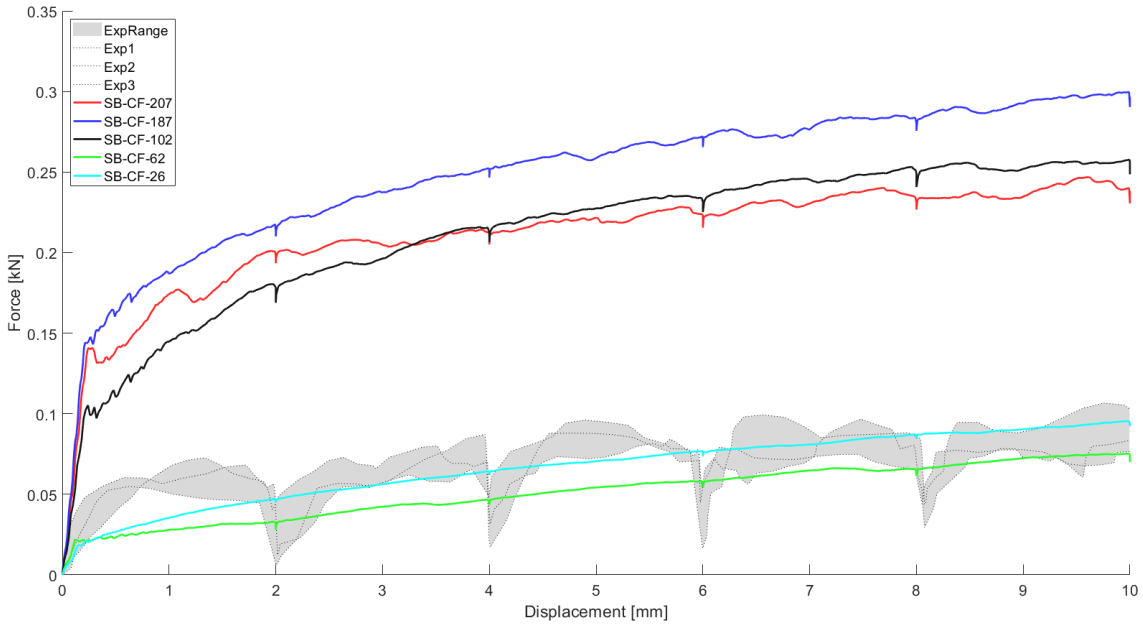

Figure 3.7 Force-displacement responses of solid bone SB-CF models and experimental data from Kulper et al. (2018) [26] using a flat-tip indenter

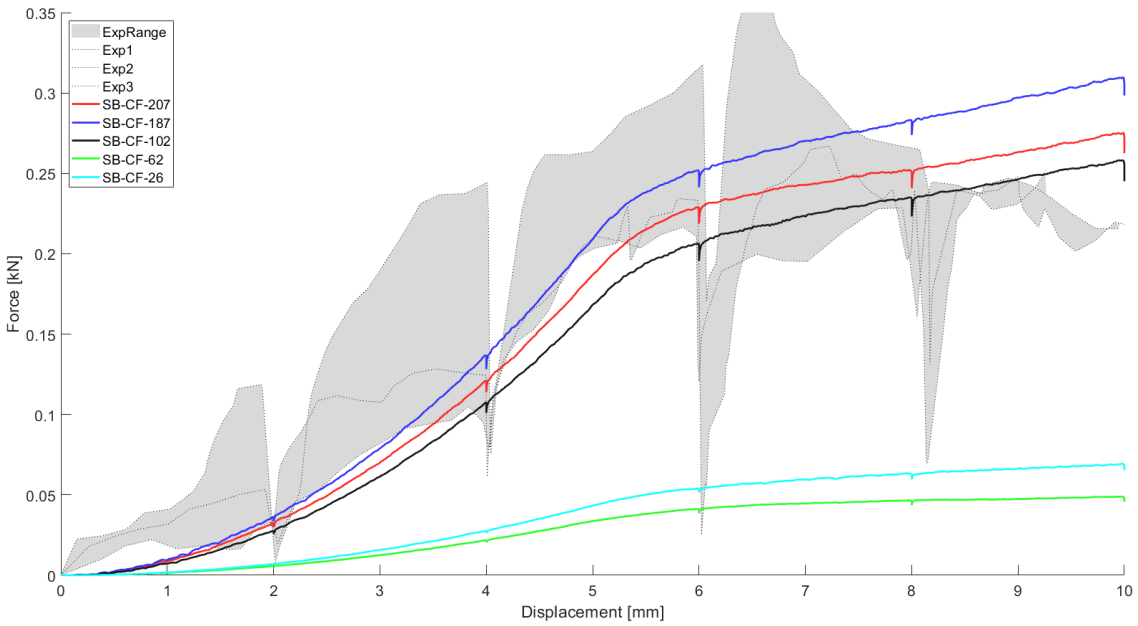

Figure 3.8 Force-displacement responses of solid bone SB-CF models and experimental data from Kulper et al. (2018) [26] using a sharp-tip indenter

Additionally, in both models, the range of BMD values used was able to envelop the reported experimental data. In the flat-tip indenter tests, the two material models representative of the least dense trabecular bone samples (SB-CF-26 and SB-CF-62) had force responses that were below the experimental findings throughout the test, and the material models based on the three denser specimens (SB-CF-102, SB-CF-187, and SB-CF-207) had force responses that were up to six times greater than the experiment. In contrast, experimental samples used in the indentation tests by Kulper et al. (2018) [26] had higher bone volume fractions than did the samples used in the flat-tip tests. Thus, the sharp-tip samples were generally stiffer, leading to greater force values in the force-displacement response. As a result, the simulations underestimated the experimental data with the two least dense specimens (SB-CF-26 and SB-CF-62) producing force responses that were up to five times weaker, and the other three denser specimens (SB-CF-102, SB-CF-187, and SB-CF-207) producing results that were much closer to the experimentally observed force response.

CORA scores evaluating the shape and phase of the response curves were determined, showing that, for both the flat-tip (Table 3.5) and sharp-tip tests (Table 3.6), the model performs well at representing the bone behaviour during densification. In all tests, the phase shift is perfectly modeled and in general, the flat-tip model does a slightly better job at representing the shape of the experimental responses.

Table 3.5 CORA Shape and Phase scores for each of the SB-CF flat-tip models, compared to the flat-tip experimental data

Model ID	SB-CF-26	SB-CF-62	SB-CF-102	SB-CF-187	SB-CF-207
CORA Shape Score	0.913	0.912	0.949	0.953	0.946
CORA Phase Score	1	1	1	1	1

Table 3.6 CORA Shape and Phase scores for each of the SB-CF sharp-tip models, compared to the sharp-tip experimental data

Model ID	SB-CF-26	SB-CF-62	SB-CF-102	SB-CF-187	SB-CF-207
CORA Shape Score	0.883	0.903	0.896	0.908	0.916
CORA Phase Score	1	1	1	1	1

The force-displacement response when using the SB-MPK material formulation in this SPH model showed much more instability than the SB-CF models, for both the flat-tip (Figure 3.9) and sharp-tip (Figure 3.10) simulations. This instability is believed to be due to failure definition of elements in the model during the progressive indentation of the material. The SB-MPK model was able to match the general shape of the curves for each of the flat- and sharp-tip indenter tests as evidenced by effective CORA scores evaluating the shape and phase of the response (Table 3.7). However, there was a significant difference between the measured

response with the SB-CF-187 model between the flat- and sharp-tip tests: with the flat-tip test, the SB-MPK model's response size is similar to that of the SB-CF-187 but it is six times weaker when using the sharp-tip indenter.

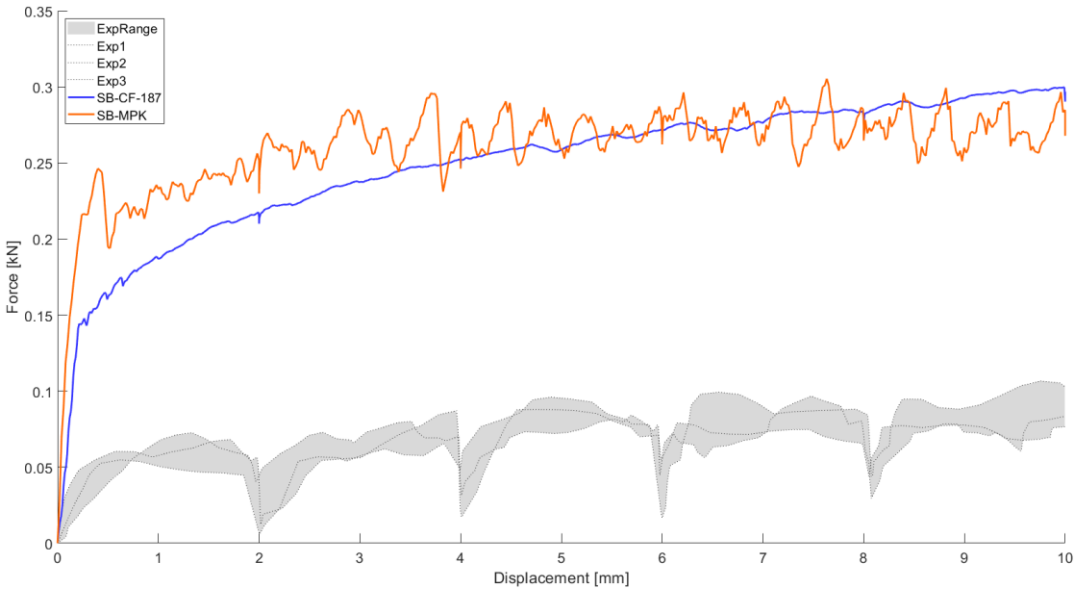

Figure 3.9 Force-displacement responses of the solid bone SB-CF-187 and SB-MPK models and experimental data from Kulper et al. (2018) [26] using a flat-tip indenter

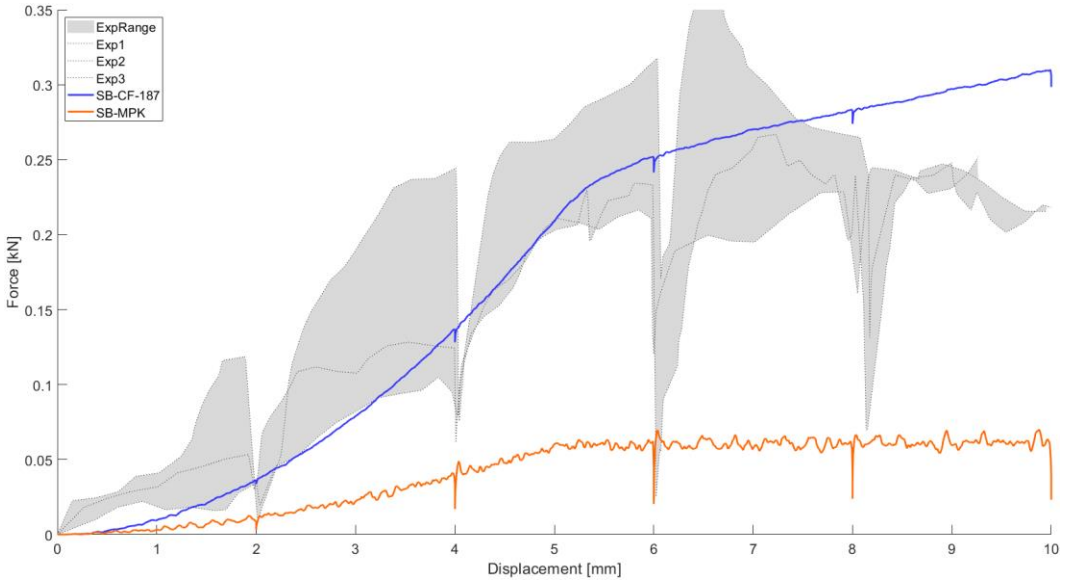

Figure 3.10 Force-displacement responses of the solid bone SB-CF-187 and SB-MPK models and experimental data from Kulper et al. (2018) [26] using a sharp-tip indenter

Table 3.7 CORA Shape and Phase scores for the SB-MPK model, compared to both the flat- and sharp-tip experimental data

Model ID	SB-MPK: Flat-Tip	SB-MPK: Sharp-Tip
CORA Shape Score	0.920	0.946
CORA Phase Score	1	1

Qualitative Results

The developed SPH model with the CF material model also demonstrated qualitative indentation behaviour of trabecular bone similar to previous imaging of trabecular bone damage (Figure 3.11 - Figure 3.14). With the flat-tip indenter, the regions of densification produced by the SB-CF and SB-MPK models differ. With the SB-MPK model, densification occurs all around the indenter when measuring bone densification based on the numerically determined plastic strain fields (Figure 3.11), following methods in the literature [26], [81]. The SPH method however also permits the visualization of the 'density' fields (Figure 3.12). When measuring the bone densification through the SPH density, the SB-MPK model exhibits densification directly beneath the indenter, but the thickness of the densified region is near constant throughout the simulation. In contrast, by measuring bone densification using both the plastic strain fields and the SPH density field, material densification occurs directly beneath the indenter in the SB-CF model, with an increase in densification thickness with increased indentation depth. The SB-CF performs better in matching the experimental findings from Kulper et al. (2018) [26] where they took photographs of trabecular bone densification from indentation. Experimentally, with a flat-tip indenter, bone densifies directly beneath the indenter with little bone densification occurring on the sides of the indenter. The thickness of

the trabecular bone densification region beneath the indenter increases, too, with increasing indentation depth.

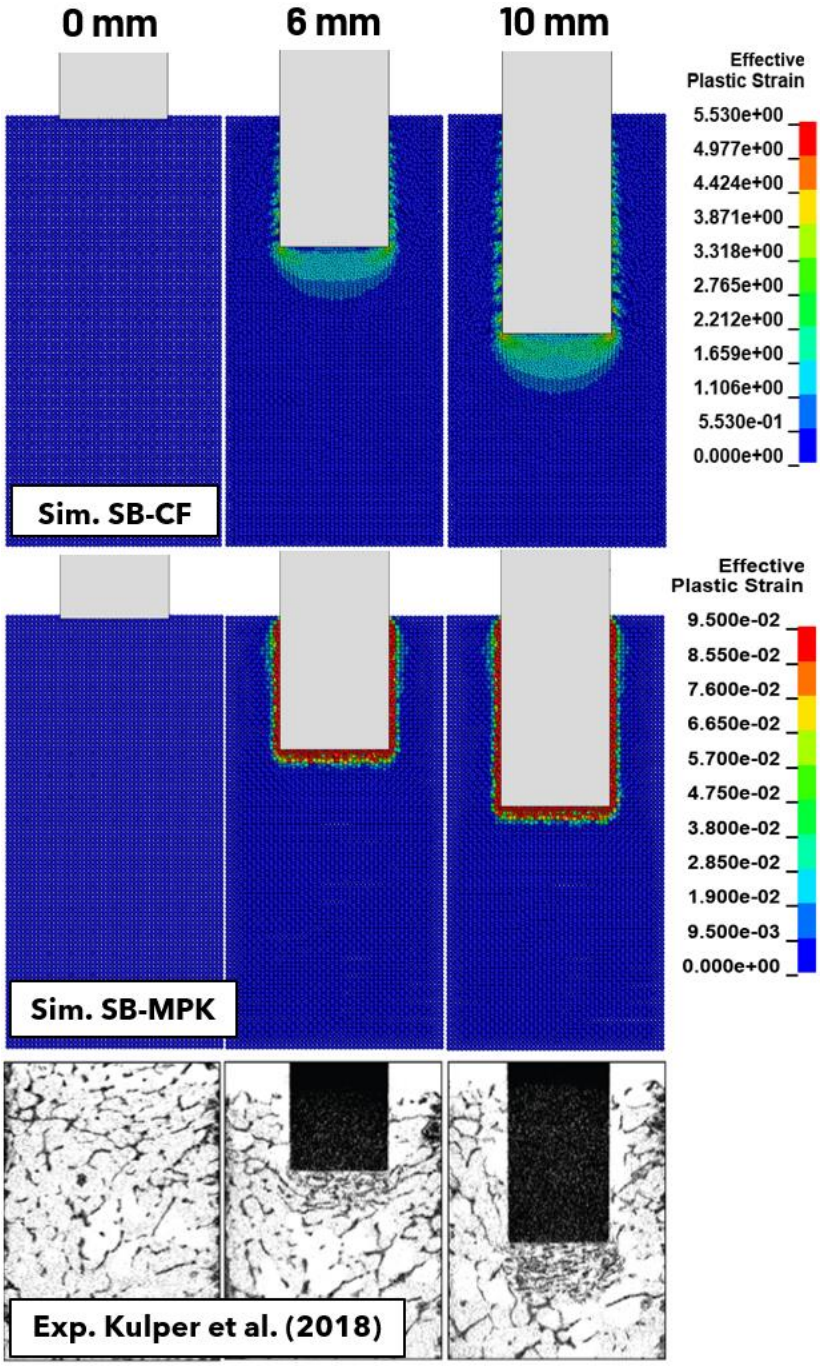

Figure 3.11 Computational plastic strain fields of trabecular SPH model with CF and MPK material models and experimental photographs adapted from Kulper et al. (2018) [26] at flat-tip indentation depths of 0, 6, and 10 mm demonstrating trabecular bone densification.

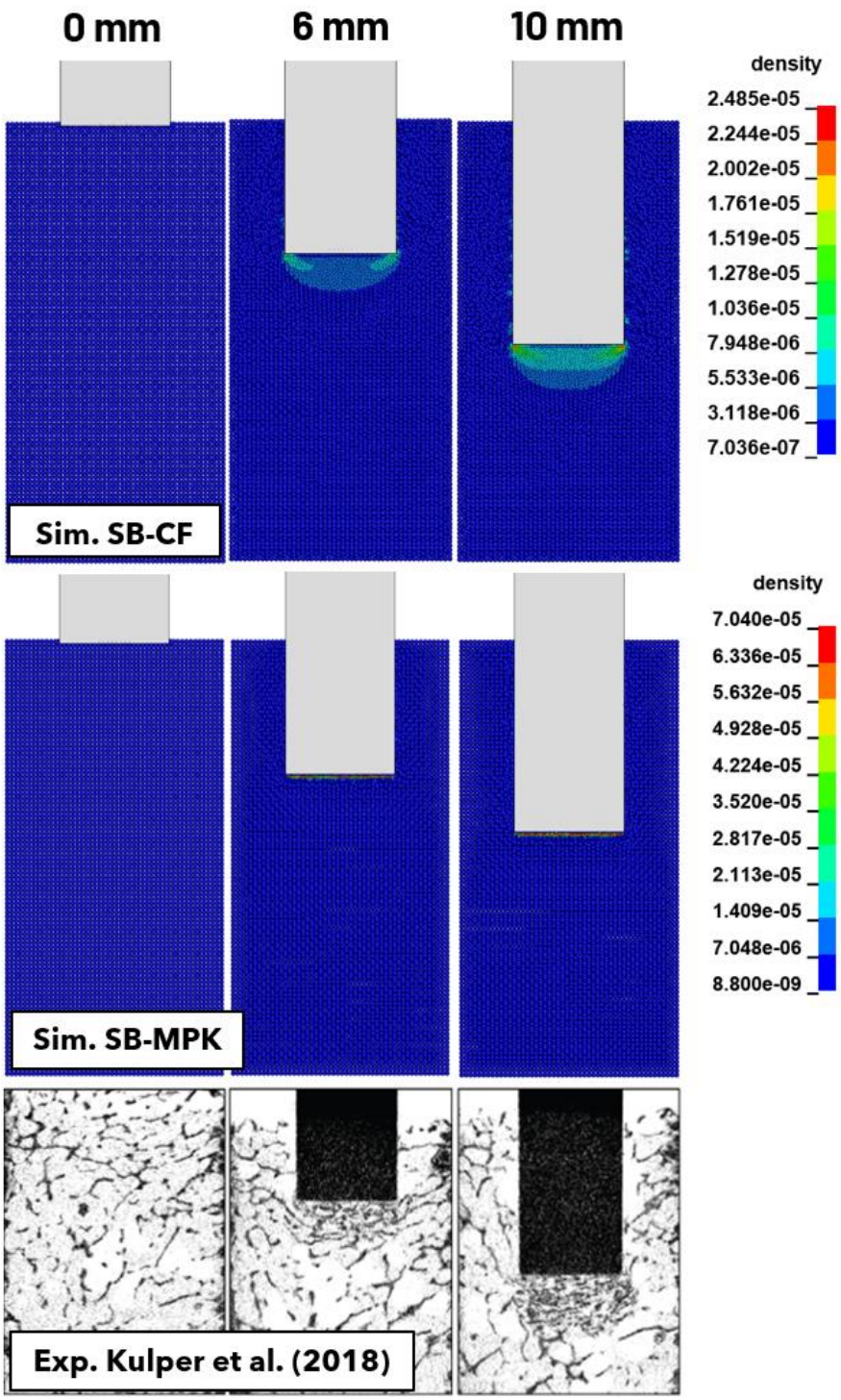

Figure 3.12 Computational SPH density fields of trabecular SPH model with CF and MPK material models and experimental photographs adapted from Kulper et al. (2018) [26] at flat-tip indentation depths of 0, 6, and 10 mm demonstrating trabecular bone densification.

With a sharp-tip indenter, densification of the trabecular bone initially occurs beneath the indenter experimentally, along the sides of its conical end, but with increased indentation, less pure crushing is occurring. The material is instead pushed away from the centerline of the specimen, and less material is concentrated near the tip of the indenter. Similar to the evolution of bone densification with the flat-tip indenter, the thickness of the densified region observed experimentally increases with increased indentation depth. In the sharp-tip simulations, the SB-CF model produces more accurate densification results than the SB-MPK model. Based on both the plastic strain fields and the SPH density field, material densification occurs around the sharp-tip indenter with less densification near the very tip of the indenter (Figure 3.13 & Figure 3.14). In contrast, the SB-MPK model, based on the plastic strain field, does not exhibit much evolution in the densification of material around the indenter: there is a near equal thickness of densified trabecular bone contacting the indenter at both 6 and 10 mm of indentation depth (Figure 3.13). There is also no variation in the thickness of the densified region at different points by the indenter. Observing the SPH density fields describes a similar story: the thickness of the densification region is constant between different indentation depths and all around the indenter (Figure 3.14). Further there is very little SPH densification following this measure.

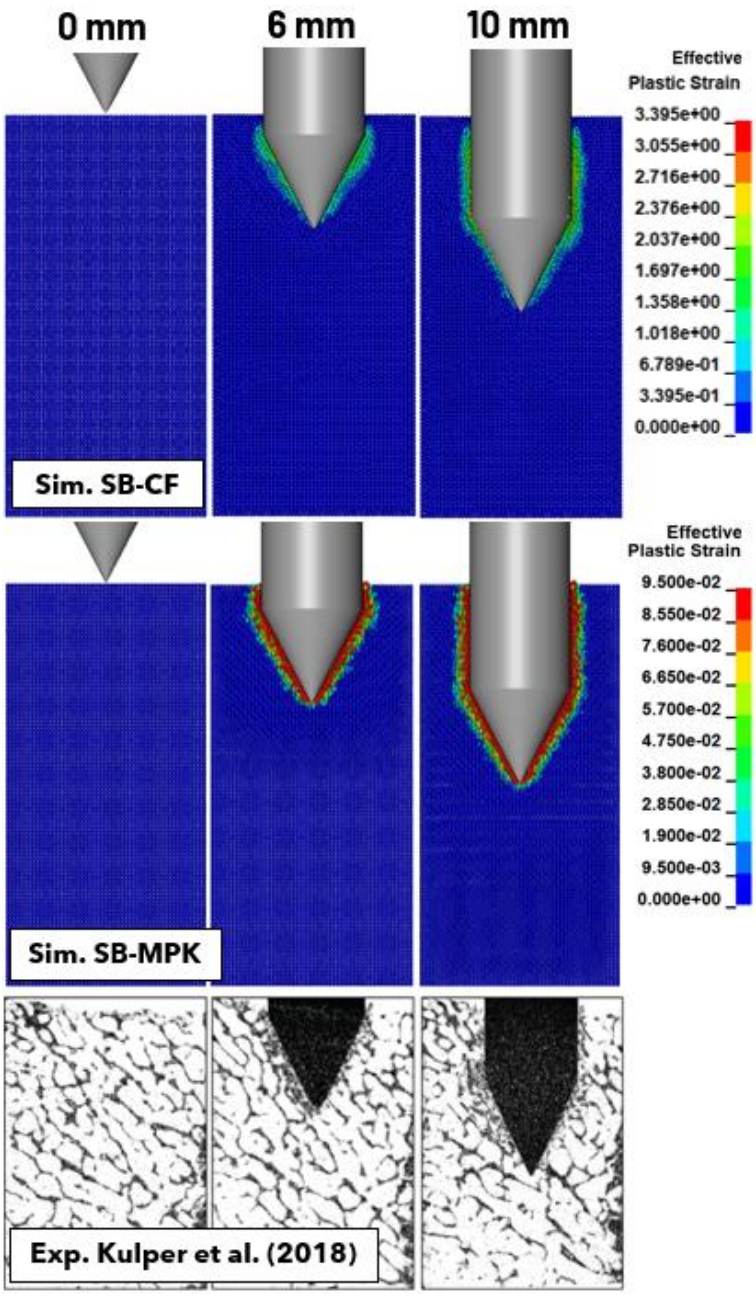

Figure 3.13 Computational plastic strain fields of trabecular SPH model with CF and MPK material models and experimental photographs adapted from Kulper et al. (2018) [26] at sharp-tip indentation depths of 0, 6, and 10 mm demonstrating trabecular bone densification.

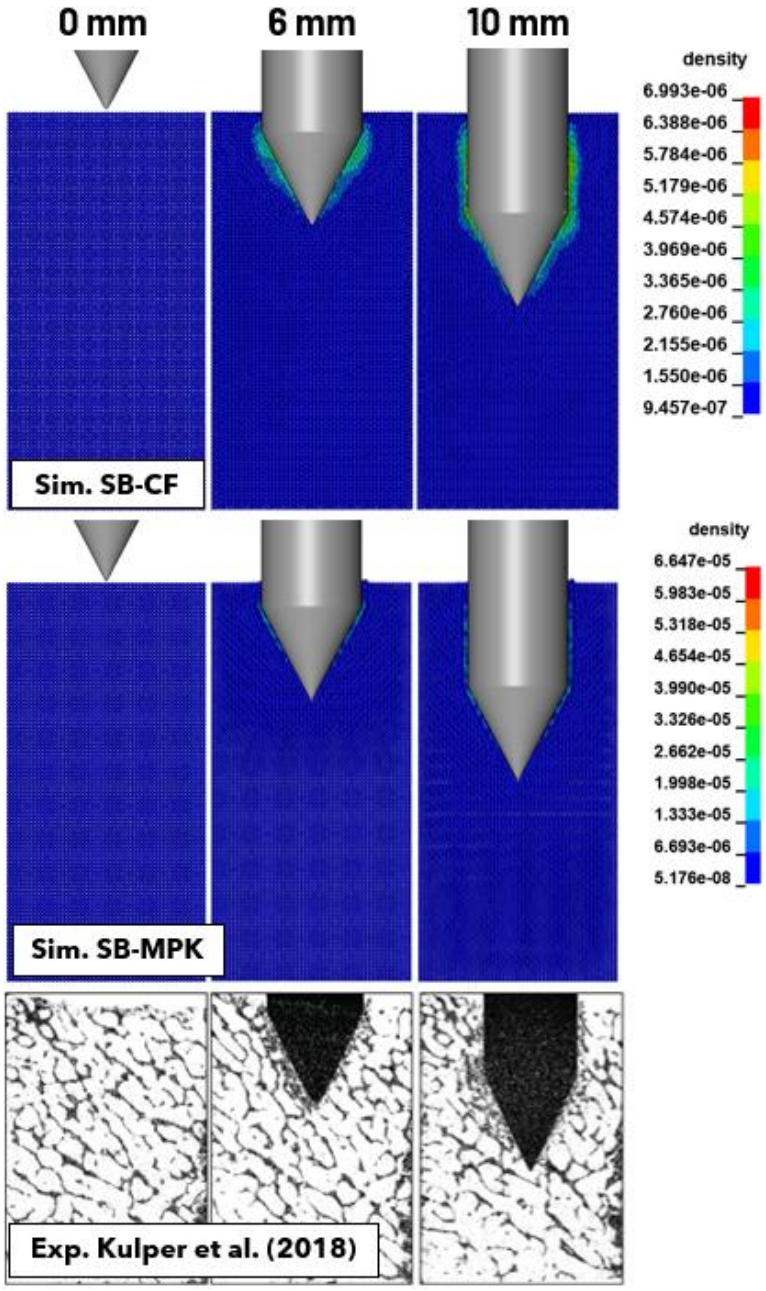

Figure 3.14 Computational SPH density fields of trabecular SPH model with CF and MPK material models and experimental photographs adapted from Kulper et al. (2018) [26] at sharp-tip indentation depths of 0, 6, and 10 mm demonstrating trabecular bone densification.

3.3.2 Bone-Marrow (BM) Model

Force-displacement plots for the flat-tip and sharp-tip indenter tests, including simulations for the SB-CF-187 model and the same model but with marrow elements included (BM-CF-187) and experimental data used for comparison were used for model assessment (Figure 3.15 & Figure 3.16). As shown in the flat-tip results, the responses are close to the experimental responses with each of the tested material models. The experimental specimens and corresponding FE model for the sharp-tip experiment had a greater bone volume fraction (on average approximately 28%) than those in the flat-tip experiments (18%). However, the model representing the sharp-tip indentation experiment still underestimates the force response.

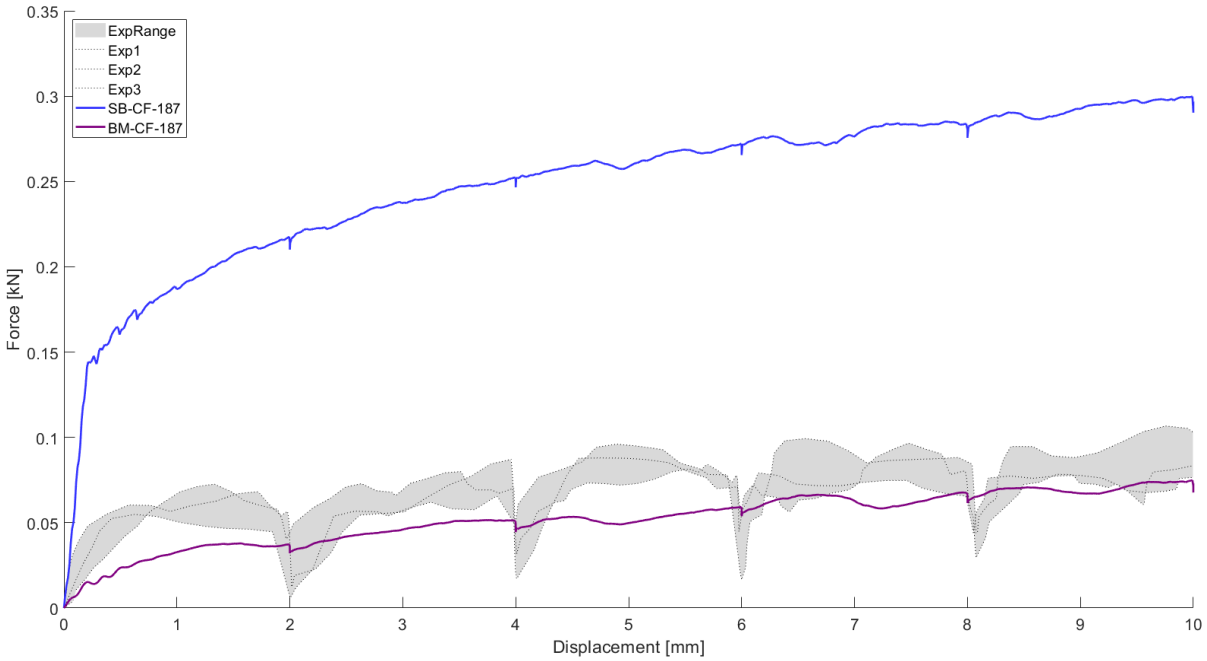

Figure 3.15 Force-displacement responses of the solid bone SB-CF-187 and bone-marrow BM-CF-187 simulations, and experimental data from Kulper et al. (2018) [26] using a flat-tip indenter

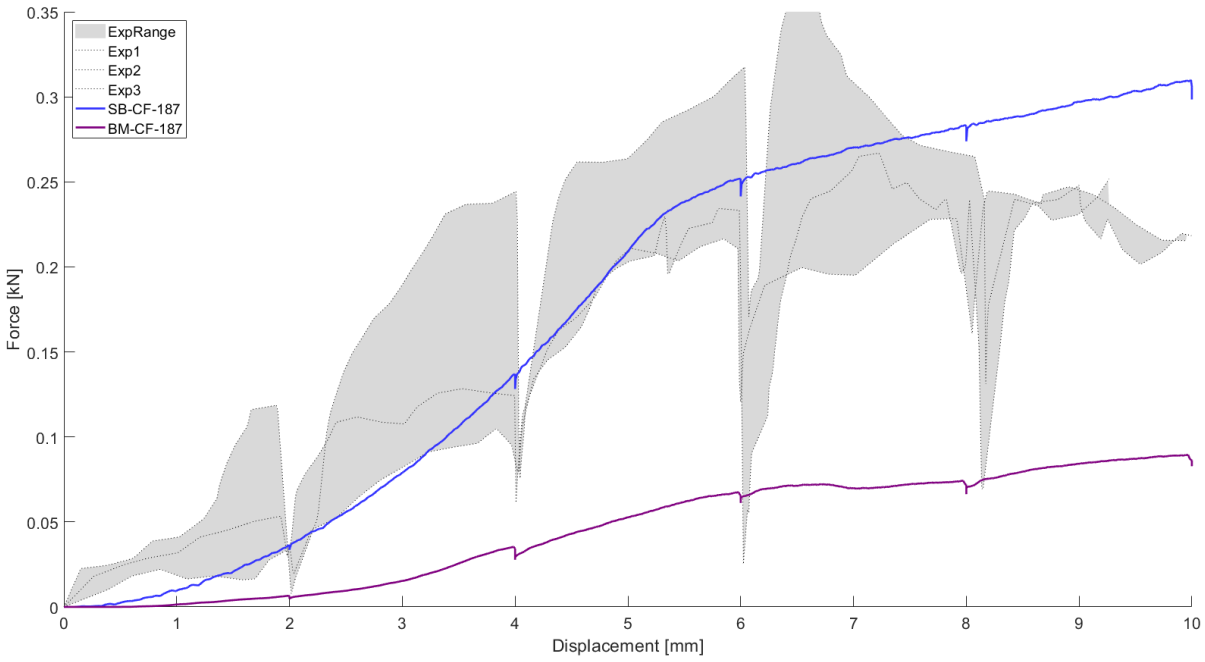

Figure 3.16 Force-displacement responses of the solid bone SB-CF-187 and bone-marrow BM-CF-187 simulations, and experimental data from Kulper et al. (2018) [26] using a sharp-tip indenter

CORA scores evaluating the shape and phase of the response curves were determined, showing that for both the flat-tip and sharp-tip tests (Table 3.8), the BM model performs well at representing the bone behaviour during densification, based on effective CORA scores for the shape and phase of the response curve. The shape score determined by CORA for the BM-CF-187 model is within the range of calculated scores for the SB-CF models in the flat-tip experiments. The shape score produced for this model in the sharp-tip configuration is slightly lower than those for the SB-CF models. In all tests, the phase shift is perfectly modeled and in general, the flat-tip model does a slightly better job at representing the shape of the experimental responses.

Table 3.8 CORA Shape and Phase scores for the BM-CF-187 model, compared to the flat-tip and sharp-tip experimental data

Model ID	BM-CF-187: Flat-Tip	BM-CF-187: Sharp-Tip
CORA Shape Score	0.925	0.868
CORA Phase Score	1	1

3.4 Discussion

In the present study, the effectiveness of a CF material formulation coupled with a continuum-based geometry using SPH elements was examined for representing trabecular bone behaviour during indentation. FE simulations revealed that the main contributing factors to the shape and magnitude of the force response curves were the elastic modulus, yield strength, and hardening evolution definition, with the models being less sensitive to other mechanical property input (i.e. Poisson's ratios, yield stress ratio, friction coefficient). Further, the large reported variation in force-displacement responses from the different specimens tested in the SB model stemmed from a significant difference in the mechanical properties for the tested experimental samples from Soltanihafshejani et al. (2021) [27] from which the material models were built using the five reported BMD values. It should also be noted that the experimental specimens from their work that were modeled in this study were generally stiffer than the regression curve they developed to build the empirical relationships between BMD and CF input material formulation properties. As a result, there may be some error in the reported dimensionless mechanical properties that cannot be directly interpreted from the uniaxial stress strain curves (i.e. Poisson's ratios, yield stress ratio).

Significant differences in the force responses for each of the material models were observed between the flat- and sharp-tip indenter simulations, both in shape and magnitude. The flat-tip indenter simulations can be characterized by the crushing and densification of bone beneath the indenter. Densification of SPH elements occurred primarily beneath the indenter as seen visually in the model and evidenced by higher levels of plastic strain and stress observed in the elements in proximity or in direct contact with the bottom face of the indenter. This is demonstrated qualitatively, with bone crushing and compaction behaviour that were

consistent with findings from Kelly et al. (2013) [81] and Kulper et al. (2018) [26], both of whom performed experimental indentation testing of trabecular bone. This behaviour is also observed in the force-displacement plots for these tests as there is a steep slope in the force response for small amounts of displacement as the bone is being compacted beneath the indenter. A shallower slope follows this as the bone continues to densify as the indenter drives the compacted bone further into specimen, which contributes to the hardening of the response curve but with parts of the bone shearing off and contributing to the reduced slope. Contrasting this, the sharp-tip indenter results illustrate the shearing of bone and densification on the sides of the indenter. As the indenter subsides into the bone, bone is displaced from the center and concentrates on the sides where it is left in a compacted state, which is consistent with findings from Kulper et al. (2018) [26]. Due to the conical shape of the indenter used in this experiment, less bone material is displacement throughout the test. Particularly, the conical section of the indenter is 4.8 mm tall and, from the results, the sharp-tip data plateaus near that amount of total indenter displacement.

CF material formulations are recognized as effective analogues for trabecular bone due to the cellular structure of both trabecular bone and foams [55]. In general, the CF material formulation used in this study was able to capture the force response of trabecular bone during indentation very well. The SB-CF models produced favourable results in modeling the crushing and densification behaviour of trabecular bone compared to the SB-MPK material model that does not consider pressure dependence in its yield criterion. The SB-MPK model performed less well in capturing the post-yield behaviour of trabecular bone based on notable instability in the post-yield region of the force-displacement curves. Additionally, there was a much greater discrepancy in the size of the response between the flat- and sharp-tip indenter

tests compared to the SB-CF models. Further, the qualitative representation of the crushing and densification phenomena during trabecular indentation was not represented as well with the SB-MPK model compared to the SB-CF models with its representation of bone densification being inconsistent with the experimental photographs. The SB-CF models instead provided results that effectively matched the experimental force-displacement responses, producing effective curve shape and phase scores computed by correlation and analysis software. Improved representation of the evolution of bone densification with increasing indentation depths, comparing with experimental photographs, was also observed. These findings support previous work on material models with pressure-dependent yielding and their benefits for modeling the post-yield behaviour of trabecular bone [63], [81].

The utilized SPH formulation demonstrated advantages in modeling bone crushing that was not possible with Lagrangian formulations in a computationally effective manner. However, the significant depth of the indentation test greatly contributed to the run-time of the simulations: simulations modeling less localized crushing ran quicker. This may have been due to the link between the computational cost of the model and the non-linear effects that are captured at higher levels of deformation in the test.

SPH allows for the densification of the bone material to occur and the subsequent "shearing-off" where material failure occurs. It also poses advantages for this sort of experiment over other FE methods since this three-dimensional problem was able to be studied without the need of mass removal or user intervention in pre-defining failure paths or with computationally intensive re-meshing protocols. The proposed methodology offers benefits over the computational results by Kulper et al. (2018) [26] where they employed a softened

elastoplastic material formulation that was optimized using a power-law with a best-fit approach. Their results with both indenter types do not accurately capture the phase-shift or shape of the curves, particularly in the sharp-tip results where their simulations tend to overestimate the responses, despite the best-fit approach in creating the material model.

While noted that the SB-CF model simulations in this study mimic the shape of the experimental force response curves very well, there is a gap in the magnitudes between the two different indenter types. The results for the flat-tip indenter scenario tended to overestimate the response while the same material models underestimate the response with the sharp-tip indenter scenario. The experimental specimens for the flat-tip tests had bone volume percentages ranging from 17.88 to 18.85%, while the sharp-tip test specimens had bone volume percentages ranging from 26.63 to 30.49%. As a result, the sharp-tip indenter experimental specimens led to stiffer results and the simulations carried out by Kulper et al. (2018) [26] are stiffer too by virtue of using CT-based geometry. Furthermore, the empirical relationships relating CF material input parameters to specimen BMD by Soltanihafshejani et al. (2021) [27] were developed from trabecular bone specimens where the bone marrow and other fluids were removed. The presented model shows overestimation in the flat-tip results, which was suspected due the continuum-based geometry versus the CT-based model that includes empty spaces between trabeculae and thus bone only occupies 18-30% of the total volume in their models. The presented model did not employ any techniques to reduce the stiffness of the model either through the material or through the geometry by incorporating the voids present between the trabeculae in a CT-based model.

To address this issue, the BM models were developed. In the flat-tip tests, the BM model produced effective results at capturing the response of the experimental trabecular bone

samples, supported by good correlation scores assessing the shape and phase of the curve compared to the experimental data. In comparison to the SB models, the BM approach performed better in its ability to match the force-displacement magnitudes and the shape of the curve. The BM method significantly reduced the stiffness of the whole simulated system since 72-82% of the elements were modeled with an elastic material model with greatly reduced stiffness relative to the CF material model applied to the bone elements. The peak force in the BM models were reduced by a factor of 4.03 and 3.48 in the flat- and sharp-tip indenter tests, respectively, compared to the results from the SB model used for comparison. Additional testing revealed that the model was very sensitive to the marrow material input parameters; however, with limited experimental data available for marrow properties, estimation of marrow behaviour was input as a simplified elastic formulation. The lack of research regarding the information on the yield and post-yield mechanical properties of bone marrow leads to some uncertainty on the suitability of this perfectly elastic material formulation, especially in the context of simulating damage and the post-yield behaviour of bone.

Applying the BM method to the sharp-tip setup with 28% of SPH elements representing bone and 72% representing marrow was less effective. The simulation underestimated the experimental results despite there being more ‘bone’ elements in these models compared to the flat-tip models based on the reported trabecular bone volume fractions [26]. It is believed that the CF performed less well in the sharp-tip tests due to the material definition. The CF material formulation in LS-Dyna (LS-Dyna 12.1, LST, Livermore, California, USA) is calibrated using uniaxial compression data and incorporates strength interactions with hydrostatic pressure, but the simplifications of the material model come with the disadvantage that material orthotropy cannot be included. In the flat-tip tests, the bone material undergoes a state of nearly pure

crushing with minimal shear or other loading modes occurring as the indenter displaces deeper into the bone specimen. In the sharp-tip tests, a significant amount of bone material is subjected to shear loading, a loading mode that is not addressed in the CF material formulation definition. This rationalizes the model's good performance in the flat-tip tests and reduced effectiveness in the sharp-tip configurations.

The original purpose of performing sharp-tip indentation tests from the Kulper et al. (2018) study was to capture the behaviour in situations including pedicle screw insertion. However, the targeted application of this thesis is implant subsidence, and, as such, the results are deemed favourable since the bone-implant interface conditions of the flat-tip indenter scenario would be similar to typical interbody implants and the underlying vertebral. Further, the CF material formulation does not require many independent material parameters along with the uniaxial compressive stress-strain response, which can all be related to the underlying trabecular bone density. As a result, adaptation to other anatomical sites or to different strength-density relations is straightforward and the CF material model is available in most commercial FE solvers, making it an effective tool for bone damage prediction.

3.4.1 Limitations and Future Work

There are some limitations and considerations for future continuation of this work. Since this study was focused on validating a trabecular bone material model against available data from the literature, it was difficult to build material models that are perfectly representative of the experimentally tested bone samples, as important details regarding the test samples were unavailable. As such, while the constructed SB models represent the bone behaviour well and envelop the previously reported experimental data, the model's ability to accurately represent the experimental specimens' behaviour in indentation including the size

of the responses given input material parameters specific to the experimental specimens used for validation is unknown. Further, the experimental data used for validation was limited by its sample size. While the presented models could accurately capture the behaviour of trabecular bone in crushing through the shape of the force response curves and through the qualitatively measured compaction of bone throughout the test, its performance in load cases with a significant amount of shear was limited. Moreover, the existing material properties in the literature for bone marrow and other constituents of the inter-trabecular spaces is very limited. Previous computational work with bone marrow has only modeled it as an elastic material and its yield and post-yield behaviour experimentally is yet unknown. To add, trabecular bone is known to have a preferential alignment according to typical load paths. Assignment of 'bone' and 'marrow' elements in the BM models was done stochastically, neglecting this microstructural quality. Further, the correlation and analysis software used to assess agreement between the simulations and the experimental data has inherent limitations: it is highly dependent on the input parameters that were based on standard values when applying CORA to the validation of human body kinematics. It is unknown if these same input parameters are suitable for orthopaedic problems like the one described in this study. To add, computed results from CORA may not be statistically significant. Lastly, convergence in this study was not fully achievable for reasons of computational cost. While the overall conclusions made in this study as well as the resulting material behaviours reported are not expected to differ with an increasingly finer mesh, errors were encountered with a very high SPH element density, over-stiffening the system.

Future work should look to include performing a series of experimental testing to produce generalized post-yield stress-strain curves representative of different populations for

the material input. Furthermore, more research on the methods of representing the constituents present in the inter-trabecular spaces would improve the performance of the presented models. Finally, exploring alternative material formulations to address the limitations of this study's models in accurately simulating loading modes aside from uniaxial and hydrostatic compression would improve its predictive capabilities for trabecular bone damage, crushing, and densification for a wider variety of test load paths that could create more complex stress states.

3.5 Conclusion

This study shows promising results in both the ability to create relatively simple FE models representative of different BMD values, and the ability to accurately match the quantitative and qualitative responses of the post-yield behaviour of trabecular bone in crushing. The SPH method and its application in the modeling of trabecular bone has not been widely explored despite the promising applications for predicting trabecular bone damage, and despite its flexibility in representing composite structures. Additionally, CF models, thanks to their pressure-dependent yielding quality, have demonstrated improved post-yield response in comparison to other material formulations. The present work will help support future research towards accurate prediction of trabecular bone crushing and its post-yield behaviour, which could be leveraged for improving the pre-clinical prediction of implant subsidence.

Chapter 4

Evaluation of a new ‘force-control’ method to perform unconstrained load-induced subsidence[2]

4.1 Introduction

Following spinal fusion surgery, intervertebral column support is often required while the spine heals. This support is provided by interbody implants that are often inserted between the remaining vertebrae. These implants help to preserve sagittal spine alignment throughout the healing process until solid osseous union is achieved [138]. However, a prevalent failure mode of these interbody cage implants is axial and/or rotational subsidence into either of the adjacent vertebral bodies, due to material stiffness and geometrical conformance mismatch between the implant and bone [81], which can introduce significant stress concentrations in the underlying trabecular bone. However, the ability to predict vertebral bone failure patterns remains limited.

Clinical studies have shown that rotation of the implant can occur following interbody fusion procedures, causing progressive changes in spinal alignment [8]. Further, the vertebral body has been shown to exhibit regional differences in mechanical properties [144], [145] with the vertebral periphery being stronger than the central portion of the body, making it more resistant to implant subsidence [138], [147]. Additionally, the anisotropic nature of trabecular bone makes the body more vulnerable to implant subsidence from specific loading modes

[2] The research presented in this chapter will be submitted for review as a manuscript.

[140], [141]. As a result, *in vivo* loads applied to vertebral bodies from interbody cage implants can involve complex shear and rotational vectors alongside axial forces [151].

ASTM F2267 is the sole test method designed to assess interbody cage implants' resistance to subsidence. However, it involves loading a system composed of an interbody cage implant and PU foam under uniaxial compression, neglecting any consideration for other loading modes [149]. Further, material characterization studies of trabecular bone have predominantly studied the bone under uniaxial compression tests [15]–[20]. Few *in vitro* studies have incorporated unconstrained loading of these implants where the implant was free to translate and rotate in and about all uncontrolled axes [152]–[155], but their methods have only been applied to the assessment of interbody cage implant stabilization and have not been applied to the prediction of axial and rotational implant subsidence.

PU foam is an industry standard trabecular bone surrogate used in biomechanical testing due to its similar microstructure [66] and its mechanical behaviour with its elastic behaviour fitting within the reported ranges of trabecular bone properties [62], [157]. Additionally, a variety of bone specimens can be represented in experimental studies based on the chosen foam density. Similar to trabecular bone, the compressive stress-strain response of PU foam can be described by three stages: (1) the beginning linear elastic region at low stresses and strains, (2) a stress plateau, and (3) a steep increase in stress representing densification of the crushed material. As such, previous computational studies have modeled PU foam using a CF material formulation [28], [29], [63], [81]. The study in Chapter 3 showed that the pressure-dependent CF model with isotropic hardening can accurately capture the pre- and post-yield behaviour of trabecular bone in uniaxial indentation. Additionally, the SPH approach used

offered advantages for represented the crushing and densification phenomena characteristic of the post-yield responses of trabecular and PU foam alike.

Therefore, this study aimed to (i) develop a novel experimental method for conducting unconstrained load-induced subsidence of a bone surrogate and to (ii) compare the findings with the current ASTM test method in terms of rotational implant subsidence about a defined bone material interface. Additionally, the FE model developed in Chapter 3 was calibrated to represent the PU foam materials used in this study and the experimental data collected would (iii) supply validation for the computational FE model. It is hypothesized that such an experimental setup would allow for freer (frictionless) translation and rotation in the unloaded axes relative to the existing test standards and provide a better approach for examining load-induced axial and rotational subsidence.

4.2 Experimental Methods

4.2.1 Test Materials

Closed-cell rigid PU foam (Sawbones, Sawbones Europe AB, Sweden) was selected in two densities to model a transition zone in mechanical properties of trabecular bone. The mechanical properties in uniaxial (Table 4.1) and confined compression (Table 4.2) for the chosen samples of PU foam (20 and 30 PCF) are listed below.

Table 4.1 Elastic Modulus and Yield Stress of 20 and 30 PCF PU foams in Uniaxial Compression

PU Foam	Author	Elastic Modulus (MPa)	Yield Stress (Mpa)
20 PCF	Sawbones [162]	210	8.40
	ASTM F1839-08 [163]	167.5-257.5	6.63-10.50
	Issa et al. (2023) [28]	257	7.73
	Schulze et al. (2018) [29]	230	4.43
	Thompson et al. (2003) [164]	164	5.14
	Patel et al. (2008) [165]	145	3.30
	Calvert et al. (2010) [166]	195	8.40
30 PCF	Sawbones [162]	445	18.00
	ASTM F1839-08 [163]	356-549	14.3-22.7
	Issa et al. (2023) [28]	482	14.30
	Schulze et al. (2018) [29]	391	11.00

Table 4.2 Elastic Modulus and Yield Stress of 20 and 30 PCF PU foams in Confined Compression

PU Foam	Author	Elastic Modulus (MPa)	Yield Stress (MPa)
20 PCF	Issa et al. (2023) [28]	271	10.20
30 PCF	Issa et al. (2023) [28]	456	18.40

The PU foam specimens were cut into rectangular prisms (22.4 x 11.2 x 22.4 mm) and were sandwiched together in 31.8 mm square hollow steel tubing (25.4 mm in length). These sandwiched foam materials of different densities provided a boundary to induce implant rotation with load-induced subsidence (Figure 4.1). The tubes with foams were then press-fit in the cut-out of a steel plate to hold its position. An additional steel plate with the same cut-out was added and offset vertically to prevent the tube from rotating out of the lower plate during the experiment.

A cervical interbody cage implant was 3D-printed in a titanium alloy (Ti-6Al-4V) by electron beam melting and placed along the boundary of the two sandwiched foams (Figure 4.1). The implant used in these tests' size had a 0° lordosis angle and had the following dimensions: 16 x 12 mm with a height of 10 mm. A 3D-printed jig was designed and used to align the implant in the center of the sandwiched foams with its plane of symmetry being inline with the foams' boundary plane.

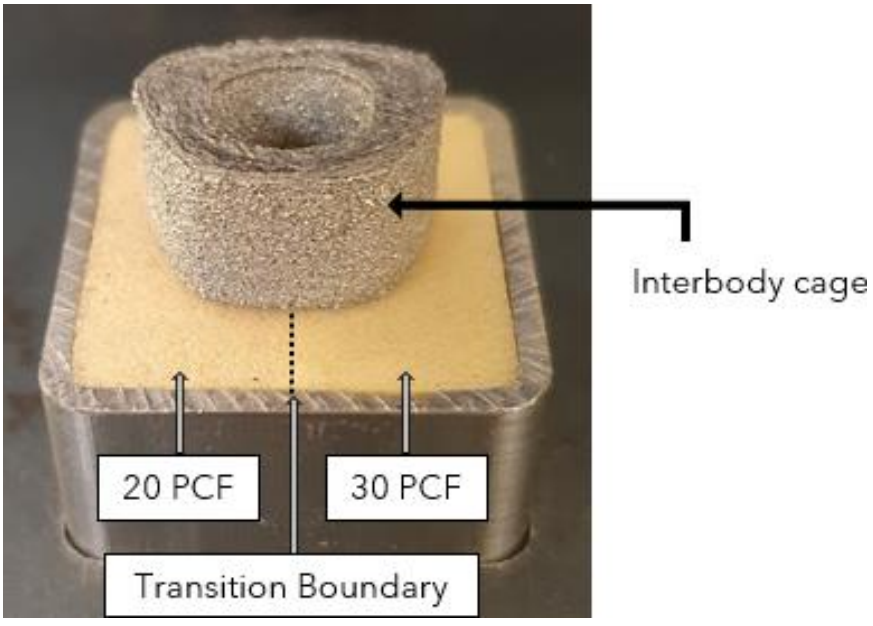

Figure 4.1 Foam-Implant system setup, including two rectangular foam blocks sandwiched in hollow steel tubing and an interbody cage implant centered on the specimen

4.2.2 Test Setups

The first method used a testing fixture inspired by the ASTM F2267 method, including a lubricated ball-and-socket joint (BSJ) for unconstrained loading under axial compression (Figure 4.2). A 20 N axial pre-load was applied to the foam-implant system via the BSJ fixture before applying a linear ramp load up to 4 kN in axial compression. The remaining degrees of freedom afforded by the test machine were fixed so that the test machine acted as a 1-DOF compression tester to follow the guideline outlined in the ASTM F2267 standard (Figure 4.2).

A second novel method was developed in this study using the six-axis force-control (FC) capabilities of the VIVO Joint Motion Simulator (AMTI, Massachusetts, USA), where the same magnitude of axial compression (up to 4 kN) was applied as the ASTM test, but with the remaining force and moment axes set to hold no load in force control (Figure 4.2 & Figure 4.3). The gain settings of the force control axes were tuned for responsiveness through pilot testing.

Twenty-four specimens were tested in total, split equally between the two fixturing setups. Twelve total samples of sandwiched foam were machined. The top and bottom faces of the foam block – steel tubing systems were tested independently. In each test, the relative position of the two PU foam samples was kept consistent, so that the "flexion" arm would allow for implant rotation about the foam interface boundary. This was done since this arm and direction of rotation offered the greatest range of motion. Additionally, this eliminated possible variability in results between different rotational axes from the VIVO. Detailed test procedures for each of the FC and BSJ tests are included in Appendix A.

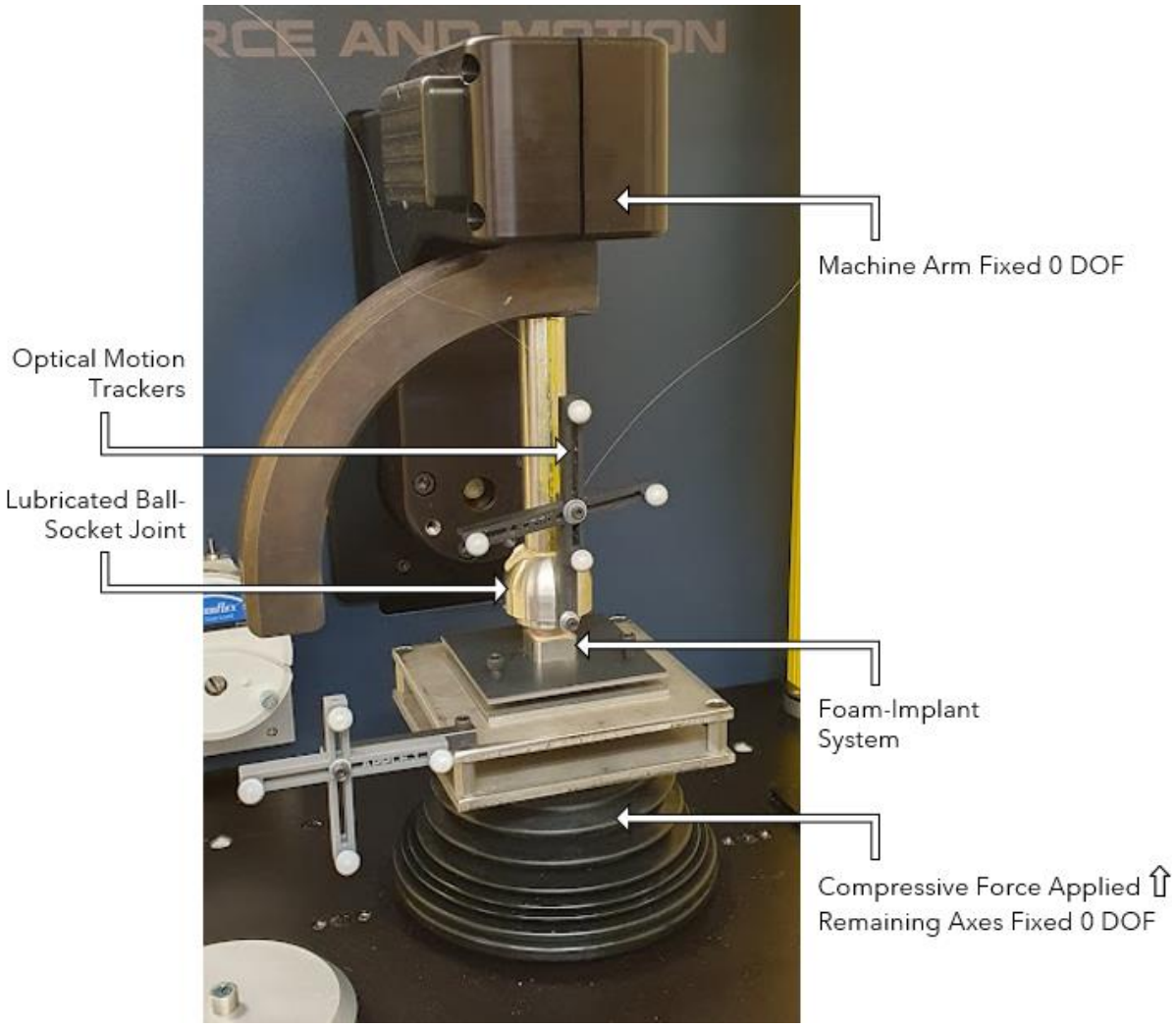

Figure 4.2 Ball-socket joint (BSJ) test setup

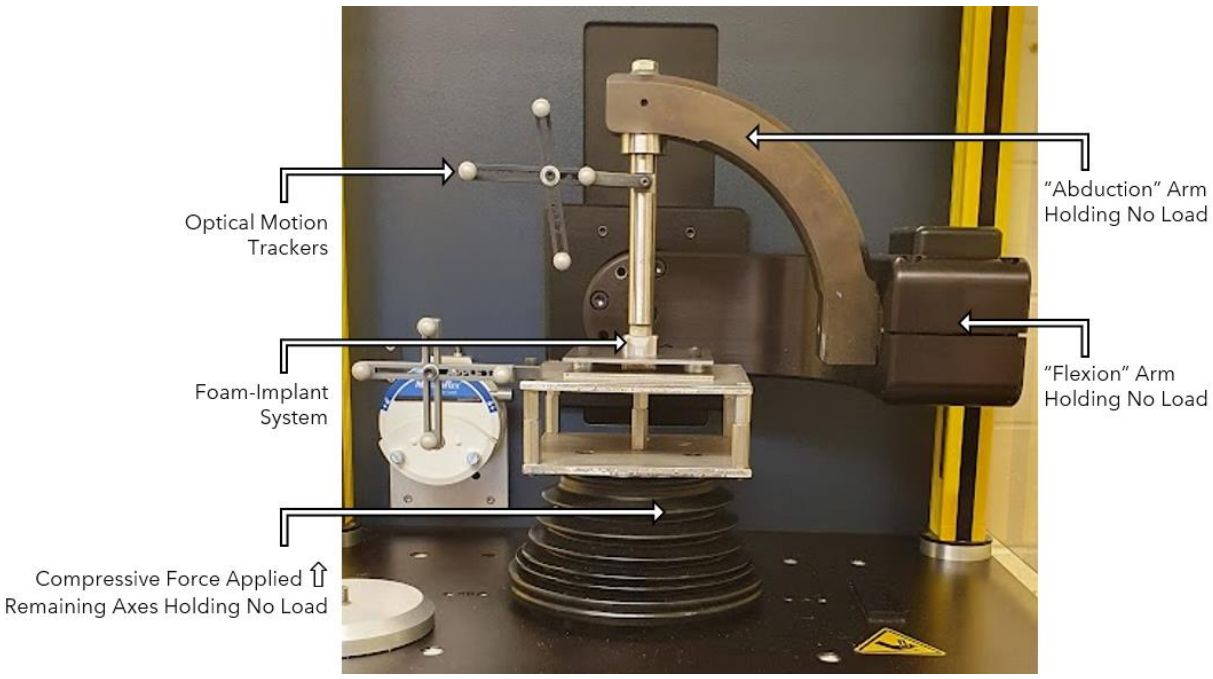

Figure 4.3 Force-control (FC) test setup

4.2.3 Data Capture and Analysis

Optical motion trackers (Northern Digital Inc., Ontario, Canada) were placed on the shaft that transfers the load to the implant to measure the displacement of the implant throughout the test and to the steel plates beneath the foams to serve as a reference. A Polaris optical motion tracking camera (Northern Digital Inc., Ontario, Canada) was used to measure the rotations and displacements of these trackers. A transformation algorithm (MATLAB R2023b, The Math-Works, Inc., Massachusetts, USA) (Appendix C) was used to convert the translational and rotational displacement measurements of the trackers relative to one another to the translational and rotational displacements of the interbody cage implant relative to the top surface of the PU foam throughout the experiment. The axial and rotational subsidence of the implant into the PU foam was interpreted from these results. The average results for each the BSJ and FC test methods were then compared.

CT Imaging

CT scanning (InCiTe 3D X-ray Microscope, KA Imagine, Ontario, Canada) and reconstruction (VGStudio 2023.4, Volume Graphics, Stockholm, Sweden) of one specimen from each test setup was performed to make qualitative assessments on failure and subsidence as supporting evidence for the quantitative results based on the densification pattern observed experimentally. Greyscale intensity measurements from the CT scan were taken at equal distances from the top of the crushed densified foam region. These, along with greyscale intensity measurement far away from the densified region, were used to make relative assessments of the densification observed in the sample from the FC and BSJ tests. Settings for the CT scanning are displayed in Table 4.3. CT reconstruction parameters included logarithmization and filtered back projection, a Shepp-Logan filter for preprocessing, low projection smoothing, medium ring artifact reduction, and no beam hardening correction (except for the physical filter).

Table 4.3 CT Scan Settings

Parameter	Value
Tube Potential (kV)	60
Tube Current (µA)	190
Integration Time (ms)	1000
Averaging (frames)	5
Angular Increment (deg)	0.36
Number of Projections	1000
Angular Section (deg)	359.64
Source-Object (mm)	410
Source-Detector (mm)	480
Sample Height (mm)	0
Lateral Position (mm)	0
System Resolution (µm)	6.93
Effective Pixel Size (µm)	6.83
Magnification	1.17
X-Ray Focal Spot	8
Filter	0.5mm Al Filter

4.3 Modeling Methods

Explicit FE simulations (LS-Dyna 12.1, LST, Livermore, California, USA) of unconstrained indentation of PU foams was also performed, following the same test setup as the experimental FC setup in this study. The general FE modeling approach developed in Chapter 3 was adapted to this study as described below. Following the results of a convergence analysis, 262,144 SPH elements were implemented in a 25.4 mm cube where one half was assigned material properties for 20 PCF PU foam and the other 30 PCF PU foam.

4.3.1 Material Modeling

The previously developed CF material model was used to model the PU foam specimens. Due to the wide range of reported mechanical properties for the tested PU foams (Table 4.1), two CF material models were constructed with the material parameters identified based on experimental uniaxial compression testing performed by Issa et al. (2023) [28] and Schulze et al. (2018) [29]. Since Schulze et al. (2018) did not report the yield stress ratio and elastic and plastic Poisson’s ratios found in their experimental specimens, the yield stress ratio and elastic Poisson’s ratios reported by Issa et al. were applied. The plastic Poisson’s ratio reported by Kelly et al. (2013) [81] was applied to all material models of PU foam, since this parameter was not reported by neither Issa et al. (2023) [28] nor Schulze et al. (2018) [29]. A single element fitting procedure was performed for each of these material models to achieve a best fit for the reported experimental stress-strain curve, in the same method followed in Chapter 3. The determined material input parameters for each of the CF models for each material are displayed below (Table 4.4).

Table 4.4 Material input parameters for the CF models used for 20 and 30 PCF PU foams following single element fitting procedure

Model ID	**CF-Issa**		**CF-Schulze**	
Material Density (PCF)	20	30	20	30
Compressive modulus (MPa)	200	350	230	391
Yield Stress ratio (K)	0.933	0.86	0.933	0.86
Elastic Poisson's ratio	0.350	0.36	0.350	0.36
Plastic Poisson's ratio	0.339	0.36	0.339	0.36

4.3.2 Boundary Conditions

To capture the confined nature of the experiment, five rigid walls were positioned in-plane with the bottom and side faces of the foams. The implant was meshed with Lagrangian elements and treated as a rigid body and was placed at the center of the two SPH foam blocks (Figure 4.4). The implant was prescribed an axial linear ramp load up to 4 kN. To mimic the experimental center of rotation of the cage, a point located at the centroid of the bottom surface of the implant was created, which was restricted from translating in the uncontrolled axes. The implant was free to rotate about all axes. The cage's center of mass was restricted from translating along the plane normal to the load direction, keeping the implant from sliding across the surface of the PU foam. On account of a wide range of reported static friction coefficients for the interaction of PU foam and metals [167], [168], a static friction coefficient of 0.15 was applied for the PU foam-indenter contact definition, following the coefficient selected for the bone-indenter contact definition in Chapter 3.

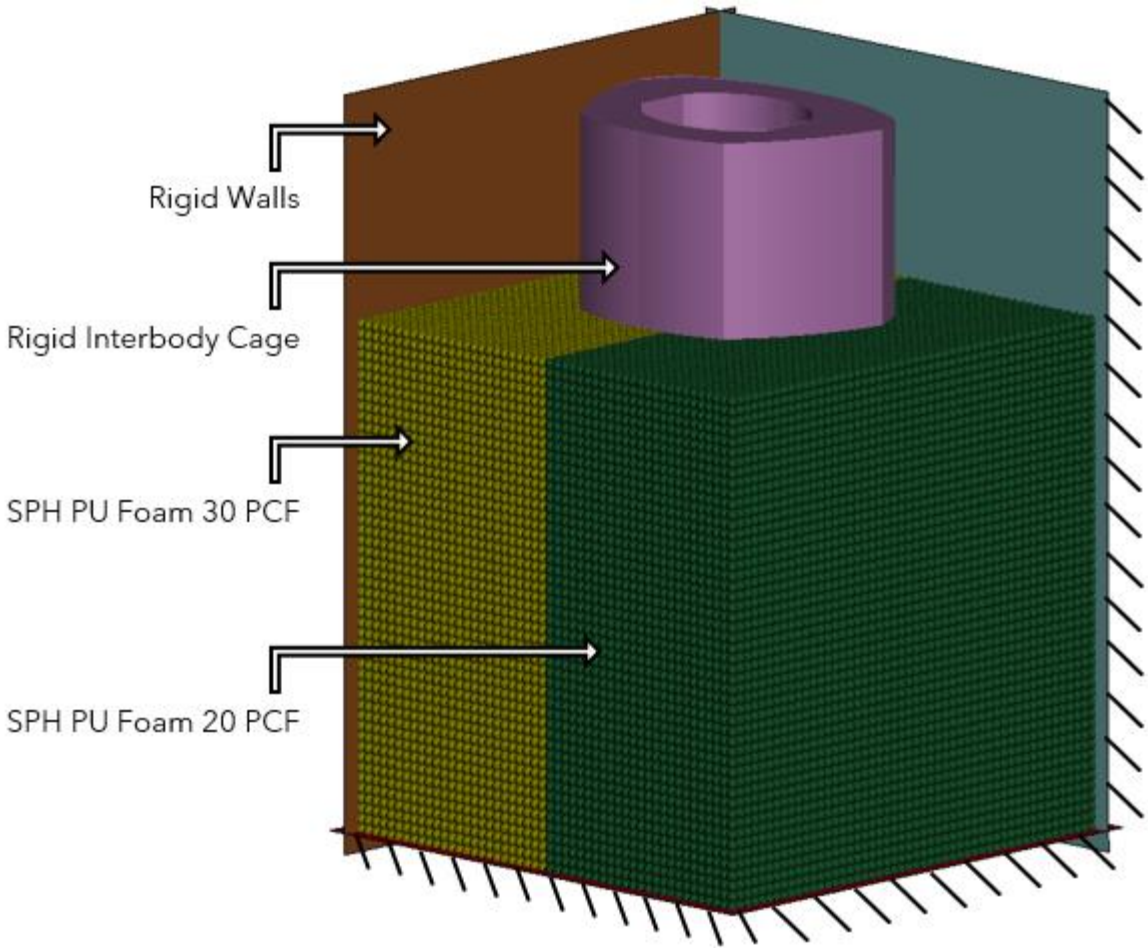

Figure 4.4 Model setup including the implant placed at the center of the top surface of the SPH foam model

4.3.3 Analysis

Single element material fitting was assessed using a root mean square error algorithm (MATLAB R2023b, The Math-Works, Inc., Massachusetts, USA). The displacement-force results representing the axial and rotational subsidence results for the implant were compared to this study's experimental data using the FC setup. Further, qualitative assessments of bone crushing and densification were done by comparing the plastic strain fields beneath the implant in the model to the CT scan image of the experiment.

4.4 Results

4.4.1 Experimental

Axial and rotational subsidence versus force results for each of the tested fixturing setups were plotted for comparison (Figure 4.5 & Figure 4.6). The implant subsided axially approximately twice as much in the tests that used the FC setup versus those that employed the BSJ setup. Unconstrained axial compression up to 4 kN yielded, on average up to 2.51 mm (SD = 0.38) and 4.68 mm (SD = 0.57) of axial subsidence for the BSJ and FC setups, respectively. Minimal rotational subsidence occurred when using the BSJ setup, with an average of 2.77° (SD = 0.50) up to a maximum of 3.49°. In contrast, significant unconstrained rotation into the less dense foam (20 PCF) was observed when using the FC setup, with an average of 17.97° (SD = 0.89) up to a maximum of 19.27°.

Using the FC setup, the implant experienced a steep increase in rotational subsidence into the weaker PU foam specimen around 1.4 kN of applied force. This coincides with an increase in axial subsidence using the FC setup. Additionally, at approximately 3.25 kN of unconstrained axial compression using the FC setup, the implant began to rotate in the opposite direction, towards the denser foam (30 PCF) until the conclusion of the test. This behaviour was not observed with the BSJ setup, nor did it significantly influence the axial subsidence results.

Through all the FC tests, the axes that were programmed to hold no load during the tests did not exhibit any loads much greater than the error bounds published by the manufacturer: 1.4 N in forces in-plane with the top surface of the foam-implant system, 0.05 N.m in axial moment, and 0.2 N.m in moments about the remaining two axes, controlled by the arms of the machine.

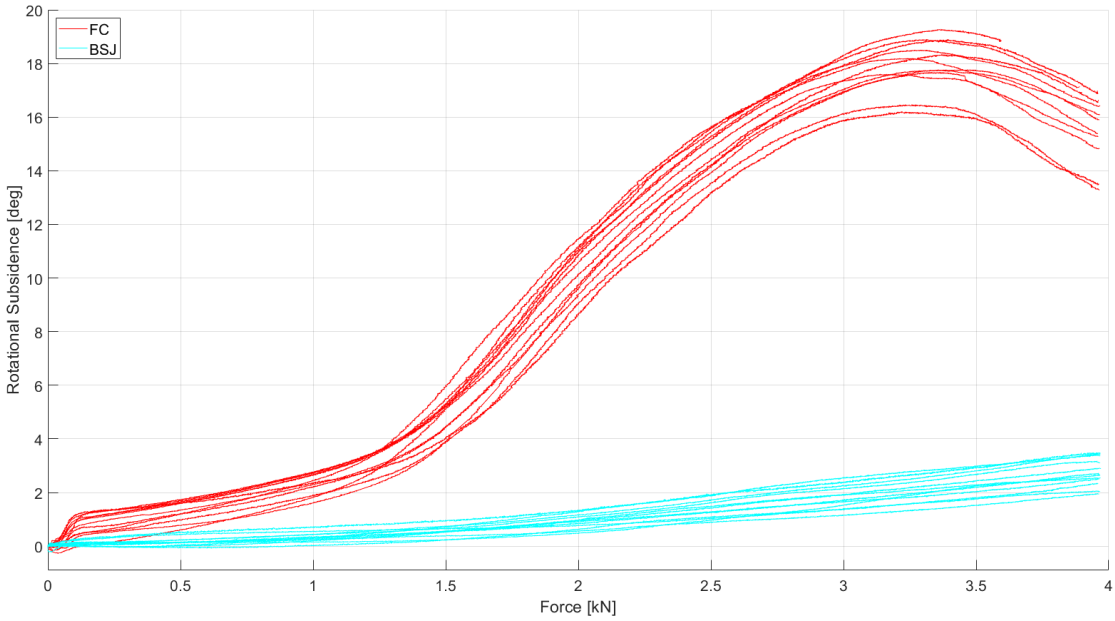

Figure 4.5 Rotational Subsidence – Force results using the FC and BSJ test setups

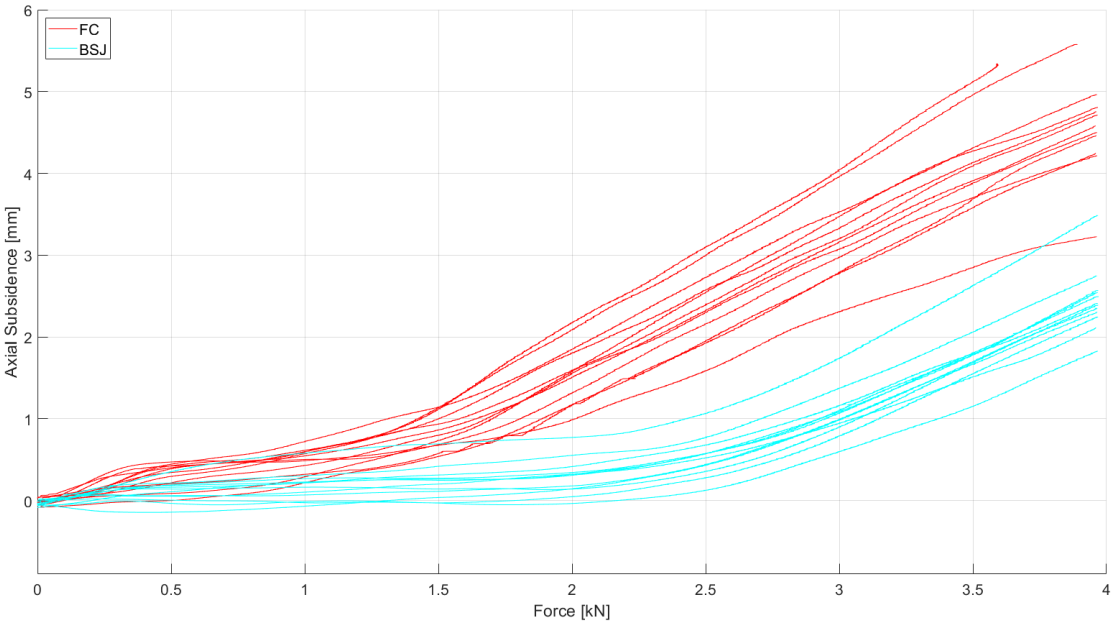

Figure 4.6 Axial Subsidence – Force results using the FC and BSJ test setups

There was limited difference between the results from each side of the PU foam-steel tubing samples. Since each side of these samples were tested sequentially, the potential for the crushed foam material on one side sample influencing the results of the other side was investigated. Following a one-tailed student t-test, no statistical significance was found

between the rotational subsidence results of each side for either of the test setups. P-values of 0.4098 and 0.2831 were calculated for the difference in rotational subsidence results from each side of the samples for the FC and BSJ setups respectively.

Photographs displaying the final deformed state of the foam-implant system were taken as comparison (Figure 4.7). There is a significant observable difference in total implant rotation into the weaker PU foam specimen, which contributed to a larger increase in total axial subsidence into both foams.

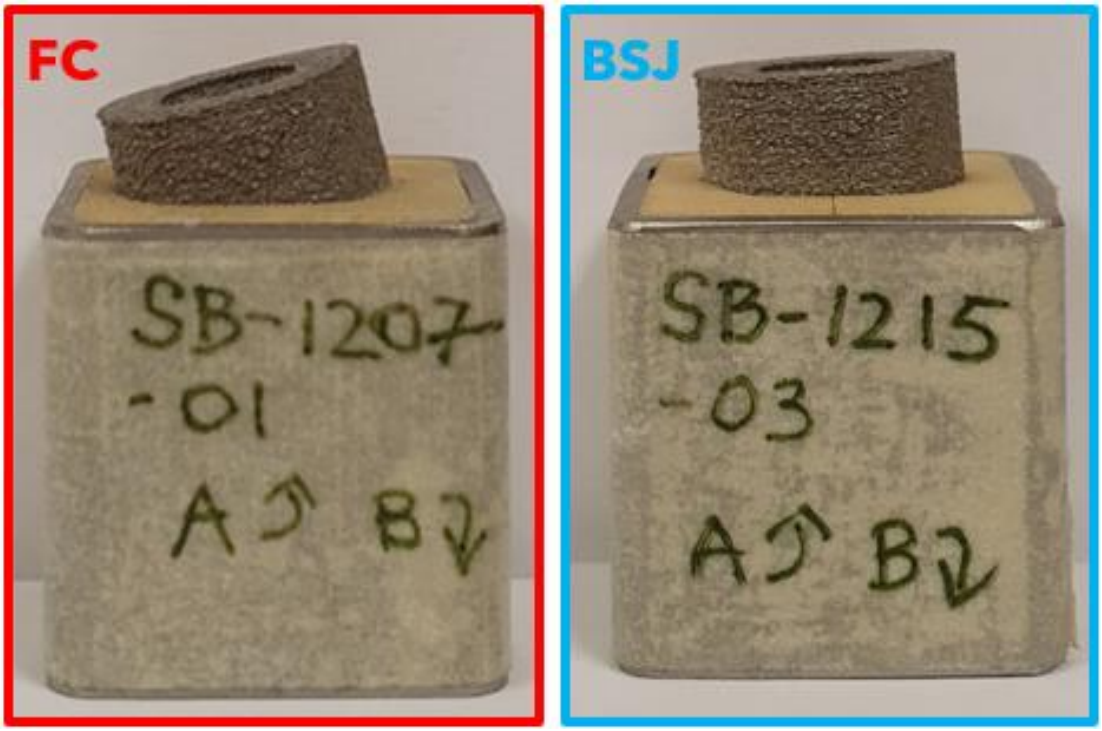

Figure 4.7 Experimental photographs representing the final deformed state of foam-implant systems using the Force-Control (left, red) and the ASTM-based Ball-Socket Joint test setup (right, blue)

CT images of the final deformed state of the sandwiched PU foam samples for the FC and BSJ tests revealed the densification pattern exhibited in the PU foam (Figure 4.8). Densification of the foam occurred predominantly directly beneath the implant and mostly in

the weaker PU foam specimen where most implant rotation occurred. PU foam material also sheared off near the implant and near the densified region in the weaker PU foam sample. Less local densification of the weaker PU foam happened with the BSJ setup due to less total implant rotation. With the FC setup, at the conclusion of the test, the region with densified material in the 20 PCF foam is thicker than observed in the BSJ setup sample.

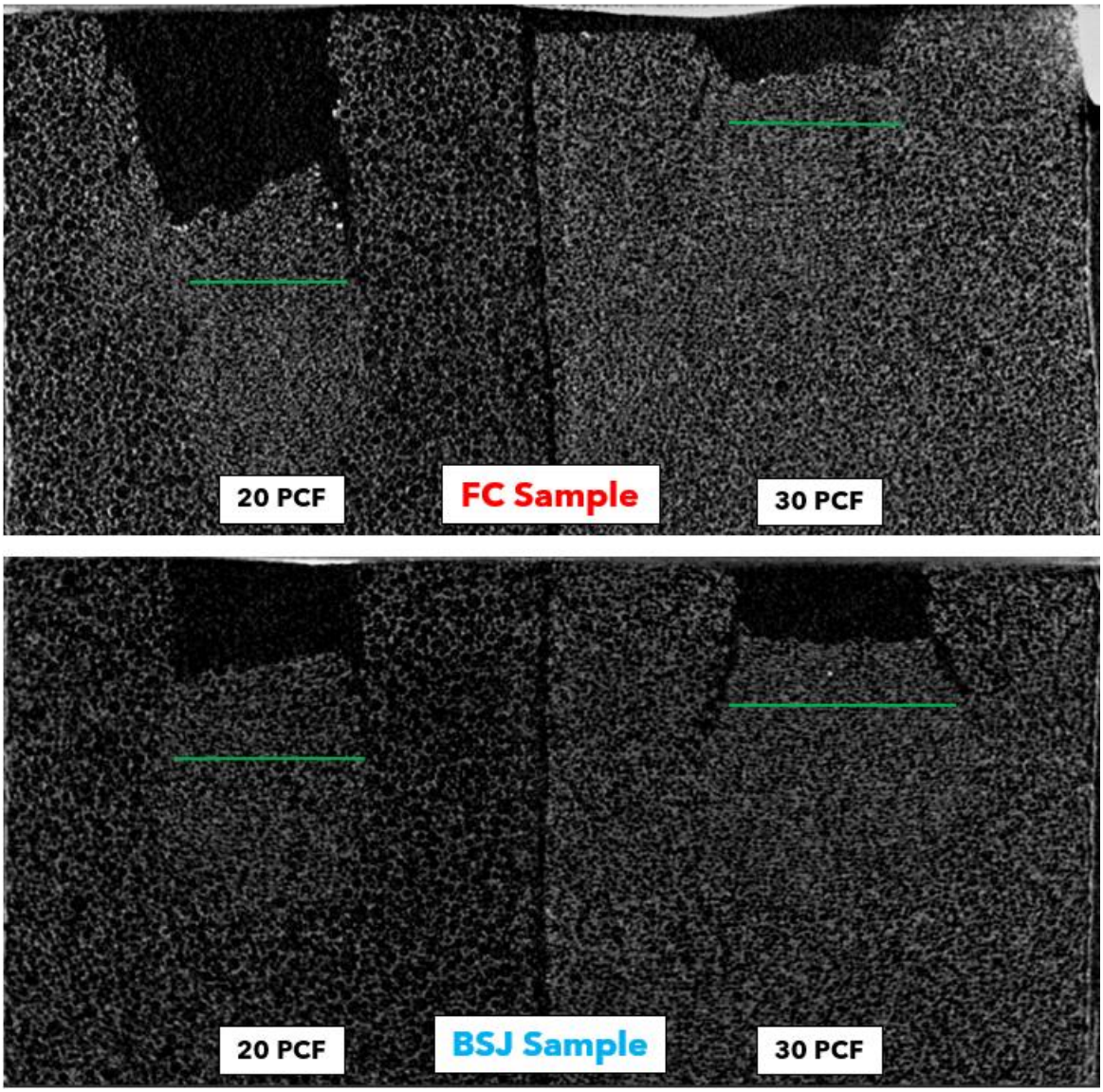

Figure 4.8 CT images representing the final deformed state of foam-implant systems using the Force-Control (top) and the ASTM-based Ball-Socket Joint test setup (bottom); green lines denote the slice at which greyscale CT intensity measurements were taken

Relative density measurements from grey-scale values based on voxel intensity in the CT scan of the PU foam specimens were taken (Table 4.5). In the sample from the FC experiments, the region of PU foam near the implant on the side with more implant rotation had a 32.1% increase in density while the other side at had a 5.5% increase at the conclusion of the experiment. The localized density of the 20 PCF foam by the implant became very similar to the measured density of the undeformed 30 PCF foam. In contrast, in the BSJ sample scanned with CT, the density of the 20 and 30 PCF foams increased by 13.6% and 13.7% respectively.

Table 4.5 CT Image Greyscale Intensity Measurement in the 20 and 30 PCF foams at the conclusion of each of the FC and BSJ tests

	FC Sample		**BSJ Sample**	
Foam Specimen (PCF)	20	30	20	30
Greyscale CT Intensity Measurement In Undeformed Region	3060.3	4146.9	5419.3	6941.9
Greyscale CT Intensity Measurement In the Densified Region	4073.3	4781.2	6626.9	7981.0
Percent Difference (%)	133.1	115.3	122.3	115.0

4.4.2 Computational

Single Element Material Fitting

Single element uniaxial compression tests were conducted with each PU foam sample from the datasets from Issa et al. (2023) [28] and Schulze et al. (2018) [29] (Figure 4.9). In general, the stress-strain curves reported by each source had very similar behaviour in the 30% strain, particularly in the PCF 20 foam but Issa et al. (2023) [28] reported an earlier onset of the material densification, based on the stress-strain response, for both foam densities. Up to

approximately 30% strain, the difference in stress-strain response between the weaker and stiffer samples of PU foam is greater in the dataset from Schulze et al. (2018) [29].

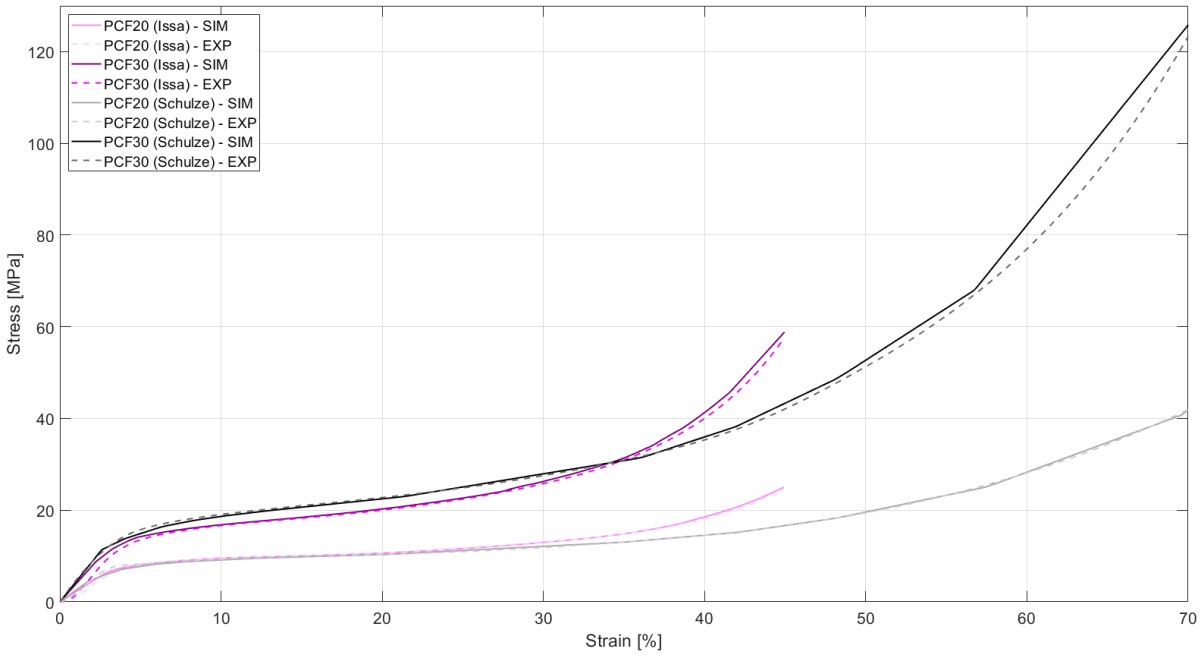

Figure 4.9 Experimental and single element fit uniaxial stress strain curves for the 20 and 30 PCF foam samples, based on datasets from Issa et al. (2023) [28] (pink, purple) and Schulze et al. (2018) [29] (grey, black)

The coefficient of determination (R^2) was calculated for each simulation-experiment pair (Table 4.6). By modifying the input elastic modulus and the sampling points of the plastic region of the uniaxial stress-strain curve, it was possible to achieve an effective fit of the material model with respect to the experimental data, with all fits having a coefficient of determination greater than or equal to 0.99998.

Table 4.6 Coefficients of Determination for each model fitting with respect to the experimental data

Exp-Sim Pair Density	Coefficient of Determination (R^2)
Issa – 20 PCF	0.99998
Issa – 30 PCF	0.99998
Schulze – 20 PCF	1
Schulze – 30 PCF	0.99999

Convergence Analysis

A convergence analysis was performed (Figure 4.10 & Figure 4.11) assessing the maximum axial and rotational subsidence using the PU-Issa model. According to the maximum rotational subsidence across the different SPH element distribution densities, the SPH model appeared to have converged with 125,000 SPH elements, but measuring the axial subsidence revealed that convergence did not occur until 262,144 SPH elements were used in the model. The main outcomes of the work in this study are axial and rotational displacement-force response curves and their comparison to experimental data. The test prescribed a linear force control rate and so the maximum axial and rotational displacements or 'subsidence' during the test was used as the measure of interest in the convergence analysis.

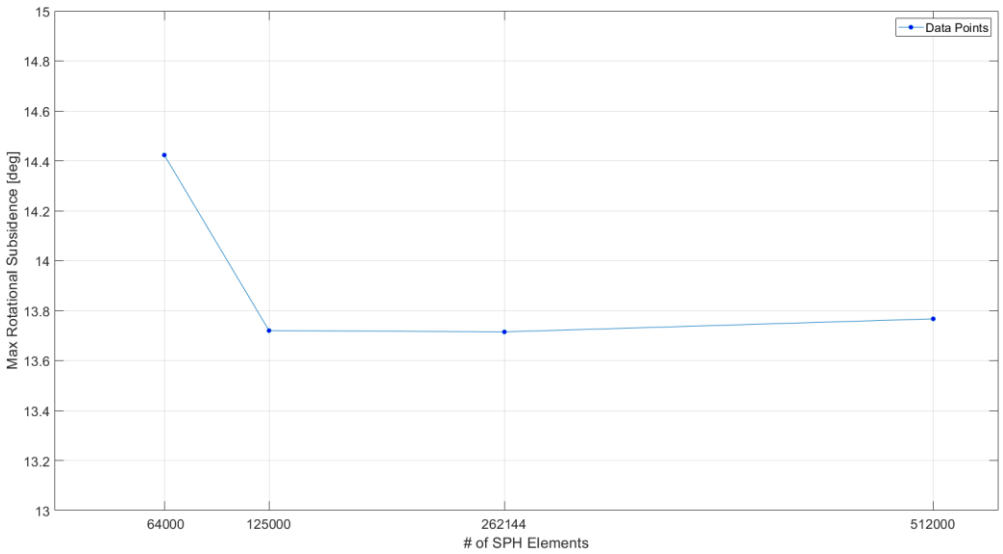

Figure 4.10 Convergence results comparing max rotational subsidence across different SPH element distribution densities

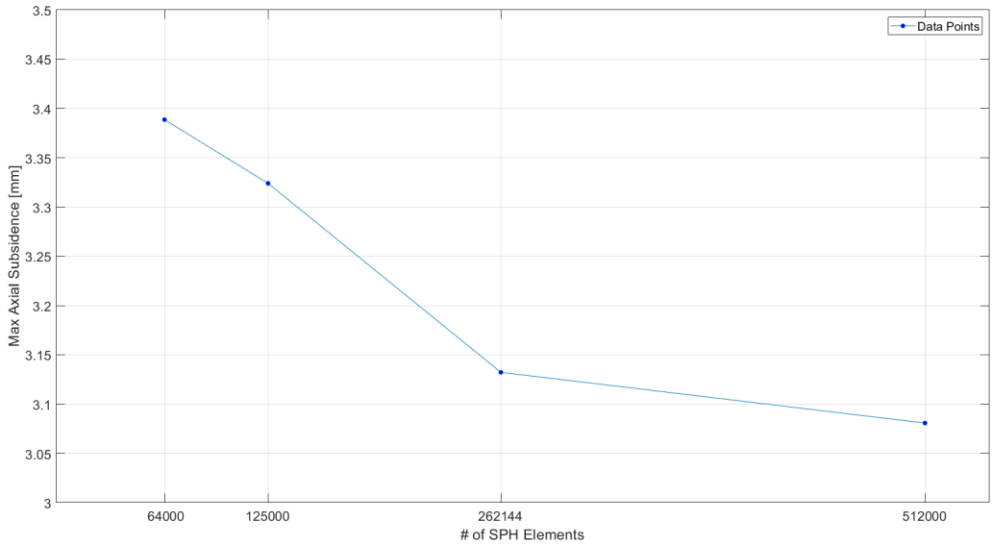

Figure 4.11 Convergence results comparing max axial subsidence across different SPH element distribution densities

Quantitative Results

The computational model was able to accurately represent the crushing and indentation behaviour that was observed experimentally. Using the two datasets to build two pairs of material models for the sandwiched PU foams in this loading mode, the model was not able to

fully envelop the rotational subsidence experimental data (Figure 4.12). The numerical rotational subsidence results matched the final values at 4 kN of unconstrained compression, but the shape of the curves did not match the experimental results well. The increase in rotation observed with the FC setup experimentally at 1.4 kN was not reproduced in the simulations. The amount of rotation was mainly influenced by the difference in mechanical properties between the weaker and stiffer PU foam samples within the same model and input dataset. Since there was a greater observed difference in the experimental stress-strain response reported by Schulze et al. (2018) [29], there was more rotation of the implant in its FE simulation. In pilot FE simulations for this study, different implant geometries and slightly modified input sampling points defining the hardening curve of the CF material formulation were investigated. In those pilot simulations, the inflection points observed experimentally in the rotational subsidence of the implant using the FC test setup around 1.4 kN and 3.25 kN of unconstrained compressive loading was reproducible. However, in the present model, that phenomenon was not reproduced.

The axial subsidence results from the simulations matched the experimental data using the FC test setup up to around 1.6 kN (Figure 4.13). In the experimental data, a change in slope of the axial subsidence using the FC setup occurred at that point, coinciding with a sudden increase in rotational subsidence (Figure 4.12). This increased rotation was not captured in the FE model via the material models used in this study. As a result, the numerical axial subsidence results deviated from the experimental FC results. In general, the prediction of the FE model was closer to the FC experimental results for both axial and rotational subsidence than they are to the BSJ results.

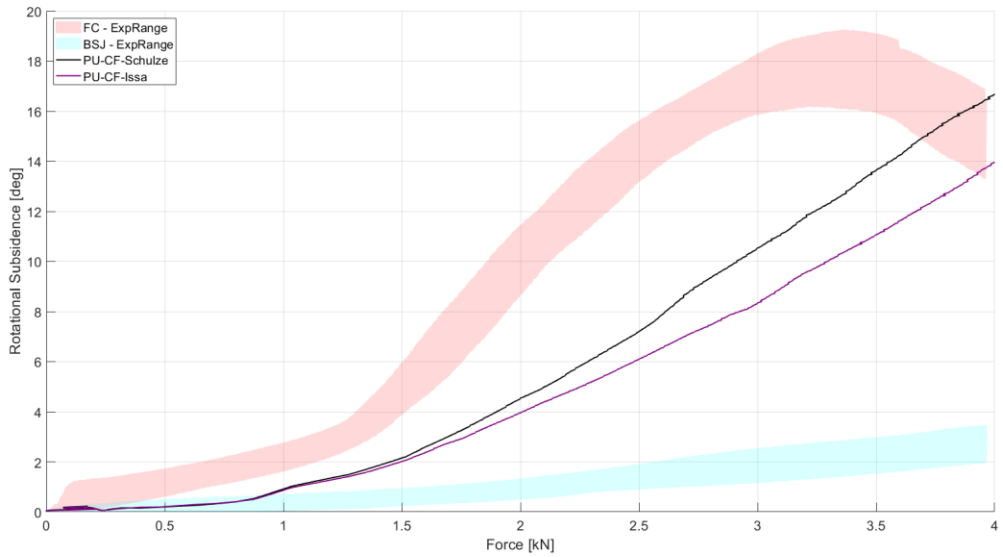

Figure 4.12 Rotational Subsidence – Force results from simulations of the models using material data from each studied dataset, and from the experimental results using the FC and BSJ setups

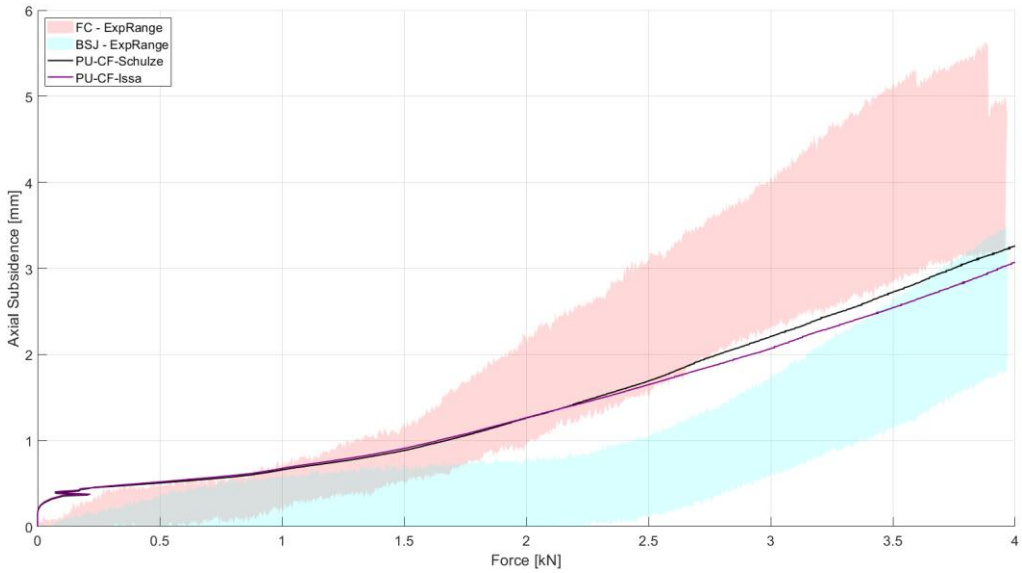

Figure 4.13 Axial Subsidence – Force results from simulations of the models using material data from each studied dataset, and from the experimental results using the FC and BSJ setups

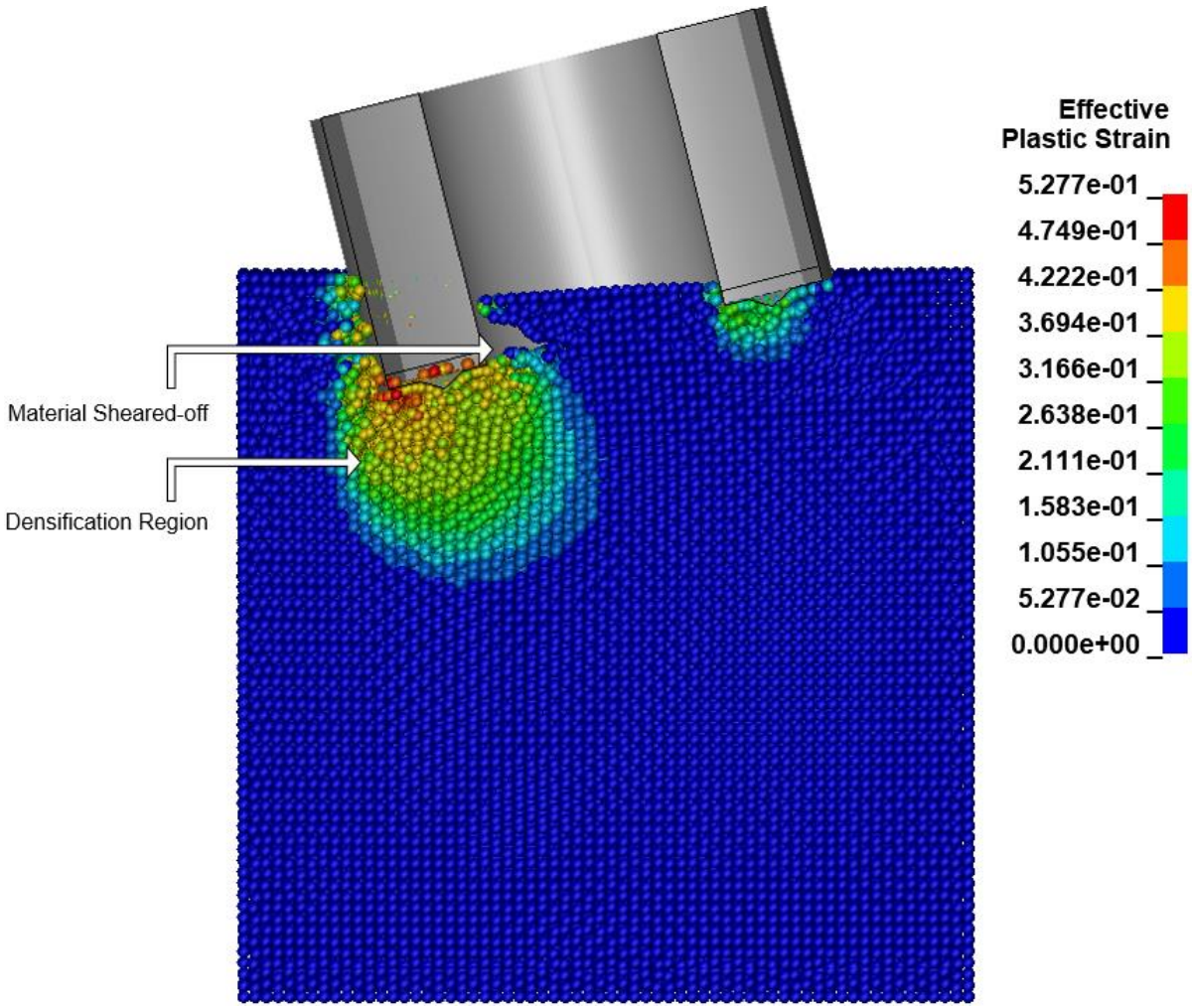

Figure 4.14 Cross-sectional view the plastic strain field of final deformed state of foam-implant system in FE simulation using the PU-Issa model

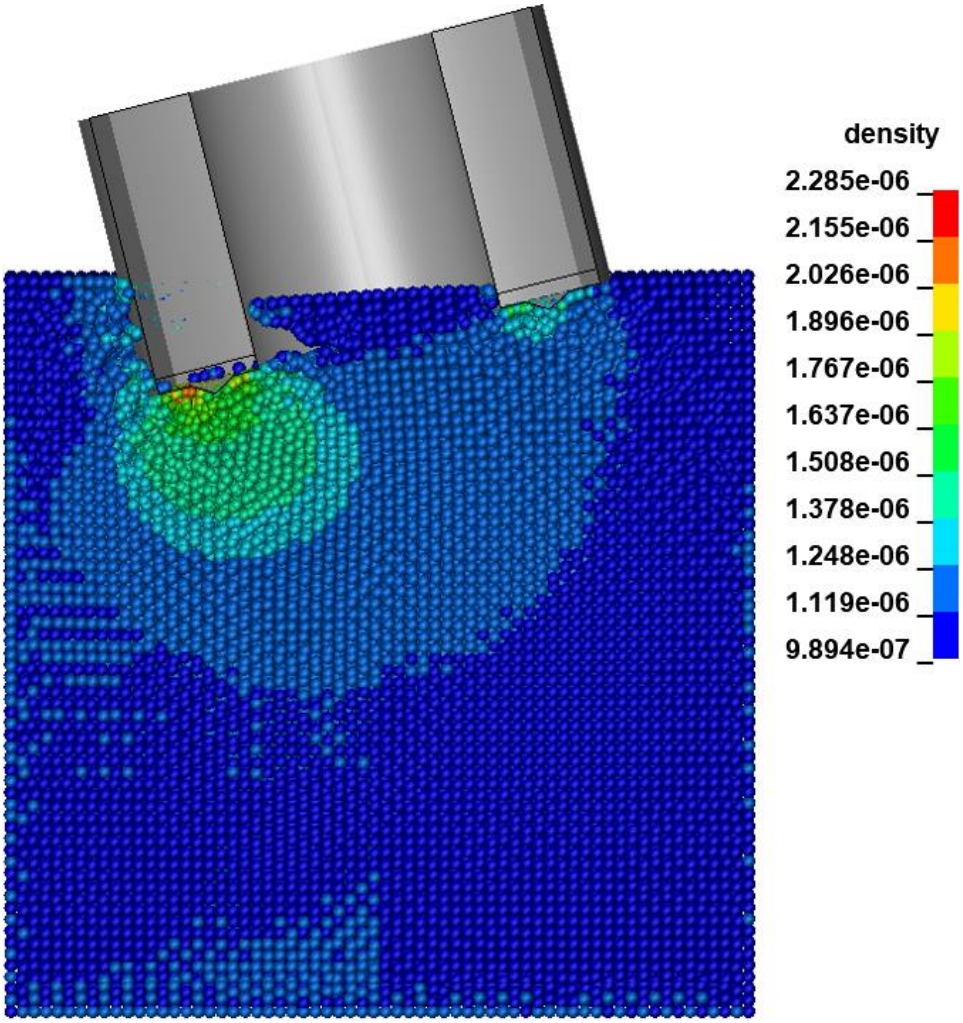

Figure 4.15 Cross-sectional view the SPH density field of final deformed state of foam-implant system in FE simulation using the PU-Issa model

Qualitative results from the FE simulations showed similar densification patterns as with the experimental CT images (Figure 4.14 & Figure 4.15): showing densification of the PU foam material beneath the implant, with a significantly larger region of densification on the weak PU side, and with material near the densified region of the weaker foam having sheared off.

4.5 Discussion

This study presented a novel method for performing unconstrained load-induced subsidence and compared it to the method from the existing ASTM F2267 test standard. Results taken from the novel setup were then also compared to FE simulation results.

4.5.1 Experimental

Overall, the FC setup provided more rotational freedom of movement compared to the BSJ setup. Increased rotational subsidence occurred, which in turn led to increased axial subsidence since the implant was effectively subsiding into a weaker material than with the BSJ setup. The BSJ setup did not provide full freedom of rotation about the foam-implant system’s center of rotation due to unwanted friction in the lubricated ball-socket joint.

Using the FC setup, the three stages of the typical stress strain curve for PU foam can be seen in the implants’ rotational subsidence curves: (1) a linear elastic region with minimal displacement relative to the increase in force, followed by (2) a plateau region where the modulus curve is much lower and thus the rotation of the implant is increased for an extended period of time, and finalized by (3) a densification region. As noticed in the CT images of the deformed PU foam specimens, significant rotational subsidence occurred with the FC setup leading to a large region of densified PU foam. The 20 PCF foam densified to a level at which the local stiffness of the 20 PCF foam was greater to or equal to the stiffness of the 30 PCF foam. As a result, at this point the implant began to rotate in the opposite direction about the same axis, leveling out its orientation before the conclusion of the experiment. This behaviour was not observed with the BSJ tests since in those tests, rotation was very limited and thus the 20 PCF foam beneath the implant did not reach the same levels of localized stress and strain.

Therefore, the 20 PCF foam did not densify enough beneath the implant to incur implant rotation in the opposite direction towards the 30 PCF material.

The overall axial implant subsidence using the FC setup was also seen to deviate from the results when using the BSJ setup. Coinciding with the 'plateau' region described previously where the implant experienced a steep uptick in rotation around 1.4 kN of applied force, there was a marked increase in overall axial subsidence of the implant into both foam specimens.

The failure behaviour of the PU foams was very similar between the two different test setups as evidenced by the CT images showing similar behaviour. The PU foam material of each density both were crushed and began to densify nearest the bottom surface of the implant with minimal densification occurring on the sides of implant. In fact, the material appeared to shear off as the implant continued to indent the PU foam material beneath it due to shear bands that occur during the compression failure of PU foam. Additionally, densification patterns were similar to those observed experimentally in human trabecular bone [26], [81] where the thickness of the densification region increases with indentation depth and is located directly beneath the indenting object.

Differences in the subsidence versus the force response were observed between the FC and BSJ setups, both axially and rotationally. Particularly, it was observed that with equal compressive loading, the tests using the FC setup exhibited 1.86 times more axial subsidence than when using the BSJ setup, highlighting the influence implant rotation can have on overall implant subsidence, both in this experiment and in pre-clinical situations. Rotationally, the FC setup produced rotational subsidence magnitudes 6.48 times greater than with the standardized test method. Furthermore, as evidenced by the machine's ability to reliably hold no load in and about all axes excluding the compressively loaded axis, the novel setup promotes full implant

freedom of rotation towards the less stiff PU foam. In contrast, while appropriately lubricated, the loaded ball-socket joint still presented non-trivial levels of friction that would restrict rotation about the in-plane axes.

These findings provide concrete evidence on the effectiveness of the newly proposed test method and the ineffectiveness of the previously employed methodology as it was shown to restrict rotational subsidence and subsequently skewed the magnitude of axial subsidence. With rotational subsidence known to occur clinically with interbody cage implants, these results highlight potential limitations of the current standard for testing cage subsidence.

4.5.2 Computational

The computational results supported the claim that the novel testing setup presented clear advantages compared to the standardized test method: the amount of implant subsidence that was observed was much closer to the FC tests’ results, both axially and rotationally. Furthermore, as evidenced by the cross-sectional images of the simulation at the end of the test and the CT images of the deformed PU foam samples, the model was able to effectively represent the crushing and densification behaviour observed in the PU foams after indentation. The simulated and experimental PU foam materials both densified primarily nearest the bottom surface of the implant with limited densification occurring elsewhere.

However, exact recreation of the failure response of the PU foams was not achieved. Using the material models developed based on work by Issa et al. (2023) [28] and Schulze et al. (2018) [29], the FE models were able to envelop the experimental axial subsidence test data. Rotational subsidence in the simulations also underestimated the FC experimental results; however, this measure is mainly influenced by the difference in mechanical properties between the 20 PCF and 30 PCF samples of foam within the same model. Additional testing showed

that calibration of different sandwiched foam pairs close to the originally input datasets could produce similar rotational subsidence results as the experimental tests. Furthermore, identification of the dimensionless parameters used as input for each model were based on those computed by Issa et al. (2023) [28]. In their work, FE simulations using these dimensionless parameters overestimated the stiffness of the PU foams relative to their experimental results. During the current study’s single element fitting procedure, only the elastic modulus and the sampling points in the plastic region of the experimental uniaxial stress-strain curve were modified to fit the desired response and the dimensionless parameters reported by Issa et al. (2023) [28] were maintained in each material model. These parameters are believed to have added unwanted error to the prediction of behaviour for these materials.

With respect to rotational subsidence results for the FC setup, the last of the three stages that describe the subsidence-force curves, densification of the 20 PCF material, was not present in the model output results. Pilot FE simulations with different implant geometries and material behaviour proved that this behaviour was achievable with the SPH-CF model setup, but it was not achieved in the model results reported in this study. With alterations to the third stage of the uniaxial compression stress strain curves used as input for the material definition, the densification behaviour of the PU foam exhibited *in vitro* would be able to be reproduced numerically. To add, as was noticed in Chapter 3, the CF model is less effective at modeling loading modes aside from uniaxial or hydrostatic compression. As a result, the present model is less effective at modeling shear loading and other complex stress states that are experienced in this test with rotational subsidence. It is believed that this quality of the model could contribute to some of the reported inaccuracy of the results.

4.5.3 Limitations and Future Work

While the experimental tests produced effective results demonstrating the improved performance of the newly proposed test method for conducting unconstrained compression of interbody cage implants into PU foam, compared to the test setup based on ASTM-F2267, the amount of rotational subsidence with this test protocol observed with cadaveric specimens is yet unknown. Further testing using this new method should include unconstrained compression of interbody cage implants on vertebral cadavers to further elucidate the clinical relevance of unconstrained loading modes for the accurate *in vitro* simulation of implant subsidence. A final limitation was inaccuracy in exactly reproducing the test fixture described in ASTM-F2267 for the BSJ test setup. The indenter 'pushrod' is set at a minimum of 38 cm in the standard but the one created for the BSJ setup measured 12.7 cm, due to test-space-related constraints.

With respect to the computational model, the model was limited in its ability to accurately match the exact magnitudes of rotational subsidence, particularly at higher force values. Lacking experimental studies that could be used to build a material model specific to the PU foam samples that were included in the test, and due to a wide range of reported mechanical properties for these foams, accurate prediction of axial and rotational subsidence is difficult. Further, while the CF-Schulze model produced effective results for lower force values and overestimated the response at higher forces, it is unclear if this inaccuracy is based in the material model or in other components of the FE model. Finally, convergence could not be fully achieved in this study due to constraints relating to computational cost of the simulation. Although the study's main conclusions and reported material behaviours are not anticipated to change significantly with a finer SPH element distribution, some error in the

final results can be attributed to the SPH element distribution density over-stiffening the system.

Suggested future work would include conducting experimental tests used for material characterization of these tested PU foams for the development of a material model that is independent of data from other sources in the literature. To add, investigation into alternate material models that can address the concerns raised by the material models reduced effectiveness at modeling non-compressive loading modes would improve its ability to predict axial and rotational subsidence.

4.6 Conclusion

Unconstrained load-induced subsidence has not been previously explored despite the clinical relevance of this loading mode. The present work demonstrates the improved performance of the novel FC technique for conducting unconstrained load-induced subsidence. Increased rotational subsidence was observed with the FC setup versus the BSJ setup, highlighting friction-based constraints preventing free rotation in the BSJ method. The numerical model developed in this study further supported the claim proposed from the experiments. This novel method for performing unconstrained loading offers potential improvement for implant subsidence testing relative to devices conforming to ASTM F2267. Improved modeling efforts, driven by the noted influence implant rotation has on total subsidence will advance the prediction of implant subsidence pre-clinically. Furthermore, the computational model developed in Chapter 3 and calibrated to different datasets for PU foam in this study was able to accurately represent the crushing and densification phenomena observed experimentally in the damaged PU foam samples. The model was further capable of producing effective displacement-force responses for this unconstrained loading mode, for both rotational and translational measures of subsidence.

Chapter 5
Conclusions and Recommendations

5.1 Significance

The presented computational work in this thesis demonstrated the potential use of simplified FE models of trabecular bone based upon common clinical imaging metrics like BMD and bone volume percentages towards pre-clinical prediction of trabecular bone damage. Despite limited research employing the SPH method in orthopaedic biomechanics, this numerical technique has significant potential in solid mechanics modeling efforts. This method provided effective results in the representation of trabecular bone crushing and densification behaviour without the need for elaborate meshing algorithms or other damage modeling methods that are less effective at modeling macro-level simulations such as 3D implant subsidence. The investigated CF material model, boasting pressure-dependent yielding, should be employed in the future to more accurately capture the post-yield response of trabecular bone, particularly in high-strain simulations modeling confined experiments. The developed models and investigated computational methods offer a strong step towards the development of accurate and simplified FE modeling for representing bone crushing and densification. These improvements in computational modeling of spinal surgery could lead to pre-clinical advances with the potential for improved pre-operative prediction of implant subsidence and other similar implant failure in patients.

The study described in Chapter 4 provided a new method for testing and evaluating implant performance in implant subsidence testing. ASTM F2267 is at present the only standardized test method for assessing an implant's resistance to subsidence. However, it and

other tests aiming to quantify interbody cage implant performance neglect consideration for the clinically relevant unconstrained loading mode proposed in this study. The test method, utilizing two densities of PU foam, and leveraging the capabilities of a six-axis load-cell allows for a simplified means of evaluating an implant's resistance to rotational subsidence. The results from this work further cemented the relevance of unconstrained loading modes for in-vitro implant subsidence tests.

The insights acquired from this study can guide the refinement of experimental and numerical implant subsidence testing to work towards improved ability to pre-clinically predict implant subsidence.

5.2 Future Work

Future endeavors should address the limitations observed in the presented work. The first is performing independent, in-house material characterization experiments on vertebral trabecular bone. This would allow for better material model calibration, with model result comparisons being made on a greater sample size of data and on data that the model was built from rather than building a material from one dataset and comparing the results to a different dataset that may have material with different mechanical properties. Conducting material characterization tests would also allow for investigation into a wider variety of possible material models, both for trabecular bone and for the inter-trabecular constituents such as marrow. Investigation of other material models to improve the model's prediction in simulations including complex loading modes like that seen in rotational implant subsidence, incorporating consideration for compression and shear loading in the material model input, may improve subsidence prediction. *In vitro* testing including and excluding marrow could help elucidate its influence on the crushing and densification response in indentation tests,

leading to the development of new appropriate material models that consider more than just an elastic definition. Similar tests can also be carried out for the material characterization of PU foam having recognized a large variation in reported mechanical properties for these materials in the literature. Finally, additional testing centered around this newly proposed FC test setup would help concretize the validity of this load case for the assessment of implant subsidence risk, axially and rotationally. The amount of rotational subsidence from unconstrained compression of an interbody cage implant into a cadaveric specimen is yet unknown. Performing unconstrained load-induced subsidence onto cadaveric specimens would highlight the clinical relevance of this loading mode for the accurate *in vitro* simulation of implant subsidence.

Letters of Copyright Permission

SPRINGER NATURE LICENSE
TERMS AND CONDITIONS
Mar 20, 2024

This Agreement between University of Waterloo -- Remy Benais ("You") and Springer Nature ("Springer Nature") consists of your license details and the terms and conditions provided by Springer Nature and Copyright Clearance Center.

License Number	5752890695320
License date	Mar 20, 2024
Licensed Content Publisher	Springer Nature
Licensed Content Publication	Zeitschrift für Rheumatologie
Licensed Content Title	Age-related changes in bone mass, structure, and strength – effects of loading
Licensed Content Author	Lis Mosekilde
Licensed Content Date	Apr 10, 2014
Type of Use	Thesis/Dissertation
Requestor type	academic/university or research institute
Format	electronic
Portion	figures/tables/illustrations
Number of figures/tables/illustrations	1
Will you be translating?	no
Circulation/distribution	1 - 29
Author of this Springer Nature content	no
Title of new work	Computational modeling of trabecular bone indentation and development of a new test method to perform unconstrained load-induced subsidence of an intervertebral body fusion device
Institution name	University of Waterloo
Expected presentation date	Apr 2024
Portions	Fig. 1 a) Vertebral body from a young individual. The central trabecular network is dense, with a ªperfectº architecture (normal photograph)

Requestor Location	University of Waterloo 181 Sherwood Avenue Toronto, ON M4P2A9 Canada Attn: University of Waterloo
Total	0.00 CAD

SPRINGER NATURE LICENSE
TERMS AND CONDITIONS

Mar 18, 2024

This Agreement between University of Waterloo -- Remy Benais ("You") and Springer Nature ("Springer Nature") consists of your license details and the terms and conditions provided by Springer Nature and Copyright Clearance Center.

License Number	5751991021123
License date	Mar 18, 2024
Licensed Content Publisher	Springer Nature
Licensed Content Publication	The International Journal of Advanced Manufacturing Technology
Licensed Content Title	Numerical analysis of vibration effect on friction stir welding by smoothed particle hydrodynamics (SPH)
Licensed Content Author	Behrouz Bagheri et al
Licensed Content Date	Aug 11, 2020
Type of Use	Thesis/Dissertation
Requestor type	academic/university or research institute
Format	electronic
Portion	figures/tables/illustrations
Number of figures/tables/illustrations	1
Will you be translating?	no
Circulation/distribution	1 - 29
Author of this Springer Nature content	no
Title of new work	Computational modeling of trabecular bone indentation and development of a new test method to perform unconstrained load-induced subsidence of an intervertebral body fusion device

Institution name	University of Waterloo
Expected presentation date	Apr 2024
Portions	Fig.2: Interpolation during SPH method
Requestor Location	University of Waterloo 181 Sherwood Avenue Toronto, ON M4P2A9 Canada Attn: University of Waterloo
Total	0.00 CAD

SPRINGER NATURE LICENSE
TERMS AND CONDITIONS
Mar 18, 2024

This Agreement between University of Waterloo -- Remy Benais ("You") and Springer Nature ("Springer Nature") consists of your license details and the terms and conditions provided by Springer Nature and Copyright Clearance Center.

License Number	5751990448364
License date	Mar 18, 2024
Licensed Content Publisher	Springer Nature
Licensed Content Publication	Neurosurgical Review
Licensed Content Title	A minimum 2-year comparative study of autologous cancellous bone grafting versus beta-tricalcium phosphate in anterior cervical discectomy and fusion using a rectangular titanium stand-alone cage
Licensed Content Author	Toru Yamagata et al
Licensed Content Date	Apr 21, 2016
Type of Use	Thesis/Dissertation
Requestor type	academic/university or research institute
Format	electronic
Portion	figures/tables/illustrations
Number of figures/tables/illustrations	1
Will you be translating?	no
Circulation/distribution	1 - 29

Author of this Springer Nature content	no
Title of new work	Computational modeling of trabecular bone indentation and development of a new test method to perform unconstrained load-induced subsidence of an intervertebral body fusion device
Institution name	University of Waterloo
Expected presentation date	Apr 2024
Portions	Figure 1: The four grades of cage subsidence with representative plain lateral radiographs. a Grade 0, no subsidence. b Grade 1, less than one-third subsidence. c Grade 2, less than two-third subsidence. d Grade 3, more than two-third subsidence
Requestor Location	University of Waterloo 181 Sherwood Avenue Toronto, ON M4P2A9 Canada Attn: University of Waterloo
Billing Type	Invoice
Billing Address	University of Waterloo 181 Sherwood Avenue Toronto, ON M4P2A9 Canada Attn: University of Waterloo
Total	0.00 CAD

JOHN WILEY AND SONS LICENSE
TERMS AND CONDITIONS
Mar 18, 2024

This Agreement between University of Waterloo -- Remy Benais ("You") and John Wiley and Sons ("John Wiley and Sons") consists of your license details and the terms and conditions provided by John Wiley and Sons and Copyright Clearance Center.

License Number	5751991021123
License date	Mar 18, 2024
Licensed Content Publisher	Springer Nature

Licensed Content Publication	The International Journal of Advanced Manufacturing Technology
Licensed Content Title	Numerical analysis of vibration effect on friction stir welding by smoothed particle hydrodynamics (SPH)
Licensed Content Author	Behrouz Bagheri et al
Licensed Content Date	Aug 11, 2020
Type of use	Thesis/Dissertation
Requestor type	academic/university or research institute
Format	electronic
Portion	figures/tables/illustrations
Will you be translating?	no
Circulation	1 - 29
Author of this ASM article	no
Title of new work	Computational modeling of trabecular bone indentation and development of a new test method to perform unconstrained load-induced subsidence of an intervertebral body fusion device
Institution name	University of Waterloo
Expected presentation date	Apr 2024
Portions	Fig.2: Interpolation during SPH method
Requestor Location	University of Waterloo 181 Sherwood Avenue Toronto, ON M4P2A9 Canada Attn: University of Waterloo
Total	0.00 CAD

JOHN WILEY AND SONS LICENSE
TERMS AND CONDITIONS

Mar 18, 2024

This Agreement between University of Waterloo -- Remy Benais ("You") and John Wiley and Sons ("John Wiley and Sons") consists of your license details and the terms and conditions provided by John Wiley and Sons and Copyright Clearance Center.

License Number	5751991164528
License date	Mar 18, 2024
Licensed Content Publisher	Springer Nature
Licensed Content Publication	The International Journal of Advanced Manufacturing Technology
Licensed Content Title	Numerical analysis of vibration effect on friction stir welding by smoothed particle hydrodynamics (SPH)
Licensed Content Author	Behrouz Bagheri et al
Licensed Content Date	Aug 11, 2020
Type of use	Thesis/Dissertation
Requestor type	academic/university or research institute
Format	electronic
Portion	figures/tables/illustrations
Will you be translating?	no
Circulation	1 - 29
Author of this ASM article	no
Title of new work	Computational modeling of trabecular bone indentation and development of a new test method to perform unconstrained load-induced subsidence of an intervertebral body fusion device
Institution name	University of Waterloo
Expected presentation date	Apr 2024
Portions	Fig.2: Interpolation during SPH method
Requestor Location	University of Waterloo 181 Sherwood Avenue Toronto, ON M4P2A9 Canada Attn: University of Waterloo
Total	0.00 CAD

References

[1] M. J. Reisener, M. Pumberger, J. Shue, F. P. Girardi, and A. P. Hughes, 'Trends in lumbar spinal fusion—a literature review', *Journal of Spine Surgery*, vol. 6, no. 4, pp. 752–776, 2020.

[2] A. J. Buckland, K. Ashayeri, C. Leon, I. Cheng, J. A. Thomas, B. Braly, B. Kwon, and L. Eisen, 'Anterior column reconstruction of the lumbar spine in the lateral decubitus position: anatomical and patient-related considerations for ALIF, anterior-to-psoas, and transpsoas LLIF approaches', *European Spine Journal*, vol. 31, no. 9, pp. 2175–2187, Sep. 2022.

[3] S. de L. Schickert, J. J. J. P. van den Beucken, S. C. G. Leeuwenburgh, and J. A. Jansen, 'Pre-clinical evaluation of biological bone substitute materials for application in highly loaded skeletal sites', *Biomolecules*, vol. 10, no. 6, pp. 1–24, Jun. 2020.

[4] A. J. Pisano, D. R. Fredericks, T. Steelman, C. Riccio, M. D. Helgeson, and S. C. Wagner, 'Lumbar disc height and vertebral Hounsfield units: Association with interbody cage subsidence', *Neurosurg Focus*, vol. 49, no. 2, pp. 1–6, Aug. 2020.

[5] I. Noordhoek, M. T. Koning, W. C. H. Jacobs, and C. L. A. Vleggeert-Lankamp, 'Incidence and clinical relevance of cage subsidence in anterior cervical discectomy and fusion: a systematic review', *Acta Neurochir (Wien)*, vol. 160, no. 4, pp. 873–880, Apr. 2018.

[6] Y. C. Yao, P. H. Chou, H. H. Lin, S. T. Wang, C. L. Liu, and M. C. Chang, 'Risk Factors of Cage Subsidence in Patients Received Minimally Invasive Transforaminal Lumbar Interbody Fusion', *Spine (Phila Pa 1976)*, vol. 45, no. 19, pp. 1279–1285, Oct. 2020.

[7] T. V. Le, A. A. Baaj, E. Dakwar, C. J. Burkett, G. Murray, D. A. Smith, and J. S. Uribe, 'Subsidence of polyetheretherketone intervertebral cages in minimally invasive lateral retroperitoneal transpsoas lumbar interbody fusion.', *Spine (Phila Pa 1976)*, vol. 37, no. 14, pp. 1268–1273, 2012.

[8] G. M. Malham, R. M. Parker, C. M. Blecher, and K. A. Seex, ‘Assessment and classification of subsidence after lateral interbody fusion using serial computed tomography’, *J Neurosurg Spine*, vol. 23, no. 5, pp. 589–597, Nov. 2015.

[9] J. T. Wewel, C. Hartman, and J. S. Uribe, ‘Timing of Lateral Lumbar Interbody Subsidence: Review of Exclusive Intraoperative Subsidence’, *World Neurosurg*, vol. 137, pp. 208–212, May 2020.

[10] C. Rentenberger, I. Okano, S. N. Salzmann, F. Winter, N. Plais, M. D. Burkhard, J. Shue, A. A. Sama, F. P. Cammisa, F. P. Girardi, and A. P. Hughes, ‘Perioperative Risk Factors for Early Revisions in Stand-Alone Lateral Lumbar Interbody Fusion’, *World Neurosurg*, vol. 134, pp. 657–663, Feb. 2020.

[11] T. Yamagata, K. Naito, H. Arima, M. Yoshimura, K. Ohata, and T. Takami, ‘A minimum 2-year comparative study of autologous cancellous bone grafting versus beta-tricalcium phosphate in anterior cervical discectomy and fusion using a rectangular titanium stand-alone cage’, *Neurosurg Rev*, vol. 39, no. 3, pp. 475–482, Jul. 2016.

[12] P. Curtin, A. Conway, L. Martin, E. Lin, P. Jayakumar, and E. Swart, ‘Compilation and analysis of web-based orthopedic personalized predictive tools: A scoping review’, *J Pers Med*, vol. 10, no. 4, pp. 1–20, Nov. 2020.

[13] I. Okano, C. Jones, S. N. Salzmann, M. –J Reisener, O. C. Sax, C. Rentenberger, J. Shue, J. A. Carrino, A. A. Sama, F. P. Cammisa, F. P. Girardi, and A. P. Hughes, ‘Endplate volumetric bone mineral density measured by quantitative computed tomography as a novel predictive measure of severe cage subsidence after standalone lateral lumbar fusion’, *European Spine Journal*, vol. 29, no. 5, pp. 1131–1140, May 2020.

[14] A. Rohlmann, D. Pohl, A. Bender, F. Graichen, J. Dymke, H. Schmidt, and G. Bergmann, ‘Activities of everyday life with high spinal loads’, *PLoS One*, vol. 9, no. 5, pp. 1–9, May 2014.

[15] S. A. Goldstein, ‘The Mechanical Properties of Trabecular Bone: Dependence on Anatomic Location and Function’, *J Biomech*, vol. 20, no. 11, pp. 1055–1061, 1987.

[16] L. Rohl, E. Larsen, F. Linde, A. Odgaard, J. Jorgensen, and L. R. Biomechanics, ‘Tensile and Compressive Properties of Cancellous Bone’, *J Biomech*, vol. 24, no. 12, pp. 1143–1149, 1991.

[17] D. L. Kopperdahl and T. M. Keaveny, ‘Yield strain behavior of trabecular bone’, *J Biomech*, vol. 31, pp. 601–608, 1998.

[18] E. F. Morgan, O. C. Yeh, W. C. Chang, and T. M. Keaveny, ‘Nonlinear behavior of trabecular bone at small strains’, *J Biomech Eng*, vol. 123, no. 1, pp. 1–9, 2001.

[19] T. M. Keaveny, R. E. Borchers, L. J. Gibson, and W. C. Hayes, ‘Trabecular Bone Modulus and Strength can Depend on Specimen Geometry’, *J Biomech*, vol. 26, no. 8, pp. 991–1000, 1993.

[20] J. H. Keyak, I. Y. Lee, D. S. Nath, and H. B. Skinner, ‘Postfailure compressive behavior of tibial trabecular bone in three anatomic directions’, *J Biomed Mater Res*, vol. 31, no. 3, pp. 373–378, Jul. 1996.

[21] L. S. Chatham, V. V. Patel, C. M. Yakacki, and R. Dana Carpenter, ‘Interbody Spacer Material Properties and Design Conformity for Reducing Subsidence during Lumbar Interbody Fusion’, *J Biomech Eng*, vol. 139, no. 5, pp. 1–8, May 2017.

[22] S. Rastegar, P.-J. Arnoux, X. Wang, C.-É. Aubin, and C.-É. Aubin Biomechanical, ‘Biomechanical analysis of segmental lumbar lordosis and risk of cage subsidence with different cage heights and alternative placements in transforaminal lumbar interbody fusion’, *Comput Methods Biomech Biomed Engin*, vol. 2020, no. 9, pp. 1–20, 2021.

[23] F. Galbusera, H. Schmidt, and H. J. Wilke, ‘Lumbar interbody fusion: A parametric investigation of a novel cage design with and without posterior instrumentation’, *European Spine Journal*, vol. 21, no. 3, pp. 455–462, Mar. 2012.

[24] S. Vadapalli, K. Sairyo, V. K. Goel, M. Robon, A. Biyani, A. Khandha, and N. A. Ebraheim, ‘Biomechanical Rationale for Using Polyetheretherketone (PEEK) Spacers for Lumbar Interbody Fusion-A Finite Element Study’, *Spine (Phila Pa 1976)*, vol. 31, no. 26, pp. 992–998, 2006.

[25] A. Calvo-Echenique, J. Cegoñino, R. Chueca, and A. Pérez-del Palomar, ‘Stand-alone lumbar cage subsidence: A biomechanical sensitivity study of cage design and placement.’, *Comput Methods Programs Biomed*, vol. 162, pp. 211–219, Aug. 2018.

[26] S. A. Kulper, C. X. Fang, X. Ren, M. Guo, K. Y. Sze, F. K. L. Leung, and W. W. Lu, ‘Development and initial validation of a novel smoothed-particle hydrodynamics-based simulation model of trabecular bone penetration by metallic implants’, *Journal of Orthopaedic Research*, vol. 36, no. 4, pp. 1114–1123, Apr. 2018.

[27] N. Soltanihafshejani, T. Bitter, D. Janssen, and N. Verdonschot, ‘Development of a crushable foam model for human trabecular bone’, *Med Eng Phys*, vol. 96, pp. 53–63, Oct. 2021.

[28] T. Issa, ‘Mechanical Testing and Material Modelling of Rigid Polyurethane Foam, a Bone Surrogate’, 2023.

[29] C. Schulze, D. Vogel, M. Sander, and R. Bader, ‘Calibration of crushable foam plasticity models for synthetic bone material for use in finite element analysis of acetabular cup deformation and primary stability’, *Comput Methods Biomech Biomed Engin*, vol. 22, no. 1, pp. 25–37, Jan. 2019.

[30] M. J. Silva, C. Wang, T. M. Keaveny, and W. C. Hayes, ‘Direct and Computed Tomography Thickness Measurements of the Human, Lumbar Vertebral Shell and Endplate’, *Bone*, vol. 15, no. 4, pp. 409–414, 1994.

[31] H. Ritzel, M. Amling, M. Pösl, M. Hahn, and G. Delling, ‘The thickness of human vertebral cortical bone and its changes in aging and osteoporosis: A histomorphometric analysis of the complete spinal column from thirty-seven autopsy specimens’, *Journal of Bone and Mineral Research*, vol. 12, no. 1, pp. 89–95, 1997.

[32] A. Vesterby, L. Mosekilde, H. J. G. Gundersen, F. Melsen, L. Mosekilde, K. Holme’, S. Sorensen’, and A. Vesterby, ‘Biologically Meaningful Determinants of the in Vitro Strength of Lumbar Vertebrae’, *Bone*, vol. 12, pp. 219–224, 1991.

[33] S. Eswaran, A. Gupta, M. Adams, and T. Keaveny, ‘Cortical and Trabecular Load Sharing in the Human Vertebral Body’, *Journal of Bone and Mineral Research*, vol. 21, no. 2, pp. 307–314, Feb. 2006.

[34] Y. Bala, R. Zebaze, A. Ghasem-Zadeh, E. J. Atkinson, S. Iuliano, J. M. Peterson, S. Amin, Å. Bjørnerem, L. J. Melton, H. Johansson, J. A. Kanis, S. Khosla, and E. Seeman, 'Cortical porosity identifies women with osteopenia at increased risk for forearm fractures', *Journal of Bone and Mineral Research*, vol. 29, no. 6, pp. 1356–1362, 2014.

[35] M. L. Bouxsein, S. K. Boyd, B. A. Christiansen, R. E. Guldberg, K. J. Jepsen, and R. Müller, 'Guidelines for assessment of bone microstructure in rodents using micro-computed tomography', *Journal of Bone and Mineral Research*, vol. 25, no. 7, pp. 1468–1486, Jul. 2010.

[36] A. S. Issever, T. M. Link, M. Kentenich, P. Rogalla, K. Schwieger, M. B. Huber, A. J. Burghardt, S. Majumdar, and G. Diederichs, 'Trabecular bone structure analysis in the osteoporotic spine using a clinical in vivo setup for 64-slice MDCT imaging: Comparison to μCT imaging and μFE modeling', *Journal of Bone and Mineral Research*, vol. 24, no. 9, pp. 1628–1637, 2009.

[37] S. C. Cowin and D. H. Hegedus, 'Bone remodeling I: theory of adaptive elasticity', *J Elast*, vol. 6, no. 3, 1976.

[38] L. Mosekilde, 'Age-related changes in bone mass, structure, and strength ± effects of loading', *Z Rheumatol*, vol. 59, 2000.

[39] R. Oftadeh, M. Perez-Viloria, J. C. Villa-Camacho, A. Vaziri, and A. Nazarian, 'Biomechanics and Mechanobiology of Trabecular Bone: A Review', *J Biomech Eng*, vol. 137, no. 1, pp. 1–15, Jan. 2015.

[40] A. Marny Mohamed, 'An Overview of Bone Cells and Their Regulating Factors of Differentiation', *Malaysian Journal of Medical Sciences*, vol. 15, no. 1, pp. 4–12, 2007.

[41] J. Ochoa, A. Sanders, D. Heck, and B. Hillberry, 'Stiffening of the Femoral Head Due to Intertrabecular Fluid and Intraosseous Pressure', *J Biomech Eng*, vol. 113, pp. 259–262, 1991.

[42] D. K. W. Yeung, J. F. Griffith, G. E. Antonio, F. K. H. Lee, J. Woo, and P. C. Leung, 'Osteoporosis is associated with increased marrow fat content and decreased marrow

fat unsaturation: A proton MR spectroscopy study', *Journal of Magnetic Resonance Imaging*, vol. 22, no. 2, pp. 279–285, Aug. 2005.

[43] M. J. Ciarelli, S. A. Goldstein, J. L. Kuhn, D. D. Cody, and M. B. Brown, 'Evaluation of orthogonal mechanical properties and density of human trabecular bone from the major metaphyseal regions with materials testing and computed tomography', *Journal of Orthopaedic Research*, vol. 9, no. 5, pp. 674–682, 1991.

[44] X. Shi, X. Wang, and G. L. Niebur, 'Effects of loading orientation on the morphology of the predicted yielded regions in trabecular bone', *Ann Biomed Eng*, vol. 37, no. 2, pp. 354–362, Feb. 2009.

[45] C. Öhman, M. Baleani, E. Perilli, E. Dall'Ara, S. Tassani, F. Baruffaldi, and M. Viceconti, 'Mechanical testing of cancellous bone from the femoral head: Experimental errors due to off-axis measurements', *J Biomech*, vol. 40, no. 11, pp. 2426–2433, 2007.

[46] E. F. Morgan, H. H. Bayraktar, and T. M. Keaveny, 'Trabecular bone modulus-density relationships depend on anatomic site', *J Biomech*, vol. 36, no. 7, pp. 897–904, Jul. 2003.

[47] B. Sanborn, C. A. Gunnarsson, M. Foster, and T. Weerasooriya, 'Quantitative Visualization of Human Cortical Bone Mechanical Response: Studies on the Anisotropic Compressive Response and Fracture Behavior as a Function of Loading Rate', *Exp Mech*, vol. 56, no. 1, pp. 81–95, Jan. 2016.

[48] S. Li, A. Abdel-Wahab, and V. V. Silberschmidt, 'Analysis of fracture processes in cortical bone tissue', *Eng Fract Mech*, vol. 110, pp. 448–458, Sep. 2013.

[49] A. A. Abdel-Wahab Vadim V Silberschmidt, 'Numerical Modelling of Impact Fracture of Cortical Bone Tissue Using X-FEM', *Journal of Theoretical and Applied Mechanics*, vol. 49, pp. 599–619, 2011.

[50] P. A. Hulme, S. K. Boyd, and S. J. Ferguson, 'Regional variation in vertebral bone morphology and its contribution to vertebral fracture strength', *Bone*, vol. 41, no. 6, pp. 946–957, Dec. 2007.

[51] S. A. Goldstein, D. L. Wilson, D. A. Sonstegard, and L. S. Matthews, ‘The Mechanical Properties of Human Tibial Trabecular Bone as a Function of Metaphyseal Location’, *J Biomech*, vol. 16, pp. 965–969, 1983.

[52] S. Cowin, *Bone Mechanics Handbook*, 2nd ed. 2001.

[53] T. M. Keaveny, P. F. Hoffmann, M. Singh, L. Palermo, J. P. Bilezikian, S. L. Greenspan, and D. M. Black, ‘Femoral bone strength and its relation to cortical and trabecular changes after treatment with PTH, alendronate, and their combination as assessed by finite element analysis of quantitative CT scans’, *Journal of Bone and Mineral Research*, vol. 23, no. 12, pp. 1974–1982, Dec. 2008.

[54] A. Sanyal, A. Gupta, H. H. Bayraktar, R. Y. Kwon, and T. M. Keaveny, ‘Shear strength behavior of human trabecular bone’, *J Biomech*, vol. 45, no. 15, pp. 2513–2519, Oct. 2012.

[55] L. J. Gibson, ‘Biomechanics of cellular solids’, *J Biomech*, vol. 38, no. 3, pp. 377–399, 2005.

[56] T. M. Keaveny, E. F. Morgan, G. L. Niebur, and O. C. Yeh, ‘Biomechanics of Trabecular Bone’, *Annu Rev Biomed Eng*, vol. 3, pp. 307–333, 2001.

[57] M. Amling, M. Posl, H. Ritzel, M. Hahn, M. Vogel, V. J. Wening, G. Delling, and M. Vogel, ‘Architecture and distribution of cancellous bone yield vertebral fracture clues A histomorphometric analysis of the complete spinal column from 40 autopsy specimens’, *Arch Orthop Trauma Surg*, vol. 115, pp. 262–269, 1996.

[58] E. F. Wachtel and T. M. Keaveny, ‘Dependence of trabecular damage on mechanical strain’, *Journal of Orthopaedic Research*, vol. 15, no. 5, pp. 781–787, 1997.

[59] A. Nazarian, D. Meier, R. Müller, and B. D. Snyder, ‘Functional dependence of cancellous bone shear properties on trabecular microstructure evaluated using time-lapsed micro-computed tomographic imaging and torsion testing’, *Journal of Orthopaedic Research*, vol. 27, no. 12, pp. 1667–1674, Dec. 2009.

[60] J. Schwiedrzik, A. Taylor, D. Casari, U. Wolfram, P. Zysset, and J. Michler, ‘Nanoscale deformation mechanisms and yield properties of hydrated bone extracellular matrix’, *Acta Biomater*, vol. 60, pp. 302–314, Sep. 2017.

[61] R. Belda, M. Palomar, J. L. Peris-Serra, A. Vercher-Martínez, and E. Giner, ‘Compression failure characterization of cancellous bone combining experimental testing, digital image correlation and finite element modeling’, *Int J Mech Sci*, vol. 165, pp. 1–12, Jan. 2020.

[62] J. A. Szivek, M. Thomas, and J. B. Benjamin, ‘Characterization of a synthetic foam as a model for human cancellous bone.’, *Journal of Applied Biomaterials*, vol. 4, no. 3, pp. 269–272, 1993.

[63] N. Kelly and J. P. McGarry, ‘Experimental and numerical characterisation of the elasto-plastic properties of bovine trabecular bone and a trabecular bone analogue’, *J Mech Behav Biomed Mater*, vol. 9, pp. 184–197, May 2012.

[64] J. Halgrin, F. Chaari, and É. Markiewicz, ‘On the effect of marrow in the mechanical behavior and crush response of trabecular bone’, *J Mech Behav Biomed Mater*, vol. 5, no. 1, pp. 231–237, Jan. 2012.

[65] W. C. Hayes and D. R. Carter, ‘Postyield behavior of subchondral trabecular bone’, *J Biomed Mater Res*, vol. 10, no. 4, pp. 537–544, 1976.

[66] L. J. Gibson, ‘The Mechanical Behaviour of Cancellous Bone’, *J Biomech*, vol. 18, no. 5, pp. 317–328, 1985.

[67] L. E. Jansen, N. P. Birch, J. D. Schiffman, A. J. Crosby, and S. R. Peyton, ‘Mechanics of intact bone marrow’, *J Mech Behav Biomed Mater*, vol. 50, pp. 299–307, Oct. 2015.

[68] J. S. Blebea, M. Houseni, D. A. Torigian, C. Fan, A. Mavi, Y. Zhuge, T. Iwanaga, S. Mishra, J. Udupa, J. Zhuang, R. Gopal, and A. Alavi, ‘Structural and Functional Imaging of Normal Bone Marrow and Evaluation of Its Age-Related Changes’, *Semin Nucl Med*, vol. 37, no. 3, pp. 185–194, May 2007.

[69] P. Meunier, J. Aaron, C. Edouard, and G. Vignon, ‘Osteoporosis and the Rplacement of Cell Populations of the Marrow by Adipose Tissue’, *Clin Orthop Relat Res*, no. 80, pp. 147–154, 1971.

[70] C. M. Schnitzler and J. Mesquita, ‘Bone marrow composition and bone microarchitecture and turnover in blacks and whites’, *Journal of Bone and Mineral Research*, vol. 13, no. 8, pp. 1300–1307, Aug. 1998.

[71] H. Isaksson, C. C. van Donkelaar, R. Huiskes, and K. Ito, ‘A mechano-regulatory bone-healing model incorporating cell-phenotype specific activity’, *J Theor Biol*, vol. 252, no. 2, pp. 230–246, May 2008.

[72] D. Lacroix, I. P. J. Prendergast, I. G. Li, and D. Marsh, ‘Biomechanical model to simulate tissue differentiation and bone regeneration: application to fracture healing’, *Med Biol Eng Comput*, vol. 40, pp. 14–21, 2002.

[73] A. Hosokawa and T. Otani, ‘Ultrasonic wave propagation in bovine cancellous bone’, *J Acoust Soc Am*, vol. 101, no. 1, pp. 558–562, Jan. 1997.

[74] M. Kasra and M. D. Grynpas, ‘On shear properties of trabecular bone under torsional loading: Effects of bone marrow and strain rate’, *J Biomech*, vol. 40, no. 13, pp. 2898–2903, 2007.

[75] F. Wang, F. Metzner, G. Osterhoff, L. Zheng, and S. Schleifenbaum, ‘The role of bone marrow on the mechanical properties of trabecular bone: a systematic review’, *Biomed Eng Online*, vol. 21, no. 1, Dec. 2022.

[76] H. Ma, R. Ren, Y. Chen, and J. Griffith, ‘A simulation study of marrow fat effect on bone biomechanics’, in *36th Annual International Conference of the IEEE Engineering in Medicine and Biology Society*, 2014.

[77] C. J. Rosen and M. L. Bouxsein, ‘Mechanisms of disease: Is osteoporosis the obesity of bone?’, *Nat Clin Pract Rheumatol*, vol. 2, no. 1, pp. 35–43, Jan. 2006.

[78] A. E. Bravo, L. C. Osnaya, E. I. Ramírez, V. H. Jacobo, and A. Ortiz, ‘The effect of bone marrow on the mechanical behavior of porcine trabecular bone’, *Biomed Phys Eng Express*, vol. 5, no. 6, Nov. 2019.

[79] G. Niebur and T. Keaveny, ‘Computational Modeling in Biomechanics Computational Modeling’, 2009, pp. 277–306.

[80] R. Nareliya and V. Kumar, ‘Finite Element Application to Femur Bone’, *Journal of Biomedical and Bioengineering*, vol. 3, no. 1, pp. 57–62, 2012.

[81] N. Kelly, N. M. Harrison, P. McDonnell, and J. P. McGarry, ‘An experimental and computational investigation of the post-yield behaviour of trabecular bone during

vertebral device subsidence', *Biomech Model Mechanobiol*, vol. 12, no. 4, pp. 685–703, Aug. 2013.

[82] M. Kurutz, 'Finite Element Modelling of Human Lumbar Spine', 2010.

[83] N. M. Harrison, P. F. McDonnell, D. C. O'Mahoney, O. D. Kennedy, F. J. O'Brien, and P. E. McHugh, 'Heterogeneous linear elastic trabecular bone modelling using micro-CT attenuation data and experimentally measured heterogeneous tissue properties', *J Biomech*, vol. 41, no. 11, pp. 2589–2596, Aug. 2008.

[84] S. Nagaraja, T. L. Couse, and R. E. Guldberg, 'Trabecular bone microdamage and microstructural stresses under uniaxial compression', *J Biomech*, vol. 38, no. 4, pp. 707–716, Apr. 2005.

[85] R. Muller and P. Ruegsegger, 'Three-dimensional finite element modelling of non-invasively assessed trabecular bone structures', *Med Eng Phys*, vol. 17, no. 2, pp. 126–133, 1995.

[86] B. Van Rietbergen, H. Weinans, R. Huiskes, and A. Odgaardt, 'A New Method to Determine Trabecular Bone Elastic Properties and Loading Using Micromechanical Finite-Element Models', *J Biomech*, vol. 28, no. 1, pp. 69–81, 1995.

[87] G. Bevill, S. K. Eswaran, A. Gupta, P. Papadopoulos, and T. M. Keaveny, 'Influence of bone volume fraction and architecture on computed large-deformation failure mechanisms in human trabecular bone', *Bone*, vol. 39, no. 6, pp. 1218–1225, Dec. 2006.

[88] J. S. Stölken and J. H. Kinney, 'On the importance of geometric nonlinearity in finite-element simulations of trabecular bone failure', *Bone*, vol. 33, no. 4, pp. 494–504, Oct. 2003.

[89] C. S. Lee, J. M. Lee, B. H. Youn, H. S. Kim, J. K. Shin, T. S. Goh, and J. S. Lee, 'A new constitutive model for simulation of softening, plateau, and densification phenomena for trabecular bone under compression', *J Mech Behav Biomed Mater*, vol. 65, pp. 213–223, Jan. 2017.

[90] J. H. Keyak, 'Improved prediction of proximal femoral fracture load using nonlinear finite element models', *Med Eng Phys*, vol. 23, pp. 165–173, 2001.

[91] C. Mercer, M. Y. He, R. Wang, and A. G. Evans, ‘Mechanisms governing the inelastic deformation of cortical bone and application to trabecular bone’, *Acta Biomater*, vol. 2, no. 1, pp. 59–68, 2006.

[92] L. P. Mullins, M. S. Bruzzi, and P. E. McHugh, ‘Calibration of a constitutive model for the post-yield behaviour of cortical bone’, *J Mech Behav Biomed Mater*, vol. 2, no. 5, pp. 460–470, Oct. 2009.

[93] K. Tai, F. J. Ulm, and C. Ortiz, ‘Nanogranular origins of the strength of bone’, *Nano Lett*, vol. 6, no. 11, pp. 2520–2525, Nov. 2006.

[94] X. Wang, M. R. Allen, D. B. Burr, E. J. Lavernia, B. Jeremić, and D. P. Fyhrie, ‘Identification of material parameters based on Mohr-Coulomb failure criterion for bisphosphonate treated canine vertebral cancellous bone’, *Bone*, vol. 43, no. 4, pp. 775–780, Oct. 2008.

[95] V. S. Deshpande and N. A. Fleck, ‘Isotropic constitutive models for metallic foams’, *J Mech Phys Solids*, vol. 48, pp. 1253–1283, 2000.

[96] M. Kinzl, U. Wolfram, and D. H. Pahr, ‘Identification of a crushable foam material model and application to strength and damage prediction of human femur and vertebral body’, *J Mech Behav Biomed Mater*, vol. 26, pp. 136–147, Oct. 2013.

[97] N. Soltanihafshejani, F. Peroni, S. Toniutti, T. Bitter, E. Tanck, F. Eggermont, N. Verdonschot, and D. Janssen, ‘The application of an isotropic crushable foam model to predict the femoral fracture risk’, *PLoS One*, vol. 18, pp. 1–16, Jul. 2023.

[98] V. Kosmopoulos, C. Schizas, and T. S. Keller, ‘Modeling the onset and propagation of trabecular bone microdamage during low-cycle fatigue’, *J Biomech*, vol. 41, no. 3, pp. 515–522, 2008.

[99] G. L. Niebur, M. J. Feldstein, J. C. Yuen, T. J. Chen, and T. M. Keaveny, ‘High-resolution "nite element models with tissue strength asymmetry accurately predict failure of trabecular bone’, *J Biomech*, vol. 33, pp. 1575–1583, 2000.

[100] G. L. Niebur, M. J. Feldstein, and T. M. Keaveny, ‘Biaxial failure behavior of bovine tibial trabecular bone’, *J Biomech Eng*, vol. 124, no. 6, pp. 699–705, Dec. 2002.

[101] N. Harrison, D. O'Mahoney, P. McDonell, and P. McHugh, 'Damage and failure of trabecular bone with non-linear geometry and inhomogeneous material properties', *J Biomech*, vol. 39, p. 417, 2006.

[102] N. M. Harrison, P. McDonnell, L. Mullins, N. Wilson, D. O'Mahoney, and P. E. McHugh, 'Failure modelling of trabecular bone using a non-linear combined damage and fracture voxel finite element approach', *Biomech Model Mechanobiol*, vol. 12, no. 2, pp. 225–241, Apr. 2013.

[103] H. Giambini, X. Qin, D. Dragomir-Daescu, K. N. An, and A. Nassr, 'Specimen-specific vertebral fracture modeling: a feasibility study using the extended finite element method', *Med Biol Eng Comput*, vol. 54, no. 4, pp. 583–593, Apr. 2016.

[104] M. Charlebois, M. Jirásek, and P. K. Zysset, 'A nonlocal constitutive model for trabecular bone softening in compression', *Biomech Model Mechanobiol*, vol. 9, no. 5, pp. 597–611, Oct. 2010.

[105] V. Tomar, 'Insights into the effects of tensile and compressive loadings on microstructure dependent fracture of trabecular bone', *Eng Fract Mech*, vol. 76, no. 7, pp. 884–897, May 2009.

[106] A. Ural and D. Vashishth, 'Cohesive finite element modeling of age-related toughness loss in human cortical bone', *J Biomech*, vol. 39, no. 16, pp. 2974–2982, 2006.

[107] A. Ural, P. Zioupos, D. Buchanan, and D. Vashishth, 'The effect of strain rate on fracture toughness of human cortical bone: A finite element study', *J Mech Behav Biomed Mater*, vol. 4, no. 7, pp. 1021–1032, Oct. 2011.

[108] R. Fan, H. Gong, X. Zhang, J. Liu, Z. Jia, and D. Zhu, 'Modeling the Mechanical Consequences of Age-Related Trabecular Bone Loss by XFEM Simulation', *Comput Math Methods Med*, vol. 2016, pp. 1–13, 2016.

[109] M. Salem, L. Westover, S. Adeeb, and K. Duke, 'Prediction of failure in cancellous bone using extended finite element method', *Journal of Engineering in Medicine*, vol. 234, no. 9, pp. 988–999, Sep. 2020.

[110] E. M. Feerick, X. C. Liu, and P. McGarry, ‘Anisotropic mode-dependent damage of cortical bone using the extended finite element method (XFEM)’, *J Mech Behav Biomed Mater*, vol. 20, pp. 77–89, Apr. 2013.

[111] A. A. Ali, L. Cristofolini, E. Schileo, H. Hu, F. Taddei, R. H. Kim, P. J. Rullkoetter, and P. J. Laz, ‘Specimen-specific modeling of hip fracture pattern and repair’, *J Biomech*, vol. 47, no. 2, pp. 536–543, Jan. 2014.

[112] J. A. DeWit and D. S. Cronin, ‘Cervical spine segment finite element model for traumatic injury prediction’, *J Mech Behav Biomed Mater*, vol. 10, pp. 138–150, Jun. 2012.

[113] M. Ovesy, M. Indermaur, and P. K. Zysset, ‘Prediction of insertion torque and stiffness of a dental implant in bovine trabecular bone using explicit micro-finite element analysis’, *J Mech Behav Biomed Mater*, vol. 98, pp. 301–310, Oct. 2019.

[114] M. Ovesy, M. Aeschlimann, and P. K. Zysset, ‘Explicit finite element analysis can predict the mechanical response of conical implant press-fit in homogenized trabecular bone’, *J Biomech*, vol. 107, pp. 1–8, Jun. 2020.

[115] R. Hambli, ‘Micro-CT finite element model and experimental validation of trabecular bone damage and fracture’, *Bone*, vol. 56, no. 2, pp. 363–374, Oct. 2013.

[116] F. Khor, D. S. Cronin, B. Watson, D. Gierczycka, and S. Malcolm, ‘Importance of asymmetry and anisotropy in predicting cortical bone response and fracture using human body model femur in three-point bending and axial rotation’, *J Mech Behav Biomed Mater*, vol. 87, pp. 213–229, Nov. 2018.

[117] J. He, J. Yan, S. Margulies, B. Coats, and A. D. Spear, ‘An adaptive-remeshing framework to predict impact-induced skull fracture in infants’, *Biomech Model Mechanobiol*, vol. 19, no. 5, pp. 1595–1605, Oct. 2020.

[118] A. Fischer and Y. Holdstein, ‘A Neural Network Technique for Remeshing of Bone Microstructure’, *Methods in Molecular Biology*, vol. 868, pp. 135–141, 2012.

[119] A. Andrade-Campos, A. Ramos, and J. A. Simões, ‘A model of bone adaptation as a topology optimization process with contact’, *J Biomed Sci Eng*, vol. 05, no. 05, pp. 229–244, 2012.

[120] J. J. Monaghan, ‘Smoothed Particle Hydrodynamics’, *Annu Rev Astron Astrophys*, vol. 30, pp. 543–574, 1992.

[121] SIMULIA Abaqus, ‘Abaqus Analysis User Guide: 15.2.1 Smoothed particle hydrodynamics’, 2016. .

[122] X. Xu and X. L. Deng, ‘An improved weakly compressible SPH method for simulating free surface flows of viscous and viscoelastic fluids’, *Comput Phys Commun*, vol. 201, pp. 43–62, Apr. 2016.

[123] X. Guo, B. D. Rogers, S. Lind, and P. K. Stansby, ‘New massively parallel scheme for Incompressible Smoothed Particle Hydrodynamics (ISPH) for highly nonlinear and distorted flow’, *Comput Phys Commun*, vol. 233, pp. 16–28, Dec. 2018.

[124] A. Krimi, M. Rezoug, S. Khelladi, X. Nogueira, M. Deligant, and L. Ramírez, ‘Smoothed Particle Hydrodynamics: A consistent model for interfacial multiphase fluid flow simulations’, *J Comput Phys*, vol. 358, pp. 53–87, Apr. 2018.

[125] D. Hu, T. Long, Y. Xiao, X. Han, and Y. Gu, ‘Fluid-structure interaction analysis by coupled FE-SPH model based on a novel searching algorithm’, *Comput Methods Appl Mech Eng*, vol. 276, pp. 266–286, Jul. 2014.

[126] T. Verbrugghe, J. M. Domínguez, A. J. C. Crespo, C. Altomare, V. Stratigaki, P. Troch, and A. Kortenhaus, ‘Coupling methodology for smoothed particle hydrodynamics modelling of non-linear wave-structure interactions’, *Coastal Engineering*, vol. 138, pp. 184–198, Aug. 2018.

[127] N. Zhang, X. Zheng, Q. Ma, W. Duan, A. Khayyer, X. Lv, and S. Shao, ‘A hybrid stabilization technique for simulating water wave – Structure interaction by incompressible Smoothed Particle Hydrodynamics (ISPH) method’, *Journal of Hydro-Environment Research*, vol. 18, pp. 77–94, Feb. 2018.

[128] Y. Xiao and H. Dong, ‘Studying normal and oblique perforation of steel plates with SPH simulations’, *Int J Appl Mech*, vol. 9, no. 6, pp. 1–23, Sep. 2017.

[129] Y. Xiao, H. Dong, J. Zhou, and J. Wang, ‘Studying normal perforation of monolithic and layered steel targets by conical projectiles with SPH simulation and analytical method’, *Eng Anal Bound Elem*, vol. 75, pp. 12–20, Feb. 2017.

[130] Z. L. Zhang and M. B. Liu, ‘Smoothed particle hydrodynamics with kernel gradient correction for modeling high velocity impact in two- and three-dimensional spaces’, *Eng Anal Bound Elem*, vol. 83, pp. 141–157, Oct. 2017.

[131] Z. L. Zhang, D. L. Feng, T. Ma, and M. B. Liu, ‘Predicting the damage on a target plate produced by hypervelocity impact using a decoupled finite particle method’, *Eng Anal Bound Elem*, vol. 98, pp. 110–125, Jan. 2019.

[132] E. Basafa, R. J. Murphy, M. D. Kutzer, Y. Otake, and M. Armand, ‘A Particle Model for Prediction of Cement Infiltration of Cancellous Bone in Osteoporotic Bone Augmentation’, *PLoS One*, vol. 8, no. 6, pp. 1–10, Jun. 2013.

[133] C. Cao, J. Zhao, L. Chao, G. Li, and D. Huang, ‘Micro-mechanism study on tissue removal behavior under medical waterjet impact using coupled SPH-FEM’, *Med Biol Eng Comput*, vol. 61, pp. 721–737, Mar. 2023.

[134] S. Li, A. Zahedi, and V. Silberschmidt, ‘Numerical simulation of bone cutting: Hybrid SPH-FE approach’, in *Numerical Methods and Advanced Simulation in Biomechanics and Biological Processes*, Elsevier Inc., 2018, pp. 187–201.

[135] A. Khayyer, Y. Shimizu, C. H. Lee, A. Gil, H. Gotoh, and J. Bonet, ‘An improved updated Lagrangian SPH method for structural modelling’, *Comput Part Mech*, pp. 1–32, 2023.

[136] J. Bonet and S. Kulasegaram, ‘Remarks on tension instability of Eulerian and Lagrangian corrected smooth particle hydrodynamics (CSPH) methods’, *Int J Numer Methods Eng*, vol. 52, no. 11, pp. 1203–1220, Dec. 2001.

[137] B. Bagheri, A. Abdollahzadeh, M. Abbasi, & Amir, and H. Kokabi, ‘Numerical analysis of vibration effect on friction stir welding by smoothed particle hydrodynamics (SPH)’, *International Journal of Advanced Manufacturing Technology*, vol. 110, pp. 209–228, 2020.

[138] J. P. Grant, T. R. Oxland, and M. F. Dvorak, ‘Mapping the Structural Properties of the Lumbosacral Vertebral Endplates’, *Spine (Phila Pa 1976)*, vol. 26, no. 8, pp. 889–896, 2001.

[139] T. M. Jackman, A. M. DelMonaco, and E. F. Morgan, ‘Accuracy of finite element analyses of CT scans in predictions of vertebral failure patterns under axial compression and anterior flexion’, *J Biomech*, vol. 49, no. 2, pp. 267–275, Jan. 2016.

[140] T.-H. Lim, H. Kwon, C.-H. Jeon, J. G. Kim, M. Sokolowski, R. Natarajan, H. S. An, and G. B. J. Andersson, ‘Effect of Endplate Conditions and Bone Mineral Density on the Compressive Strength of the Graft-Endplate Interface in Anterior Cervical Spine Fusion’, *Spine (Phila Pa 1976)*, vol. 26, no. 8, pp. 951–956, 2001.

[141] S. J. Fatihhi, M. N. Harun, M. R. Abdul Kadir, J. Abdullah, T. Kamarul, A. Öchsner, and A. Syahrom, ‘Uniaxial and Multiaxial Fatigue Life Prediction of the Trabecular Bone Based on Physiological Loading: A Comparative Study’, *Ann Biomed Eng*, vol. 43, no. 10, pp. 2487–2502, Oct. 2015.

[142] B. Jost, P. A. Cripton, T. Lund, T. R. Oxland, K. Lippuner, P. Jaeger, L.-P. Nolte, · T R Oxland, and M. E. Müller, ‘Compressive strength of interbody cages in the lumbar spine: the effect of cage shape, posterior instrumentation and bone density’, *European Spine Journal*, vol. 7, pp. 132–141, 1998.

[143] R. Closkey, R. Parsons, C. Lee, M. Blacksin, and M. Zimmerman, ‘Mechanics of Interbody Spinal Fusion’, *Spine (Phila Pa 1976)*, vol. 18, no. 8, pp. 1011–1015, 1993.

[144] H. Chen, S. Shoumura, S. Emura, and Y. Bunai, ‘Regional variations of vertebral trabecular bone microstructure with age and gender’, *Osteoporosis International*, vol. 19, no. 10, pp. 1473–1483, Oct. 2008.

[145] D. G. Kim, C. A. Hunt, R. Zauel, D. P. Fyhrie, and Y. N. Yeni, ‘The effect of regional variations of the trabecular bone properties on the compressive strength of human vertebral bodies’, *Ann Biomed Eng*, vol. 35, no. 11, pp. 1907–1913, Nov. 2007.

[146] S. Roberts, I. W. Mccall, J. Menage, M. J. Haddaway, S. M. Eisenstein, R. Jones, A. H. Orthopaedic, and • M J Haddaway, ‘Does the thickness of the vertebral subchondral bone reflect the composition of the intervertebral disc?’, *European Spine Journal*, vol. 6, pp. 385–389, 1997.

[147] T. G. Lowe, S. Hashim, L. A. Wilson, M. F. O, D. A. Smith, M. J. Diekmann, and J. Trommeter, ‘A Biomechanical Study of Regional Endplate Strength and Cage

Morphology as It Relates to Structural Interbody Support', *Spine (Phila Pa 1976)*, vol. 29, no. 21, pp. 2389–2394, 2004.

[148] 'F2077-22 Standard Test Methods for Intervertebral Body Fusion Devices'.

[149] 'F2267-22 Standard Test Method for Measuring Load-Induced Subsidence of Intervertebral Body Fusion Device Under Static Axial Compression'.

[150] A. K. Aiyangar, A. G. Au, P. A. Anderson, and H.-L. Ploeg, 'Comparison of Two Bone Surrogates for Interbody Device Subsidence Testing', *J ASTM Int*, vol. 9, no. 1, pp. 1–7, 2011.

[151] P. B. Suh, C. Puttlitz, C. Lewis, B. S. Bal, and K. McGilvray, 'The effect of cervical interbody cage morphology, material composition, and substrate density on cage subsidence', *Journal of the American Academy of Orthopaedic Surgeons*, vol. 25, no. 2, pp. 160–168, 2017.

[152] A. Kettler, H.-J. Wilke, R. Dietl, M. Krammer, C. Lumenta, and L. Claes, 'Stabilizing effect of posterior lumbar interbody fusion cages before and after cyclic loading', *J Neurosurg Spine*, vol. 92, pp. 87–92, 2000.

[153] A. Kettler, W. Schmoelz, E. Kast, M. Gottwald, L. Claes, and H.-J. Wilke, 'In Vitro Stabilizing Effect of a Transforaminal Compared With Two Posterior Lumbar Interbody Fusion Cages', *Spine (Phila Pa 1976)*, vol. 30, pp. 665–670, 2005.

[154] H. J. Wilke, D. Volkheimer, B. Robie, and F. B. Christensen, 'Two-piece ALIF cage optimizes the bone–implant interface in a 360° setting', *European Spine Journal*, vol. 26, no. 11, pp. 2747–2753, Nov. 2017.

[155] L. La Barbera, H. J. Wilke, C. Liebsch, T. Villa, A. Luca, F. Galbusera, and M. Brayda-Bruno, 'Biomechanical in vitro comparison between anterior column realignment and pedicle subtraction osteotomy for severe sagittal imbalance correction', *European Spine Journal*, vol. 29, no. 1, pp. 36–44, Jan. 2020.

[156] V. Shim, J. Boheme, C. Josten, and I. Anderso, 'Use of Polyurethane Foam in Orthopaedic Biomechanical Experimentation and Simulation', in *Polyurethane*, InTech, 2012, pp. 171–199.

[157] J. A. Szivek, J. D. Thompson, and J. B. Benjamin, ‘Characterization of three formulations of a synthetic foam as models for a range of human cancellous bone types’, *Journal of Applied Biomaterials*, vol. 6, no. 2, pp. 125–128, 1995.

[158] K. Haggard, ‘Rigid Polyurethane Foams and Hazardous Materials: Applications in Transport and Blast Energy Absorption’, in *34th Department of Defense Explosives Safety Seminar*, 2010.

[159] R. J. Hartstock, E. B. Smith, and C. S. Petty, ‘Normal Variations with Aging of the Amount of Hematopoietic Tissue in Bone Marrow From the Anterior Iliac Crest’, *J Clin Pathol*, vol. 43, no. 4, pp. 326–331, 1965.

[160] SIMULIA Abaqus, ‘ABAQUS Analysis User’s Manual: 18.3.5 Crushable foam plasticity models’, 2009. .

[161] D. Webster, F. A. Schulte, F. M. Lambers, G. Kuhn, and R. Müller, ‘Strain energy density gradients in bone marrow predict osteoblast and osteoclast activity: A finite element study’, *J Biomech*, vol. 48, no. 5, pp. 866–874, Mar. 2015.

[162] Sawbones, ‘Test Materials and Composite Bones Biomechanical Products Catalog’. .

[163] ‘F1839-08 Standard Specification for Rigid Polyurethane Foam for Use as a Standard Material for Testing Orthopaedic Devices and Instruments’.

[164] M. S. Thompson, I. D. McCarthy, L. Lidgren, and L. Ryd, ‘Compressive and Shear Properties of Commercially Available Polyurethane Foams’, *J Biomech Eng*, vol. 125, no. 5, pp. 732–734, Oct. 2003.

[165] P. S. D. Patel, D. E. T. Shepherd, and D. W. L. Hukins, ‘Compressive properties of commercially available polyurethane foams as mechanical models for osteoporotic human cancellous bone’, *BMC Musculoskelet Disord*, vol. 9, pp. 1–7, 2008.

[166] K. L. Calvert, K. P. Trumble, T. J. Webster, and L. A. Kirkpatrick, ‘Characterization of commercial rigid polyurethane foams used as bone analogs for implant testing’, *J Mater Sci Mater Med*, vol. 21, no. 5, pp. 1453–1461, May 2010.

[167] J. A. Grant, N. E. Bishop, N. Götzen, C. Sprecher, M. Honl, and M. M. Morlock, ‘Artificial composite bone as a model of human trabecular bone: The implant-bone interface’, *J Biomech*, vol. 40, no. 5, pp. 1158–1164, 2007.

[168] N. Chessin and W. Driver, ‘Compression and Friction Properties of Rigid Polyurethane Foams’, *Journal of Cellular Plastics*, pp. 185–191, 1967.

Appendices

Appendix A

Experimental Standard Operating Procedure

Sampling Name ID: SB – Date of Test – Sample # of Test Day – Sample Face (A or B)

- Turn ON the VIVO Joint Simulator to warm up
    - Ensure all controls are set to their neutral position
- Test Fixture Setup Phase
    - For FC Test Setup
        - Mount Top Part of the Fixture (FC Indenter) to Abduction Arm
        - Jog Base Plate up to 20mm in displacement position
        - Mount Bottom Part of the Fixture (Fixture Plates), adjust standoffs for Plates so that the Foam-Implant system nearly touches the FC Indenter
        - Mount Optical Motion Trackers to FC Indenter and Fixture Plates
    - For BSJ Test Setup
        - Apply Cartesian Coordinate system setting *in vivo*
        - Jog Flexion Arm to 110 degrees (Flexion Arm will be vertical)
        - Remove Grease Port Bolt from Flexion Arm
            - Mount Top Part of the Fixture (BSJ Indenter) directly to Flexion Arm
        - Jog Base Plate up to 20mm in displacement position
        - Mount Fixture Plates, adjust standoffs for Plates so that the Foam-Implant system nearly touches the BSJ Indenter
        - Mount Optical Motion Trackers to BSJ Indenter and Fixture Plates
- Insert PU foam – Steel Tube system into test space, fixed by the Fixture Plates
- Center Implant on PU foam using custom-made Implant Alignment Jig
- Center the Indenter overtop of the Foam - Implant sample
- VIVO Settings
    - Auto-Zero the VIVO Load Cell
    - Apply a 10 N compressive pre-load (in VL direction) (using force-control setting)
    - Set the current position as the reference position in the VIVO settings

- Set the VIVO control parameters
    - For FC Test Setup: All axes in force-control, ILC off, Virtual Ligaments Disabled
    - For BSJ Test Setup: VL axis in force-control, all uncontrolled axes in displacement-control, ILC off, Virtual Ligaments Disabled
- Apply linear waveform
    - Set waveform cycle frequency = 0.0065
- Data Acquisition: Acquire all post trigger data by elapsed time, apply a 50Hz data filter, and only record load cell data (no recording of virtual forces)
- Start/Stop Behaviour: Start from current, maintain stop pose, do not load/record ILC profile
- Set VL direction event monitor at +/- 9mm hard stop to prevent the indenter from impacting the steel tubing encasing the PU foam
- Apply pre-calibrated VIVO servo response settings (see servo tuning protocol)

- Optical Motion Tracking Settings
    - Turn ON the Optical Motion Tracking Camera
    - Load Tracker Files corresponding to the three used trackers (Apple1, Apple2, Calibration Digitization Tool)
        - Set the Optical Motion Tracker fixed to the Base Plates (Apple1) as the Global Reference Tracker
- Begin Optical Motion Tracking recording including recording of Apple1 and the Calibration Digitization Tool
    - Digitize the points on the surface PU foam sample and position of the implant for use of coordinate transformation of Optical Motion Tracking results
- Begin Test
    - Begin Optical Motion Tracking recording including recording of Apple1 and Apple2
    - Start VIVO test
- Test END
    - VIVO Test Ends and all axes return to original positions at start of test
    - Stop Optical Motion Tracking recording
    - Jog Base Plate to Separate the Foam – Implant sample from the Indenter
        - Remove the Foam – Implant sample from the test fixtures
- Repeat protocol for next sample

Appendix B

Experimental Photographs of Each Tested Sample

Overhead view of deformed sandwiched PU foam samples. Samples 1A, 2A, 3A, 4A, 5A, 6A using FC setup depicted.

Overhead view of deformed sandwiched PU foam samples. Samples 1B, 2B, 3B, 4B, 5B, 6B using FC setup depicted.

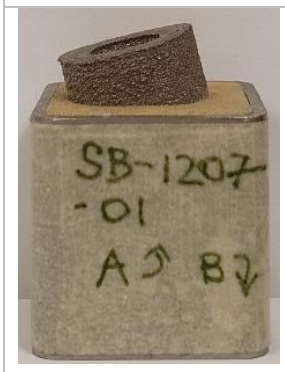		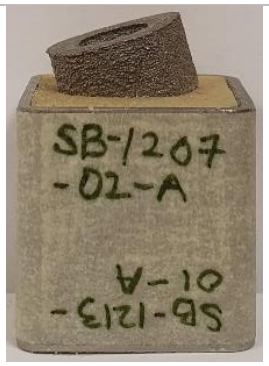	
FC: Sample 1-A	FC: Sample 1-B	FC: Sample 2-A	FC: Sample 2-B

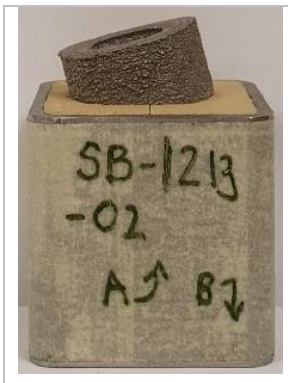

FC: Sample 3-A

FC: Sample 3-B

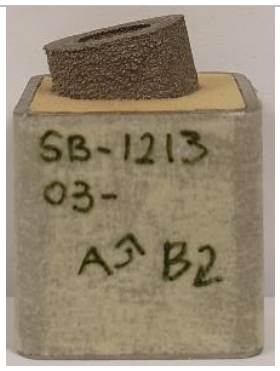

FC: Sample 4-A

FC: Sample 4-B

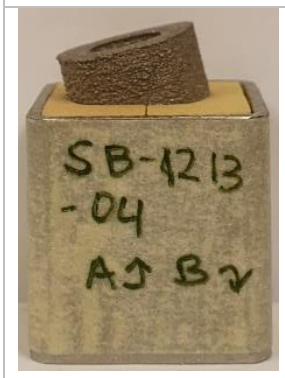

FC: Sample 5-A

FC: Sample 5-B

FC: Sample 6-A

FC: Sample 6-B

Overhead view of deformed sandwiched PU foam samples. Samples 1A, 2A, 3A, 4A, 5A, 6A using BSJ setup depicted.

Overhead view of deformed sandwiched PU foam samples. Samples 1B, 2B, 3B, 4B, 5B, 6B using BSJ setup depicted.

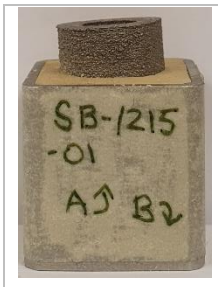			
BSJ: Sample 1-A	BSJ: Sample 1-B	BSJ: Sample 2-A	BSJ: Sample 2-B
			
BSJ: Sample 3-A	BSJ: Sample 3-B	BSJ: Sample 4-A	BSJ: Sample 4-B
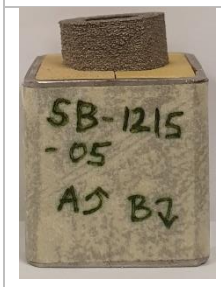			
BSJ: Sample 5-A	BSJ: Sample 5-B	BSJ: Sample 6-A	BSJ: Sample 6-B

Appendix C

Coordinate Frame Transformation MATLAB Script

```
excelFilePath = 'C:\Users\mmeinst\Downloads\test transform\SB-Data-NDI-FINAL_testtransform2.xlsx';

% Manually define the calibration points taken on surface of the Sawbones wrt A1

calibA_A1_120701A = [-127.329; -20.211; -100.46];
calibB_A1_120701A = [-127.69; -20.211; -85.291];
calibD_A1_120701A = [-134.135; -20.211; -84.784];

calibA_A1_120701B = [-126.586; -20.845; -99.005];
calibB_A1_120701B = [-127.67; -20.845; -85.204];
calibD_A1_120701B = [-134.288; -20.845; -85.755];

calibA_A1_120702A = [-126.635; -19.895; -99.233];
calibB_A1_120702A = [-127.273; -19.895; -84.721];
calibD_A1_120702A = [-133.025; -19.895; -86.858];

calibA_A1_121301A = [-123.142; -19.925; -102.443];
calibB_A1_121301A = [-125.797; -19.925; -85.266];
calibD_A1_121301A = [-130.591; -19.925; -87.182];

calibA_A1_121302A = [-123.099; -19.164; -100.567];
calibB_A1_121302A = [-125.024; -19.164; -86.46];
calibD_A1_121302A = [-132.332; -19.164; -87.503];

calibA_A1_121302B = [-125.79; -19.959; -102.462];
calibB_A1_121302B = [-124.304; -19.959; -85.755];
calibD_A1_121302B = [-132.969; -19.959; -85.499];

calibA_A1_121303A = [-126.407; -19.026; -103.06];
calibB_A1_121303A = [-130.905; -19.026; -87.112];
calibD_A1_121303A = [-132.712; -18.841; -86.578];

calibA_A1_121303B = [-125.702; -18.969; -100.447];
calibB_A1_121303B = [-128.041; -18.969; -85.854];
calibD_A1_121303B = [-132.773; -18.969; -86.297];

calibA_A1_121304A = [-127.098; -20.794; -101.38];
calibB_A1_121304A = [-126.309; -20.794; -87.458];
calibD_A1_121304A = [-132.726; -20.794; -87.022];

calibA_A1_121304B = [-126.994; -19.623; -101.494];
```

```
calibB_A1_121304B = [-123.947; -19.623; -85.203];
calibD_A1_121304B = [-132.429; -19.623; -86.694];

calibA_A1_121305A = [-125.983; -19.192; -102.004];
calibB_A1_121305A = [-124.262; -19.192; -84.104];
calibD_A1_121305A = [-132.693; -19.192; -86.732];

calibA_A1_121305B = [-127.905; -20.301; -102.163];
calibB_A1_121305B = [-127.293; -20.301; -87.107];
calibD_A1_121305B = [-133.209; -20.301; -85.988];

calibA_A1_121501B = [-122.856; -18.96; -98.234];
calibB_A1_121501B = [-123.913; -18.96; -86.737];
calibD_A1_121501B = [-133.536; -18.96; -88.884];

calibA_A1_121502A = [-123.268; -19.576; -102.836];
calibB_A1_121502A = [-126.956; -19.576; -85.12];
calibD_A1_121502A = [-131.965; -19.576; -87.237];

calibA_A1_121502B = [-124.451; -21.489; -99.517];
calibB_A1_121502B = [-124.859; -21.489; -85.346];
calibD_A1_121502B = [-132.237; -21.489; -87.588];

calibA_A1_121503A = [-123.555; -20.08; -99.575];
calibB_A1_121503A = [-125.916; -20.08; -87.58];
calibD_A1_121503A = [-131.798; -20.08; -87.146];

calibA_A1_121503B = [-123.427; -19.518; -101.428];
calibB_A1_121503B = [-124.894; -19.518; -85.179];
calibD_A1_121503B = [-132.292; -19.518; -87.685];

calibA_A1_121501A = calibA_A1_121503B;
calibB_A1_121501A = calibB_A1_121503B;
calibD_A1_121501A = calibD_A1_121503B;

calibA_A1_121504A = calibA_A1_121503B;
calibB_A1_121504A = calibB_A1_121503B;
calibD_A1_121504A = calibD_A1_121503B;

calibA_A1_121504B = [-122.284; -19.748; -100.511];
calibB_A1_121504B = [-126.141; -19.748; -86.308];
calibD_A1_121504B = [-132.486; -19.748; -87.19];

calibA_A1_121505A = [-125.653; -19.769; -99.532];
calibB_A1_121505A = [-125.212; -19.769; -86.318];
calibD_A1_121505A = [-135.281; -19.769; -87.922];
```

```
calibA_A1_121505B = [-123.205; -21.945; -100.164];
calibB_A1_121505B = [-125.778; -21.945; -86.999];
calibD_A1_121505B = [-132.708; -21.945; -87.507];

calibA_A1_121506A = [-122.985; -19.755; -98.353];
calibB_A1_121506A = [-127.329; -19.755; -86.847];
calibD_A1_121506A = [-131.828; -19.755; -88.022];

calibA_A1_121506B = [-124.604; -20.377; -96.792];
calibB_A1_121506B = [-125.814; -20.377; -85.049];
calibD_A1_121506B = [-131.102; -20.377; -87.549];

% Create a matrix with 24 columns with each calibration dataset for each
% test to be referenced in a for loop later
calibA_A1 = horzcat(calibA_A1_120701A, calibA_A1_120701B, calibA_A1_120702A,
calibA_A1_121301A, calibA_A1_121302A, calibA_A1_121302B, calibA_A1_121303A,
calibA_A1_121303B, calibA_A1_121304A, calibA_A1_121304B, calibA_A1_121305A,
calibA_A1_121305B,calibA_A1_121501A, calibA_A1_121501B, calibA_A1_121502A,
calibA_A1_121502B, calibA_A1_121503A, calibA_A1_121503B, calibA_A1_121504A,
calibA_A1_121504B, calibA_A1_121505A, calibA_A1_121505B, calibA_A1_121506A,
calibA_A1_121506B);
calibB_A1 = horzcat(calibB_A1_120701A, calibB_A1_120701B, calibB_A1_120702A,
calibB_A1_121301A, calibB_A1_121302A, calibB_A1_121302B, calibB_A1_121303A,
calibB_A1_121303B, calibB_A1_121304A, calibB_A1_121304B, calibB_A1_121305A,
calibB_A1_121305B,calibB_A1_121501A, calibB_A1_121501B, calibB_A1_121502A,
calibB_A1_121502B, calibB_A1_121503A, calibB_A1_121503B, calibB_A1_121504A,
calibB_A1_121504B, calibB_A1_121505A, calibB_A1_121505B, calibB_A1_121506A,
calibB_A1_121506B);
calibD_A1 = horzcat(calibD_A1_120701A, calibD_A1_120701B, calibD_A1_120702A,
calibD_A1_121301A, calibD_A1_121302A, calibD_A1_121302B, calibD_A1_121303A,
calibD_A1_121303B, calibD_A1_121304A, calibD_A1_121304B, calibD_A1_121305A,
calibD_A1_121305B,calibD_A1_121501A, calibD_A1_121501B, calibD_A1_121502A,
calibD_A1_121502B, calibD_A1_121503A, calibD_A1_121503B, calibD_A1_121504A,
calibD_A1_121504B, calibD_A1_121505A, calibD_A1_121505B, calibD_A1_121506A,
calibD_A1_121506B);

%%

% Sheet names in excel sheet for the script to go through, read and edit
Sheets = ['SB-1207-01-A';
'SB-1207-01-B';
'SB-1207-02-A';
'SB-1213-01-A';
'SB-1213-02-A';
'SB-1213-02-B';
```

```
'SB-1213-03-A';
'SB-1213-03-B';
'SB-1213-04-A';
'SB-1213-04-B';
'SB-1213-05-A';
'SB-1213-05-B';
'SB-1215-01-A';
'SB-1215-01-B';
'SB-1215-02-A';
'SB-1215-02-B';
'SB-1215-03-A';
'SB-1215-03-B';
'SB-1215-04-A';
'SB-1215-04-B';
'SB-1215-05-A';
'SB-1215-05-B';
'SB-1215-06-A';
'SB-1215-06-B'];

for j = 1:24
   excelWorksheet = Sheets(j,1:12);
   disp(excelWorksheet)
   % Vector at time = 0 defining position of Apple2 wrt Apple1
   % It's different each test and particularly different between FC & BSJ


   % vec_A2_A1_t0 = xlsread(excelFilePath, excelWorksheet, 'U2:W2').';

   %In the below commented out versions of vec_a2_a1_etc, they are only
   %for the ASTM (BSJ) tests. This is because Apple2 was rotated by 90deg
   %during those tests relative to its position in the VIVO control (FC)
   %tests and so the X and Y translations and rotations are swapped. The
   %thought was to manually swap out the x and y but that caused issues
   %seen with Martine on Jan25'24

   DataNDI_translations_A1_A2 = xlsread(excelFilePath, excelWorksheet, 'U2:W2');
   vec_A2_A1_t0 = [DataNDI_translations_A1_A2(1,1); DataNDI_translations_A1_A2(1,2);
DataNDI_translations_A1_A2(1,3);];

   %%
   % PART 1 solve for T_SB_A1 Apple1 wrt Sawbones surface

   % STEP 1
   % Define AB and AD vectors
   vecAB = calibB_A1(:,j) - calibA_A1(:,j);
   vecAD = calibD_A1(:,j) - calibA_A1(:,j);
```

```
% Determine the unit vectors
vecAB_unit = vecAB/norm(vecAB);
vecAD_unit = vecAD/norm(vecAD);

% STEP 2
% Set y as the unit vector in SI axis, pointed inferiorly
y = cross(vecAD_unit, vecAB_unit);
y_unit = y/norm(y);

% STEP 3
% Let z = vecAB_unit and then compute x from z and y
z_unit = vecAB_unit;
x_unit = cross(y_unit, z_unit);
% Construct the transformation matrix T of SB wrt A1. Origin position set as calibD
T_A1_SB = [x_unit, y_unit, z_unit, calibD_A1(:,j); 0 0 0 1];
% Invert T_A1_SB to get T_SB_A1
T_SB_A1 = inv(T_A1_SB);


%%
% PART 2 solve for T_A2_CG Cage wrt Apple2
% Using same calibration points so it becomes simpler. If using
% calibrations points from a different surface (ie top surf of cage), must
% repeat process in Part 1

% STEP 1
% Determine coordinates of origin point wrt Apple2
calibD_A2 = calibD_A1(:,j) - vec_A2_A1_t0;

% Construct the transformation matrix T of SB wrt A1. Origin position set as calibD
T_A2_CG = [x_unit, y_unit, z_unit, calibD_A2; 0 0 0 1];

%%
% PART 3 Develop the Transformation Matrix of A2 wrt A1

% STEP 1 Compute the rotation matrix of A2 wrt A1

% Read Excel data and create an empty matrix to store results into
DataNDI = xlsread(excelFilePath, excelWorksheet, 'R:W');
results = zeros(size(DataNDI, 1),7);
resultsinv = zeros(size(DataNDI, 1),7); %test

for i = 1:size(DataNDI, 1)

    % Convert frame # to time, based on NDI 60FPS. Used only for results.
    time = (i-1)/60;
```

```
% Define the rotation angles from NDI tracking
rot_vec = [DataNDI(i,3); DataNDI(i,2); DataNDI(i,1)];

% Define the rotation vector as a unit vector and its normal scale factor
rot_vec_norm = norm(rot_vec);
rot_vec_unit = rot_vec/rot_vec_norm;
% Assemble the unit vector and the normal into a 1x4 vector
rot_vec_A1_A2 = [rot_vec_unit(1) rot_vec_unit(2) rot_vec_unit(3) rot_vec_norm];
% Compute rotation vector from axis angles. Angles must be in radians
rot_mat_A1_A2 = axang2rotm(deg2rad(rot_vec_A1_A2));

% STEP 2 Compute the transformation matrix of A2 wrt A1 using the developed
% rotation matrix and the origin point based on translation point from NDI

transl_vec = [DataNDI(i,4); DataNDI(i,5); DataNDI(i,6)];

T_A1_A2 = [rot_mat_A1_A2, transl_vec; 0 0 0 1];

%%
% PART 4 Multiply the three matrices together to form the transformation
% matrix of Cage relative to Sawbones T_SB_CG

T_SB_CG = (T_SB_A1 * T_A1_A2) * T_A2_CG;

% Draw the rotation matrix of SB wrt CG from its Transformation Matrix
rot_mat_SB_CG = T_SB_CG(1:3, 1:3);
% Compute axis angles from the rotation matrix
rot_vec_SB_CG = rotm2axang(rot_mat_SB_CG);

% Determine the axis angles of SB wrt CG
Rx_SB_CG = rad2deg(rot_vec_SB_CG(1,1)*rot_vec_SB_CG(1,4));
Ry_SB_CG = rad2deg(rot_vec_SB_CG(1,2)*rot_vec_SB_CG(1,4));
Rz_SB_CG = rad2deg(rot_vec_SB_CG(1,3)*rot_vec_SB_CG(1,4));

Tx_SB_CG = T_SB_CG(1,4);
Ty_SB_CG = T_SB_CG(2,4);
Tz_SB_CG = T_SB_CG(3,4);

results(i,1:7) = [time,Rx_SB_CG, Ry_SB_CG, Rz_SB_CG, Tx_SB_CG, Ty_SB_CG,
Tz_SB_CG];

%Same thing but now with SB wrt CG instead of CG wrt SB

T_CG_SB = inv(T_SB_CG);
```

```
        % Draw the rotation matrix of CG wrt SB from its Transformation Matrix
        rot_mat_CG_SB = T_CG_SB(1:3, 1:3);
        % Compute axis angles from the rotation matrix
        rot_vec_CG_SB = rotm2axang(rot_mat_CG_SB);

        % Determine the axis angles of SB wrt CG
        Rx_CG_SB = rad2deg(rot_vec_CG_SB(1,1)*rot_vec_CG_SB(1,4));
        Ry_CG_SB = rad2deg(rot_vec_CG_SB(1,2)*rot_vec_CG_SB(1,4));
        Rz_CG_SB = rad2deg(rot_vec_CG_SB(1,3)*rot_vec_CG_SB(1,4));

        Tx_CG_SB = T_CG_SB(1,4);
        Ty_CG_SB = T_CG_SB(2,4);
        Tz_CG_SB = T_CG_SB(3,4);

        resultsinv(i,1:7) = [time,Rx_CG_SB, Ry_CG_SB, Rz_CG_SB, Tx_CG_SB, Ty_CG_SB,
Tz_CG_SB];
    end;


    headers = {'Frame','Rx_CG_SB', 'Ry_CG_SB', 'Rz_CG_SB', 'Tx_CG_SB', 'Ty_CG_SB',
'Tz_CG_SB'};
    xlswrite(excelFilePath, headers, excelWorksheet, 'AH1');
    xlswrite(excelFilePath, results-results(1,:), excelWorksheet, 'AH2');
    headers = {'Frame','Rx_CG_SB_raw', 'Ry_CG_SB_raw', 'Rz_CG_SB_raw',
'Tx_CG_SB_raw', 'Ty_CG_SB_raw', 'Tz_CG_SB_raw'};
    xlswrite(excelFilePath, headers, excelWorksheet, 'AP1');
    xlswrite(excelFilePath, results, excelWorksheet, 'AP2');


    headers = {'Frame','Rx_SB_CG', 'Ry_SB_CG', 'Rz_SB_CG', 'Tx_SB_CG', 'Ty_SB_CG',
'Tz_SB_CG'};
    xlswrite(excelFilePath, headers, excelWorksheet, 'AX1');
    xlswrite(excelFilePath, resultsinv-resultsinv(1,:), excelWorksheet, 'AX2');
    headers = {'Frame','Rx_SB_CG_raw', 'Ry_SB_CG_raw', 'Rz_SB_CG_raw',
'Tx_SB_CG_raw', 'Ty_SB_CG_raw', 'Tz_SB_CG_raw'};
    xlswrite(excelFilePath, headers, excelWorksheet, 'BF1');
    xlswrite(excelFilePath, resultsinv, excelWorksheet, 'BF2');

end;
```